

EXPERIMENTAL AND ANALYTICAL
INVESTIGATION OF MULTIPLE JETS IN A CROSS-FLOW,

by

Kakkattukuzhy Mathai, Isaac

Dissertation submitted to the Faculty of the
Virginia Polytechnic Institute and State University
in partial fulfillment of the requirements for the degree of

DOCTOR OF PHILOSOPHY

in

Aerospace Engineering

APPROVED:

A. K. Jakubowski, Chairman

J. A. Schetz

J. F. Marchman, Jr.

W. E. Kohler

C. H. Long

August, 1982
Blacksburg, Virginia

ACKNOWLEDGEMENTS

The author wishes to thank Dr. A.K. Jakubowski who, as the Chairman of his Advisory Committee, has been involved in all facets of this work. His insight and encouragement have been very helpful in producing this work in the short time spent on it; his contributions are gratefully acknowledged. Dr. J.A. Schetz is thanked for suggesting and supervising the analytical work and also for his interest and timely suggestions regarding the experimental work. Dr. J.F. Marchman is thanked for taking interest in this work as a member of the advisory committee and also for the help rendered in Scheduling and running the VPI&SU Stability Wind Tunnel. The other members of the advisory committee, Dr. W.E. Kohler and Professor C.H. Long are thanked for their continued interest throughout the course of this work.

and are thanked for lending the equipments used in the experiments.

Special thanks are due to for the long hours spent on setting up the experiments and taking the data.

In addition, the author wishes to thank the following persons for their help during various stages of the experiments:

, and

Finally, the author wishes to thank his wife, for
moral support.

CONTENTS

ACKNOWLEDGEMENTS	i
LIST OF CONTENTS	iii
LIST OF FIGURES	
NOMENCLATURE	

Chapter	page
I. INTRODUCTION	1
II. WIND TUNNEL, EXPERIMENTAL SETUP AND INSTRUMENTATION	10
The Model	10
The Anemometer System	15
III. EXPERIMENTAL PROCEDURES AND TEST CONDITIONS	18
Probe Calibration	18
Influence of Temperature Variation	20
Test Conditions	21
IV. DATA REDUCTION	25
Single Wire	25
X-Wire	26
Error Analysis	29
V. EXPERIMENTAL RESULTS AND DISCUSSION	31
Single jet	32
Tandem plumes	36
Side-by-side plume	39
Some General Results	40
Frequency Spectra	44
VI. ANALYSIS	47
Governing Equations	47
Results	54
VII. CONCLUSIONS AND SUGGESTIONS	57
VIII. VITA	158

LIST OF FIGURES

Fig.	Title	Page
1	Diagram of jet in Cross-Flow	66
2	Pressure contours in the jet cross-section.	67
3	VPI&SU Stability Wind Tunnel	68
4	Diagram of the jets in tandem configuration.	69
5	Injection plate.	70
6	Hot-wire and tuft rake	71
7	Traverse System.	72
8	Single wire and X-wire probes.	73
9	X-wire sensors and coordinate system	74
10	Instrumentation for the first set of experiments.	75
11	Instrumentation for the second set of experiments.	76
12	Hot-wire calibration curve.	77
13	Voltage-velocity plot.	78
14	Voltage-sensor orientation plot.	79
15	Effect of temperature variation on voltage output.	80
16	Jet exit velocity profile.	81
17,18	Boundary-layer profiles on the injection plate.	82
19	Coordinate systems used for data plots.	84
20-25	U,u,v,w, $\tilde{u}\tilde{v}$ and $\tilde{u}\tilde{w}$ profiles. Single jet, X/D = 3	85
26-30	U,u,v,w and $\tilde{u}\tilde{v}$ profiles. Single jet, X/D = 7	91
31-36	U,u,v,w, $\tilde{u}\tilde{v}$ and $\tilde{u}\tilde{w}$ profiles. Single jet, X/D = 10	96
37-42	U,u,v,w, $\tilde{u}\tilde{v}$ and $\tilde{u}\tilde{w}$ profiles. Single jet, X/D = 14	102
43-47	U,u,v,w and $\tilde{u}\tilde{v}$ profiles. Tandem jets, X/D = 3	108
48-53	U,u,v,w, $\tilde{u}\tilde{v}$ and $\tilde{u}\tilde{w}$ profiles. Tandem jets, X/D = 10.	113

54-59	U,u,v,w,u \tilde{v} and u \tilde{w} profiles. Side-by-side jets, X/D = 3	119
60-65	U,u,v,w,u \tilde{v} and u \tilde{w} profiles. Side-by-side jets; X/D = 10	125
66	Comparison of U,u,v and u \tilde{v} variations for single and tandem configurations; X/D = 3.	131
67	Comparison of U,u,v,w,u \tilde{v} and u \tilde{w} variations for single and tandem configurations; X/D = 10	132
68	Comparison of U,u,v,w,u \tilde{v} and u \tilde{w} variations for single and side-by-side configurations; X/D = 10; Z/D = 0	133
69	Comparison of U,u,v,w, u \tilde{v} and u \tilde{w} variations for single jet (Z/D=0) and side-by-side jets (Z/D=-2); X/D = 10	134
70-74	Axial variations of U,u,v,w,u \tilde{v} and u \tilde{w} peaks . . .	135
75	Flow angles for single jet; X/D = 3	140
76	Flow angles for single jet; X/D = 10	141
77	Flow angles for tandem jets; X/D = 3	142
78	Flow visualisation of circulatory flow	143
79,80	Jet boundaries in side view and top view	144
81	Single jet power spectra in plane of symmetry . .	146
82	Single jet power spectra at Z/D = -2	147
83	Side-by-side jets power spectra Z/D = -2	148
84	Cartesian and natural coordinate systems	149
85	Entrainment coefficient	150
86,87	Drag coefficients of twin circular cylinders . . .	151
88-90	Single and Tandem jet trajectores	153
91	Trajectories of single and side-by-side jets . . .	156
92	Comparison of analysis and data for single jet. .	157

NOMENCLATURE

- A } cross-sectional area of the jet, constant in King's Law,
} intercept in hot-wire calibration plot
- B constant in King's Law
- C effective jet circumference
- C_D drag coefficient
- C_p specific heat at constant pressure
- D jet exit diameter
- d effective jet diameter
- ds infinitesimal length of jet control volume
- E } entrained mass per unit length of jet control volume,
} voltage
- E_0 voltage output for no flow condition
- e' fluctuating component of voltage.
- e rms value of the voltage fluctuations.
- E^* entrainment coefficient
- f frequency (Hz)
- g gravity
- h width of jet
- \bar{h} average film heat transfer coefficient
- K Sensitivity coefficient, $\delta E / \delta U$
- k correction for tangential component of velocity
- n constant in King's Law
- \bar{p} average static pressure of jet flow

q mean dynamic pressure of jet fluid flow
 R radius of curvature of jet trajectory
 Re_D Reynolds number based on D
 S_u velocity sensitivity of the voltage, $\partial E / \partial U$
 S_ϕ angular sensitivity of the voltage, $\partial E / \partial \phi$
 s, n natural coordinates along and normal to the trajectory
 T { mean cross-sectional temperature of jet fluid,
general expression for temperature
 VR effective velocity ratio
 U { general expression for velocity
axial component of the mean velocity
 U_∞ freestream velocity
 u')
 v') instantaneous values of the velocity fluctuations
 w')
 \bar{v} mean cross-sectional velocity of jet fluid
 u)
 v) rms values of the velocity fluctuations
 w)
 \tilde{uv} $\overline{u' v'}$
 \tilde{uw} $\overline{u' w'}$
 X)
 Y) cartesian coordinates
 Z)
 α inclination of the jet axis to the cross-flow direction

- β constant in expression for eddy viscosity
 θ flow angle in the vertical plane
 ρ mean cross-sectional density of jet fluid
 τ shear stress in s-direction acting on jet control volume
 ν kinematic viscosity
 ϵ eddy viscosity

Subscripts

- j jet flow conditions at injection point
 ∞ freestream conditions
c corrected for tangential velocity component
1 sensor number 1
2 sensor number 2
($\bar{\quad}$) Overbar indicates time averaged values

Chapter I

INTRODUCTION

Fluid Mechanics research workers often encounter problems in which one or more jets enter a cross-flow at large angles to the main stream. The lift jets of V/STOL aircraft is an example of jets in a cross-flow. Other examples of gaseous jets in a cross-flow are the gas injection into combustion chambers, the cooling jets on turbine blades, and the secondary injection in rocket nozzles for thrust vector control. In all these cases the jets enter the cross-flow at right angles to the main stream.

A different, but equally important area in which jets in cross-flow play a major role, is environmental pollution. A key factor in preventing coal from being used in alleviating the energy shortage, is the hazard from air pollution. Cooling tower plumes and pollutant discharges into rivers constitute other examples in this regard.

In most situations described above one encounters more than one jet in proximity to another. A knowledge of the jet behaviour in the examples cited above would be highly desirable from an engineering standpoint. In the case of coolant jets in combustion chambers, their effectiveness is dependent upon how fast the jets and the combustion gases

mix. The aerodynamic characteristics of the V/STOL aircraft will be greatly influenced by the behaviour of the deflected lift jets, and the thrust vector control effectiveness is dictated by the modification of the pressure distribution around the nozzle walls. The location of chimneystacks, the rate of discharge of pollutant etc. could be decided with greater confidence if one is able to determine the nature of pollutant dispersal.

There have been several analytical and experimental studies of a single jet exiting normal to cross flow (Refs.1-8). There have also been a few studies of multiple jets in a cross-flow (Refs.9,10). A review of some of the important ones among these is given below.

The early researchers in this field were concerned with velocity and pressure measurements on the experimental side, and a momentum integral approach on the analytical side. Abramovich (Ref.1) has given a detailed description of the processes involved in the deflection of a turbulent jet in a cross-flow. The early work of Russian reserchers is compiled in this excellent book. He observed that the jet cross-section deforms into a horse-shoe shape which could be approximated to an ellipse with a major axis to minor axis ratio of 5:1. A pictorial representation of the jet interacting with the freestream (from Ref.1) is shown in Fig. 1.

The deformation of the jet cross-section, the formation of the counter-rotating vortices and the presence of the potential core are shown in Fig.1. Fig.2, also from Ref.1, shows the total and static pressure contours and the potential core in the jet cross-section for different downstream stations. A very recent publication which deals with the subject is that of Schetz (Ref.2). More than a decade's effort by the author and his coworkers is discussed in this publication. An exhaustive survey of the work done by other researchers in the field is also given by the author. Keffer and Baines (Ref.3) studied the flow of a jet directed normal to a cross-wind; the position of the jet in space, when stretched by the ratio of jet to cross-wind momenta was described by a single function. They obtained a single functional behaviour for the axial jet velocity for various velocity ratios when the jet was considered to originate from a virtual source. They then deduced similarity in lateral velocity profiles when scaled by suitable length scales. Their entrainment function depended only on the difference in magnitude between the jet velocity and the freestream velocity. Hoult, Fay and Forney (Ref.7) based their studies on the conclusion of Jordinson (Ref.8) that mass entrainment is more important in the determination of the plume trajectory than drag; they postulated that there are basically two

entrainment mechanisms, one due to the difference between the jet velocity and the component of the freestream velocity parallel to the jet velocity, and the other due to the normal component of the freestream velocity. They, in addition, supposed that the two parts of their entrainment mechanisms are additive.

Campbell and Schetz (Ref.4) performed experimental and theoretical investigation of flow properties of submerged heated effluents in a waterway. Their analysis accounted for natural fluid behaviour such as entrainment, buoyancy, drag, and heat transfer. They obtained the jet cross sectional area as a part of the solution of the conservation equations rather than assuming a specific growth for the area. They found good agreement between the analysis and the experimental data available in the literature.

Although the integral methods give useful information about the gross properties of the jet such as the jet trajectory, jet velocity, bulk temperature, the growth of the jet cross-sectional area, they have the limitation of not being able to predict the detailed structure of the flow. Knowledge of the detailed flow structure within a deflected turbulent jet is desirable for two reasons. First, it may be put to use in applications discussed in the beginning of this section. The second, though not so direct, reason is

that it may open the door to a better understanding of the turbulence phenomena associated with three-dimensional free shear flows. As a result, more and more attention is being focused on the numerical solution of the equations of motion. Chien and Schetz (Ref.11) obtained exact numerical solutions for a three-dimensional buoyant jet in a cross-flow, using the steady state Navier-Stokes equations written in terms of velocity, vorticity and temperature with a Boussinesq approximation for eddy viscosity. Patankar, Basu and Alpay (Ref.12) numerically solved the elliptic equations for a deflected turbulent jet with the three velocity components and the pressure as the dependent variables. They used a two-equation turbulence model for the Reynolds stresses. A similar approach was also used by Jones and McGuirk (Ref.13) for the computation of a round turbulent jet in a cross-flow. Questions concerning adequate models for the Reynolds stresses, and computer storage and run times must be resolved before the numerical solution of the Navier-Stokes equations becomes attractive. The authors of Ref.12 suspect that the coarse mesh used in their solution procedure might have degraded their results.

The limitations of the numerical approaches have led researchers to the experimental investigation of the flow structure within a deflected turbulent jet. Kamotani and

Greber(Ref.5) reported results from experiments on both unheated and heated jets in a cross-flow. They presented longitudinal and transverse distributions of velocity, temperature, and turbulence intensity profiles. They found that the jet structure is dominated by a vortex wake which forms behind the jet. A detailed investigation of the circulating flow in the cross planes was also included in their study. Chassing, George, Claria and Sananes (Ref.14) experimentally investigated the physical characteristics of single and coaxial subsonic jets in a cross-stream. They confined their attention to the jet axes and the velocity profiles in the plane of symmetry of the flow. They defined the shape of the universal axial velocity profile as well as the law of the axial velocity decay and the laws of the variation of the thicknesses of the jet.

Crabb, Durao and Whitelaw (Ref.15) took detailed measurements of the characteristics of a round jet normal to a cross-flow. They used laser-doppler anemometry in the upstream region and hot-wire anemometry in the downstream region. The mean velocity, turbulence intensity and turbulent shear stress profiles were given for velocity ratios of 1.15 and 2.3. The results confirmed the double vortex character of the downstream flow. They also showed, by means of helium trace concentrations, that the region of high velocity is composed mainly of the freestream fluid.

The literature review presented so far deals only with single jets in a cross-flow; a review of the recent studies on multiple jets in a cross-flow indicates that the information available is very limited. Schwendemann (Ref.16) has given trajectory data for tandem jets in a cross-flow for normal and inclined injections, and for double jets arranged side-by-side for normal injection. Ziegler and Wooler (Ref.9) compared Schwendemann's (Ref.16) data with their analysis of multiple jets in a cross-flow. In their model the jet induced velocity was determined by a combination of sinks and doublets. They assumed that the leading jet is not influenced by the presence of the rear jet; the rear jet is modified by the reduced dynamic pressure behind the leading jet. Makiata and Miyai (Ref.10) performed experimental and theoretical studies on twin jets in a cross-flow. They followed a momentum integral approach in their analysis; their results do not identify individual trajectories for the front and the rear jets.

It is evident from the literature review presented above that wide gaps exist in the understanding of jets in a cross-flow, especially so in the case of multiple jets in a cross-flow. The present study was meant to close some of these gaps. The effort was directed at two fronts. The first one dealt with an experimental study concentrating on

the detailed structure of the flowfield. The single jet behaviour was first investigated; the data from this study was compared with the published data of Crabb et. al. (Ref.15). This afforded a qualitative check on the present experiments. The double jet characteristics were then looked into. It was felt that a thorough study of a few transverse planes would be more useful than skimming over several cases without extracting as much information as possible.

The experimental investigation consisted mainly of hot-wire anemometry; the axial mean velocity, the turbulence intensities in the three coordinate directions, and the Reynolds shear stresses in the vertical and horizontal planes were obtained from these measurements. A flow visualization study using tufts was performed to estimate the flow angles and the spread of the jets. One dimensional spectra was obtained for several stations using the single wire probe; this was intended to see if the energy spectra have any dependence on the parameters of the problem. Since no detailed experimental data exists to the best of the author's knowledge, this study was hoped to be a motivating first step towards the collection of a good amount of data on the subject.

The second part of the study was concerned with the analytical investigation of the gross properties of the jet by

extending the integral method developed in Ref.4. It was meant to complement the experimental work.

The present study being one of varied applications, no attempt was made to model any particular problem completely. Thus, the effect of boundary-layer, and the characteristics of the terrain, which may be important in atmospheric pollution problems, had to be left out in the present study. The thermal and chemical species diffusion characteristics which are significant in the case of cross-flow with chemical reaction, were also not looked into. Instead, emphasis was focused on the aerodynamic interaction of two equal and closely spaced jets, arranged in either tandem or side-by-side configuration, and exposed to a uniform cross flow.

Chapter II

WIND TUNNEL, EXPERIMENTAL SETUP AND INSTRUMENTATION

A brief description of the wind tunnel, the experimental setup, and the instrumentation is given in this chapter. The experiments were done in two phases and the instrumentation differed slightly for the two.

The testing was carried out in the VPI&SU Stability Wind Tunnel (Fig.3). The facility has a 1.82mx1.82m (6ft.x6ft.) test section, is 7.104m (23 ft.) long and the cross-section diverges slightly in the downstream direction. The tunnel dynamic pressure was indicated by a Barocel Electronic Manometer (Model 1173)¹ and the tunnel temperature was indicated on a digital thermometer² (Model 1563-83-115).

2.1 THE MODEL

Fig.4 is a schematic representation of the experimental setup in tandem configuration. The model consisted of the plenum chamber, the nozzle, and the injection plate. A DC blower³ provided a steady supply of air, the mass flow rate

¹ Manufactured by Datametrics.

² Manufactured by Instrulab Inc.

³ 1400 CFM at 13" PS. JOY, P/N, AVR 90-75D, 27 VDC, 175 amp. Motor 4.4 HP, 7500RPM. Distributed by C&H Sales.

of which could be regulated by varying the input voltage to the blower. The blower was followed by a 15.24cm(6 in.) long conical converging section which had a small end internal diameter of 15.24cm(6in.). The conical section was connected to a plenum chamber which was fitted with a flow straightener and four fine mesh screens. The plenum chamber was made of PVC pipe 38cm (15 in.) long and 15.24cm(6in.) internal diameter. The flow straightener was made of 3.81 cm (1.5 in.) long and 0.635 cm(0.25in.) diameter tubular pieces cut from commercial drinking straws. One of the jets had a 30 deg elbow between the conical section and the plenum chamber. This was provided in order to bring the jets close together so as to have a minimum spacing of 4 jet diameters.

The nozzle was machined out of laminated plexiglass and the surface had a very smooth finish. The nozzle had a contraction ratio of 8.4 and a throat diameter of 5.08cm (2in.). The nozzle was 12.7 cm (5 in.) long , and the contour was a compromise between the Batchelor-Shaw and the Cubic Equation nozzles. This contour is reported to give uniform flow at the nozzle exit with low turbulence intensity (Ref.17). The last 2.54cm (1in.) of the nozzle length had a uniform cross-section of 5.08 cm (2in.) diameter. Two static pressure ports, one at the entrance to the nozzle and

another at the exit were used for static pressure measurements. The jets were strapped together to ensure that the jet exit surfaces lay in the same plane and the jet axes were parallel to each other. The nozzles were made to fit flush with the top surface of the injection plate.

The injection plate was made of 183cmx183cmx1.91cm (6ft.x6ft.x0.75in.) plywood with a formica laminate glued on top (Fig.5). The leading edge of the injection plate was rounded, coated with epoxy and sanded to a very smooth finish. A 22.9cm (9in.) wide T-shaped slot was cut on the injection plate (See Fig.5) and several 22.9cm (9in.) wide plywood pieces of varying lengths were used as spacing blocks; this arrangement provided a convenient means of changing from tandem to side-by-side configuration and vice-versa and varying the jet spacing in the two cases. The large area of the injection plate prevented any vortices at the edges from rolling up and 'contaminating' the jet flow. The injection plate was fixed at 58.4cm(23in.) above the tunnel floor. A shield with a rounded leading edge and a tapered trailing edge extended from the injection plate to the tunnel floor covering the jets, thus reducing the disturbances in the flow.

A hot-wire rake (Fig.6) which could accommodate three probes was specially made for the present set of experi-

ments. The rake was mounted on an aerodynamically smooth aluminum bar which could be fixed to a traverse system. The rake was designed such that the probes could be fixed at any angle to the freestream; this arrangement was found to be extremely useful for probe calibration and making fine adjustments for taking measurements. The aluminum bar was 61cm (24in.) long and was fixed at 45 deg with respect to the horizontal direction (See Fig.6) keeping the traverse sufficiently behind the measurement station, thus avoiding flow interference. The rake could be moved up and down, and sideways by means of the traverse system(Fig.7) fitted with electric step motors. The least counts of the traverse in the vertical and horizontal directions were 0.1cm(0.0394in.) and 0.0254cm (0.01in.), respectively. The traverse system could move much faster in the vertical direction than in the horizontal direction. It had a travel of about 1.25m.(4 ft.) in both directions; therefore the entire flowfield could be mapped without difficulty. Prior to operating the traverse, it was calibrated for a reference position. To move the traverse in the vertical direction, the desired travel was set on a counter and the on-button was pressed. The motor would stop automatically at the desired position. The horizontal traverse was less automated; but essentially performed in the same manner as the vertical traverse. The

control panel had a switch for left and right motion and the position was indicated on a counter. The counter had independent on-off control; therefore, any desired value could be set for the reference position. The motion was manually stopped when the counter showed the desired position; this was easy because of the slow lateral motion of the traverse. From the above description it is evident that it was easier to make vertical scans during measurements.

Two types of probes were used in the present investigation namely, single wire and X-wire probes (See Fig.8). The single wire probe was used to measure the mean flow and the turbulence intensity in the axial direction. The two sensors of the X-wire probe, oriented at 90 deg to each other (Fig.9) could detect mean flow and turbulence intensities in two perpendicular directions; the shear stress in the plane of the sensors was subsequently calculated, as described in 'DATA REDUCTION'

The probes used were TSI 1210 (single normal wire) and TSI 1241 end flow X-probe (Fig.8). The sensors were .00058 cm (.0002 in.) in diameter and 0.127 cm (0.05 in.) in length. The probe dimensions are as shown in Fig.8.

2.2 THE ANEMOMETER SYSTEM

The selection of the instruments used was dictated by availability. Fig.10 shows a line diagram of the instrumentation for the first set of experiments; and Fig.11 shows the instrumentation for the second set of experiments.

The TSI 1050 Anemometer used in the present experiments has very low noise (less than 0.007% equivalent turbulence intensity). The TSI Model 1755 Constant Temperature Anemometer, used in conjunction with the single wire probe, is a simple modular unit which has comparable noise and temperature drift specifications with the TSI bench type anemometers. It uses a 15 volt power supply and an external control resistor. The DISA Type 55D01 anemometer was used in the constant temperature mode at a bridge ratio of 1:20.

The TSI Model 1052 linearizer is designed to linearize the output from a constant temperature anemometer and to serve as a general purpose function shaper. It is done by approximating the curve by a fourth degree polynomial. The DISA Type 55D10 linearizer is the exponential type.

the TSI Model 1015C correlator performs a number of analog computations. The four positions on the output knob enable the user to read the two input signals (eg. from an X-wire), their sum and difference. It will be shown in a later chapter, how these quantities are used in the calcula-

tion of Reynolds Stresses. The DISA Type 52B25 Turbulence Processor is a small analog computer; its function in the present study was the same as the TSI Model 1015C Correlator.

The 6ft. Stability Tunnel Data Acquisition System was used to perform online hot-wire calibration, which is described in a later section, as well as to record the DC signals from the hot-wire sensors on magnetic tape. The Data Acquisition System consisted of an HP 3495A channel selector, HP 3455A Digital Voltmeter, HP 9825A computer and an HP 9872A plotter. The voltmeter had a sampling rate of about 20 samples per second. Each voltage signal from the anemometer was sampled for three seconds and the average, maximum, and minimum were recorded on magnetic tape.

The Hewlett Packard 3580A spectrum analyzer used in the present experiments is a low frequency, high performance analyzer with a band width of 1 Hz.

A tuft wire was used for flow visualization in order to estimate the flow angles and the spread of the jet. The tuft wire was held taut on a tubular frame (See Fig.6). The frame was moved from place to place in the flowfield using the traverse system and the tuft wire was photographed at each position. Since the tufts were fluttering about a mean position, the pictures were taken at a slow shutter speed

(1/30sec.); the pictures, therefore, provided the mean positions of the tufts.

The mean velocity profiles in the boundary-layer on the injection plate were obtained with a rake of fine pitot tubes. The rake was approximately 3.8cm (1.5in.) high with one static pressure port and 24 total pressure tubes staggered at increased spacing with distance from the wall. The rake was mounted on the injection plate at the same downstream coordinates as the leading edges of the front and rear jets. The output pressures from the pitot rake were measured by using a Scanivalve System* which consisted of four components: Scanivalve model D, pressure transducer model 237, power supply model B24-1.2, and electromagnetic counter model 177004020. The transducer output was fed to the Data Acquisition System and the results were plotted on-line (Figs.17 and 18).

* Manufactured by Scanivalve, Inc.

Chapter III

EXPERIMENTAL PROCEDURES AND TEST CONDITIONS

This chapter describes the experimental procedures adopted for the present study. Three equally spaced probes -two X-wire probes on either side and a single-wire probe in the middle- were used in the experiments. The X-wire probes were arranged in the vertical and horizontal planes respectively. The use of three probes considerably reduced the time needed for taking the data.

3.1 PROBE CALIBRATION

The single wire probe was calibrated by online computation of the exponent in the King's Law relationship. A typical calibration curve is shown in Fig.12. This is a plot of $\log U$ Vs. $\log [(E/E_0)^{**2} - 1]$; a straight line is fit into these points by a least square curve fitting routine. The slope of the stright line gives the value of n in the King's Law relation. (Eq.2). Typically the number of points used in the calibration was between 8 and 15. Care was taken to have several points in the range of velocities that would be encountered during actual measurements.

Two methods are described for the X-wire calibration - one for the case for measurements with the correlator/turbulence processor and the other without.

In the first method, each sensor of the X-wire was aligned normal to the flow and the linearized output of the anemometer was made to read zero for no flow and 10 volts for a velocity of 190 ft./sec. This particular value of 190 ft./sec. was chosen because of the availability of the linearizer coefficients for the 0-190 ft./sec. velocity range. The linearizer output was checked at several intermediate speeds and the maximum deviation from linearity was found to be less than 1%.

The second method was more involved; first, the DISA Type 55D01 anemometer was linearized using the DISA Type 55D10 exponential linearizer. The linearizer exponent was determined by the same method as for the single wire. The output from the linearizer was then normalized to give zero voltage at zero velocity and a full scale deflection of 10 volts at 190 ft./second. The velocity sensitivity of the sensors were then determined by making measurements at different known speeds and plotting the results. (See Fig.13). The angular sensitivity of the sensors was determined by taking measurements at five different sensor orientations (39 , 42 , 45 , 48 , and 51 deg) to the freestream. This procedure was repeated at three different speeds namely, 50 ft./second, 100 ft./second and 150 ft./second (Fig.14).

All the anemometers were operated at an overheat ratio of 1.8.

3.2 INFLUENCE OF TEMPERATURE VARIATION

The output of an anemometer may be represented by the well known relationship

$$E^2 = (A + BU^{1/n}) (T_s - T_e) \quad (1)$$

Where E is the anemometer output voltage, U is the velocity, T_s is the sensor temperature and T_e is the temperature of the airstream. A and n are constants. It is readily seen from this equation that in order that the output voltage E to be a true representation of the velocity, the temperature, T_e must remain constant. The temperature of the airstream could not, however, be controlled at will. It was felt necessary to address this question more systematically and come up with some correction factors, if possible. Voltage output - velocity plots were made at different tunnel temperatures, the measurement being taken over a period of several days so as to have as wide a temperature range as possible (Fig.15). Fig.15 shows two curves for sensor number 1 of the vertical X-wire. The one with temperatures near 40 deg F is the calibration curve, and the other with temperatures near 0 deg F is an extreme case which was ob-

tained due to an unusual drop in the ambient temperature towards the end of the experiments. The rest of the curves were all close to the calibration curve and are not shown so as not to lose clarity. A linear relationship between the velocity and the temperature change ΔT was thought to be adequate for small variations from the nominal (calibration) value. An estimate of the deviation from the calibration curve was made; the result of this estimate is shown by the shaded area in Fig.15. This shaded area corresponds to a temperature variation of ± 5 deg F. All the data points lie within this shaded area. A 5 deg. F change in the temperature of the airstream corresponds to 8% change in the velocity. Therefore, the maximum correction applied to the mean velocity due to changes in the ambient temperature was 8%.

3.3 TEST CONDITIONS

The jets were tested independently to determine the velocity profile at the jet exit. Fig.16 shows a sample plot from these tests. As expected it is a top-hat profile, the maximum deviation from the mean value being 1.5%. Several tests were made with both the jets at different azimuthal angles, the differences among them being hardly noticeable. It is also worth noting that the 30 deg elbow on the second jet does not alter the velocity profile at the jet exit.

With the model in position, but without the jets blowing the freestream had a maximum deviation in mean velocity of 0.6% and a maximum turbulence intensity of 0.04%. The mean flow inclination in the same configuration was slightly less than 0.5 deg above horizontal.

The results of the boundary-layer survey are shown in Figs.17 and 18. It can be seen that, for the freestream velocity of 50 ft./sec. used in the present experiments, the boundary-layer was approximately 0.45in. and 0.6in. thick at the two stations corresponding to the leading edges of the tandem jets spaced at 4D.

All the data were taken at a freestream velocity of 50 ft./sec. which corresponded to a Reynolds number based on jet diameter, of 0.56×10^5 .

Corrsin and Uberoi (Ref.18) have reported that temperature changes may considerably affect the jet characteristics. For the present study it was found that the jet air temperature was about 4 deg F higher than the room air temperature. The tunnel air temperature varied somewhat during the long periods of tunnel operation. The maximum difference in the temperature between the tunnel air and the jet air was 20 deg F.

The present study has been undertaken mainly to gain insight into the interaction, mixing and growth of multiple

jets in a cross-flow. One can easily see that the parameters involved in this situation are numerous - the jet to freestream velocity ratio, the Reynolds number based on the jet diameter, the jet spacing, and the jet configuration (tandem vs. side-by-side etc.) are to name a few. Therefore, it was necessary to restrict the study to a few aspects of the problem. A separation distance of four jet diameters and a velocity ratio of two were chosen for the present study. These values were thought to be representative of many engineering situations involving jets in a cross-flow. Data were taken for single jet, tandem plume and side-by-side plume configurations. The selection of the downstream stations at which data were taken, was dictated by two inherent limitations of the hot-wire anemometry. First, hot-wire data become increasingly unreliable for high turbulence intensities ($>30\%$). The second major limitation of hot-wire anemometry is the inability to detect reverse flow. There is also the necessity to have the axis of the X-probe aligned with the mean flow direction. A preliminary survey of the flowfield using tufts indicated that a minimum downstream distance of $3D$ (See Fig.19) would give flow angles less than 20 deg. above horizontal. Therefore it was decided not to take data anywhere upstream of this station. Thus, two downstream stations of $3D$ and $10D$ were selected

for the double jet case. Four downstream stations namely, 3D, 7D, 10D and 14D were chosen for taking data for the single jet case. These stations are shown in Fig.19.

Chapter IV
DATA REDUCTION

This chapter describes the methods used for reducing the data. It was explained earlier that the single wire signal was not linearized; the data were, therefore, calculated from the nonlinearized signal. For reducing the X-wire data two methods were used; they corresponded to the two types of instrumentation used in the experiments.

4.1 SINGLE WIRE

King's Law states that

$$E^2 - E_0^2 = BU^{1/n} \quad (2)$$

Where E is the anemometer output voltage and E_0 is the voltage corresponding to zero velocity; n is an empirical constant. Differentiating the logarithm of both sides one gets

$$2E \, dE / (E^2 - E_0^2) = \frac{1}{n} \, dU/U \quad (3)$$

Under the assumption of small fluctuations one can write the rms value of the voltage fluctuation, e as the deviation dE from the time averaged value of the voltage E and the rms value of the velocity fluctuation u as the deviation dU from the mean velocity U . Therefore

$$\frac{u}{U} = \frac{2n E e}{E^2 - E_0^2} \quad (4)$$

E_0 and n were calculated from the calibration experiments of the sensor. The axial mean velocity is computed from the calibration curve of the single wire. The equation for the line may be written as

$$\ln U = n \ln \left[\left(\frac{E}{E_0} \right)^2 - 1 \right] \quad (5)$$

4.2 X-WIRE

The method of Champagne et al. (Ref.19) was used to reduce the data taken with a correlator/turbulence processor. The equations used are as follows (Ref.19).

$$U = \frac{\overline{E_1 + E_2}}{\sqrt{2K \left(1 + \frac{1}{2}k^2 - \frac{1}{8}k^4 \right)}} \quad (6)$$

$$\left(\frac{u}{U} \right)_c = \frac{\sqrt{\overline{(e'_1 + e'_2)^2}}}{\overline{(E_1 + E_2)}} \quad (7)$$

$$\frac{v}{U}_C = \left[\frac{(1+k^2)}{1 - 3k^2 + 4k^4} \right]^{1/2} \frac{\sqrt{(\overline{e'_1 - e'_2})^2}}{(\overline{E_1 + E_2})} \quad (8)$$

$$-\frac{\overline{uv}}{U^2}_C = \left(\frac{1+k^2}{1-k^2} \right) \frac{\overline{e'_2{}^2} - \overline{e'_1{}^2}}{(\overline{E_1 + E_2})^2} \quad (9)$$

where u and v are the rms values of the fluctuating velocities in the two perpendicular directions; \overline{uv} is the Reynolds shear stress. Subscripts 1 and 2 refer to the two sensors in Fig.9. K is the sensitivity coefficient whose value was set during calibration and k is the correction factor for tangential component cooling. Its value was taken to be equal to 0.2 as suggested in Ref.19 for the sensor dimensions of the probes used in the present study. Subscript c denotes values corrected for the effect of tangential velocity component. The output of the correlator gives the individual values of the instantaneous voltages from the two sensors, their sum and difference; the mean and the rms values of these four quantities were subsequently obtained using the Data Acquisition System and the rms meter. These quantities are used in Eq.6-9 to yield the mean flow and the turbulence quantities. The overbar denotes temporal means.

For the cases of $X = 3D$ (single jet), $X = 7D$ (single jet) and $X = 3D$ (tandem jets) the sums and differences of the horizontal X-wire signals could not be directly measured

because the turbulence processor was not available for the corresponding part of the measurements. The data reduction, therefore, was done by combining the single wire and X-wire information. This procedure required that data be taken at the same locations by the X-wire and the single wire probes; this placed a restriction on the probe spacing in relation to the interval in the lateral direction, at which data were taken. A probe spacing of 3.0 cm (1.18in.) was chosen for the first set of experiments and 2.54cm (1in.) for the second set, and data were taken at intervals of 1.5cm(0.59in.) and 1.27cm (0.5in.) for the two jets, respectively.

The expressions for the fluctuating voltages from the sensors of an X-wire inclined at +45 deg and -45 deg (See Fig.9) are as follows

$$\overline{e^2}_{+45} = (S_u)_{+45}^2 u^2 + 2(S_u)_{+45} (S_\phi)_{+45} \overline{uw} + (S_\phi)_{+45}^2 w^2 \quad (10)$$

$$\overline{e^2}_{-45} = (S_u)_{-45}^2 u^2 + 2(S_u)_{-45} (S_\phi)_{-45} \overline{uw} + (S_\phi)_{-45}^2 w^2 \quad (11)$$

where S_u and S_ϕ are velocity and angular sensitivities respectively. Subscripts +45 and -45 denote sensor orientations with respect to the probe axis. In the above two

equations the unknowns are u , w , and $\tilde{u}w$. The axial turbulence intensity, calculated from the single wire measurements is used to reduce the number of unknowns to two. The two equations are then used to solve for the two unknowns w and $\tilde{u}w$.

4.3 ERROR ANALYSIS

A difficult, but important aspect of any experimental work is the estimation of error bounds for the experiments. An attempt is made here to identify the sources and magnitudes of the errors associated with the present experimental work.

The overall error in measuring the tunnel speed was estimated to be 1.8% at 50 fps. The tunnel dynamic pressure corresponding to 50 fps. was calculated periodically to account for changes in the ambient temperature and pressure. The maximum drift in the jet dynamic pressure was observed to be 0.15 in. of water which corresponded to 4 ft./second at the jet speed of 100 ft./second. Thus the maximum error in the jet speed was estimated to be 4%.

The error estimates of the hot-wire data are largely based on previous experience; they are estimated to be within 2-3% for the mean flow and 3-6% for low and medium turbulence intensities (<20%); however, the accuracy of the hot-

wire data deteriorates rapidly for high levels of turbulence. Therefore, it was felt that the numerical values of the data corresponding to $X/D=3$ for all the three configurations should be interpreted with caution.

Chapter V

EXPERIMENTAL RESULTS AND DISCUSSION

The experimental results from the hot-wire anemometry, spectral analysis, and the flow visualization are presented in this chapter. The hot-wire data in Figs.20-65 are given as variations along vertical lines for different transverse positions. Each figure covers the data for one plane normal to the freestream direction. First the single jet data are presented for the four downstream stations. This is treated as the base-line case for the double jet data. The differences among them are discussed and the underlying reasons for the observed behaviour are explored.

Figs. 20 to 65 show vertical distributions of the mean velocity and turbulence parameters for the configurations studied namely, single jet for $X/D = 3, 7, 10$ and 14 , tandem jets for $X/D = 3$ and 10 , and side-by-side jets for $X/D = 3$ and 10 . The coordinate systems used for presenting the data and discussion of the results for the three configurations are given in Fig.19. The jet spacing for the tandem and the side-by-side configurations was $4D$, and the velocity ratio, $VR (V_j / U_{\infty})$, was kept at 2 for all the cases studied.

5.1 SINGLE JET

Fig. 20 shows the mean velocity plot at $X/D = 3$ for a single jet. The distribution shows that the axial mean velocity, U decreases and then increases to a peak and subsequently reaches a constant value. The trough as well as the peak move toward the injection surface with increasing distance from the plane of symmetry. This confirms the observation of earlier investigators (Ref.1) that the outer edges of the jet bend more rapidly than the center region because of the increased interaction of the jet with the cross-flow at the outer edges. The minimum velocity is less than 50% of the freestream value in the region of the plane of symmetry; however, the peak is only slightly in excess of the freestream value. This observation indicates that at this low velocity ratio the cross-flow interacts with the jet rapidly and intensely, destroying the jet momentum to a large extent. The similarity plots of previous investigators (Ref.3) show a velocity excess for the jet; however, some have indicated that the similarity laws may not be applicable for low velocity ratios such as the present. All the curves for $Z/D = 1.48$ and above of Fig. 20 show values of U/U_{∞} near the injection surface slightly higher than the asymptotic value; this may be the result of the jet blockage and the subsequent acceleration of the freestream around the

jet. Fig. 21 shows the vertical distribution of the axial turbulence intensity for different transverse stations. It may be observed from Figs. 20 and 21 that the low axial mean velocity and high axial turbulence intensity occur in the same region above the injection surface, the trend is the same for the distributions of vertical and transverse turbulence intensities (Figs. 22 and 23). The region of increased turbulence intensities can therefore be characterized as the wake of the jet. It is useful at this stage to define a transverse width for the jet; the most convenient one is to call the edge of the jet as the station where the velocity defect disappears. Such a definition would yield 3 diameters as the transverse width of the jet for the case under discussion.

Fig. 24 is a plot of the variation of the Reynolds Stress $-\tilde{u}\tilde{v}$ for various transverse stations. The transverse stations near the plane of symmetry show two troughs and one peak. As one moves away from the plane of symmetry, the first trough gradually disappears leaving one trough and one peak. Comparison of Figs. 20 and 24 show that negative mean velocity gradient is associated with negative shear stress and positive mean velocity gradient associated with positive shear stress. It is, however, not possible to state with complete certainty that there is perfect correlation between the mean velocity gradient and the Reynolds shear stress.

Fig. 25 is the distribution of the Reynolds stress $-\tilde{u}\tilde{w}$. The distribution at $Z = 0$ shows a small negative value for small values of Y/D , though symmetry demands that $\tilde{u}\tilde{w}$ be zero in the plane of symmetry. This small deviation from symmetry may be attributed to imperfections in geometry and symmetry of the jet configuration. The lateral shear stresses in Fig. 25 are in general smaller than the vertical shear stresses in Fig. 24. This may be a consequence of the jets being much wider in the lateral direction than in the vertical direction; a fact which results in smaller mean velocity gradients in the lateral direction.

Figs. 26-30 show the flow property variations at $X/D = 7$ for the single jet case. The data for this station show less scatter compared to the previous case. The mean velocity distribution is much flatter in comparison to the case for $X/D = 3$, indicating that considerable exchange of momentum between the jet and the freestream has taken place between these two stations. The mean velocity peak is almost non-existent, and the maximum value of the axial turbulence intensity has come down by nearly half. The vertical turbulence intensity profiles show slower decay with downstream distance. The transverse turbulence intensity profiles show values much higher than its axial and vertical counterparts.⁵ The Reynolds stress profiles in the vertical plane

at this station are similar to the ones at $X/D = 3$; however, their peaks are flatter at this station.

The single jet data for $X/D = 10$ are plotted in Figs.31-36. The velocity excess in the mean velocity profile has almost completely disappeared at this station; the jet width in the vertical direction has grown to about $4D$. In the lateral direction the jet boundary extends to about $2.75D$ from the plane of symmetry. The turbulence intensity profiles have a maximum value of about 25% at this station and show near isotropy. The observation in Ref.15 that the turbulence intensity in the lateral direction is higher near the wall is confirmed by the w profiles in Fig. 34. The transverse turbulence intensity profiles on either side of the plane of symmetry are nearly symmetrically distributed; this confirms that the jet flow was approximately symmetrical about the geometric plane of symmetry.

The behaviour of the single jet at $X/D = 14$ (Figs.37-42) is very much similar to the previous station, $X/D = 10$. The Reynolds stresses are further reduced; the width of the jet is increased; and isotropy is more predominant. The verti-

⁵ The lateral turbulence intensity(w) and the lateral shear stress(\overline{uw}) corresponding to $X/D = 3$ and 7 for the single jet and $X/D = 3$ for the tandem jets were obtained by combining the single wire and the horizontal X-wire information. These data are, therefore, less reliable and may account for the scatter as well as the large values.

cal shear stresses at this station are seen to be higher than the lateral shear stresses. The lateral width of the plume is about $7D$ at this station.

5.2 TANDEM PLUMES

The single plume data of the present investigation serve as base-line cases for the tandem plume and the side-by-side plume configurations.

The data for the case of $X/D = 3$ are presented in Figs. 43-47. Several observations may be made regarding the distribution of the flow properties for this case. The profiles are flatter and have widths larger in comparison to the single jet at $X/D = 3$ and $X/D = 7$. The dip in the mean velocity is seen to be much smaller in the case of the tandem jets vis-a-vis its individual counterparts. This behaviour may be caused by the velocity excess of the rear jet compensating in part, the velocity defect of the leading jet. The maximum value of the axial turbulence intensity is less for the tandem jet in comparison to the single jet at $X/D = 3$; The corresponding maximum values of the vertical turbulence intensity are nearly the same. The mean velocity peak is shifted upward in comparison to the single jet at $X/D = 7$. It should be noted that the rear jet retains a large part of the vertical momentum because of the shielding

effect of the leading jet. The rear jet thus, may be considered to be "pushing" the trajectory upwards (See Fig.75 for a pictorial representation of the jets interacting). Surprisingly, the mean velocity and the turbulence intensity profiles do not show individual peaks for the two jets, indicating that the two jets have merged completely at this station. The vertical shear stress distribution of Fig.47 shows patterns completely different from the single jet cases of $X/D = 3$ and $X/D = 7$. The troughs and crests are less pronounced and the variations are less smooth especially near the plane of symmetry. For the stations, $Z/D = 0$ and 0.3 only a very flat trough exists in the vertical shear stress profiles. For $Z/D = 0.87$ and higher, the $-\tilde{u}\tilde{v}$ profiles show both a peak and a trough which are similar to the ones for the single jet. Comparison of the mean velocity profile in Fig.43 and the vertical shear stress profiles in Fig.47 shows that large values of turbulent stress are associated with steep gradients in mean velocity and small values of turbulent shear stress associated with flatter mean velocity profiles. A more precise relationship with respect to their signs does not appear to exist, at least for this station. The small positive values for the horizontal shear stress in the plane of symmetry are likely to be arising from the slight asymmetry in the flow.

The tandem plume data for $X/D = 10$ are given in Figs.48-53. The dip in the mean velocity profile in Fig.48 is more pronounced than the previous case of $X/D = 3$ and the single jet case of $X/D = 14$. The axial turbulence intensity profiles near the plane of symmetry show slight differences in shape when compared to the single jet data for the corresponding cases. The vertical turbulence intensity profiles in Fig.50 are very similar in shape to that of the axial ones; however, their values are in general higher. The lateral turbulence intensity profile of Fig.51 show marked differences from their axial and vertical counterparts. They are higher near the injection surface in the region of the plane of symmetry. In Fig.52 well defined profiles of vertical shear stress are seen; the troughs and peaks in this case are sharper than the single jet case and the magnitudes are seen to be higher than that of single jet cases of $X/D = 10$ and 14. The horizontal shear stress profiles of Fig.53 show very small values. The overall picture that emerges from Figs.48-53 is that, despite differences in details, the distributions of the flow properties for this case are very much similar to the single jet property distributions. This is a revealing observation because it points to the possibility that the downstream behaviour of the jets, whether single or double, may be dominated by the two counter-rotating vortices.

5.3 SIDE-BY-SIDE PLUME

The comparison of the flow properties of the side-by-side plume (Figs.54-59) with that of a single jet for $X/D = 3$, shows several interesting features of the problem. The distribution of the properties in the outer regions ($Z > 0$ in Fig.19b) are similar to that of the single jet for the same X/D . However, in the region between the two jets ($Z < 0$), the effects of the interaction of the jets are evident. The mean velocity profiles in Fig.54 show a rather pronounced velocity excess even in the plane of symmetry ($Z/D = -2$). The turbulence intensities are large just as the single jet case for $X/D = 3$. The shape of the tranverse turbulence intensity profiles in the region around the jet center in Fig.57 is very much different from that of the axial and vertical turbulence intensity profiles in Figs.55 and 56. It is interesting to note that at this station the vertical shear stresses are smaller than the lateral shear stresses; a trend which gets reversed for higher values of X/D . The low values of the mean velocity together with the high turbulence intensities near the injection surface indicate that this is a region of intense mixing. The two vortices associated with the jets interact in this region creating high levels of turbulence.

For the station, $X/D = 10$, the mixing region between the two jets, characterized by the low mean velocity and high turbulence intensities, is still present (Figs.60-65). For regions away from the plane through the jet center ($Z > 0$ in Fig.19b), the influence of the second jet is hardly noticeable. However, just as in the previous case of $X/D = 3$, for regions between the two jets the flowfield is considerably modified near the injection surface. In Fig.63, the lateral turbulence intensity profiles for $Z/D = -3$ and $Z/D = -1$ show nearly the same distribution confirming that the flowfield was symmetrical about the geometric plane of symmetry.

5.4 SOME GENERAL RESULTS

Figs.66-69 show comparison of the flow properties for the different configurations. Fig. 66 shows the variation for $X/D = 3$. The mean velocity plots of Fig.66a show the different distinct regions. The wake of the jet is indicated by the low velocity region; it is followed by the sharply rising region which is the lower edge of the jet. The center of the jet itself is shown by the peaks. The rear jet ($X/D=3$) shows the highest peak. It is interesting to note that the plume spreads apart in the case of the tandem configuration and the peaks and the troughs are flatter. The upward shift of the plume is also evident in Fig.66. The

axial turbulence intensity profiles are shown in Fig.66b, and the vertical turbulence intensity profiles in Fig.66c. A major observation here is that the tandem plume peak values are smaller than the single jet case at $X/D = 3$. The shear stress distribution (Fig.66d) for the double jet case is less smooth when compared to that of the single jet case.

Fig.67 shows distributions of the flow properties in the plane of symmetry of the single and the tandem jets for $X/D = 10$. All the variations are smooth and the increased spread of the tandem jets is clearly seen in all the six parts of Fig.67. The lateral shear stress, $\tilde{u}w$ is seen to be very small.

Fig.68 shows the all the flow property distributions through one of the jet centers ($Z=0$ in Fig.19b) for the side-by-side jet case for $X/D=10$; the single jet data are also given for comparison. There are only small differences between the single jet and the double jet cases except for the lateral shear stress near the injection surface for the double jet case. The jets, therefore, may be considered to have little influence on each other for this jet spacing at least as far as the flow property variations within the jet are concerned.

The distributions in the plane of symmetry for the side-by-side case ($X/D=10$) are given in Fig.69 along with the

single jet data in the plane 2D to the right of the plane through the jet center. These curves show that the flow properties are different not only in magnitude but in the shape of the variations as well. Most of the differences between the two configurations are confined to the region near the injection surface.

Figs.70-74 give axial variations of the peak turbulence parameters in the plane through the jet center for the three configurations. The axial turbulence intensity shows much faster decay for the single jet case in comparison to its vertical and lateral counterparts (Figs.70). Since data for only two stations are available for the tandem and the side-by-side configurations, not much can be said about the axial variations of the flow properties for these cases. The turbulence intensities in the three coordinate directions are in general higher for the tandem and the side-by-side cases in comparison to the single jet case (See Figs.70-72). In Figs.73-74 the axial variations of the Reynolds shear stresses are presented.

Figs.75-77 show flow angles in the vertical plane for a few cases. These were calculated from the DC signals of the vertical X-wire sensors; the limitations of the hot-wire anemometry apply to these plots. In particular, large flow angles (>20 deg) could not be measured accurately. Also,

the accuracy of measurements at the points, where both the vertical and the horizontal angularity were relatively large, may not be good.

The freestream, the jet and the wake can be distinguished from these plots and the corresponding mean velocity plots (eg. See Figs.20 and 75). For the stations investigated in this program, The wake shows low values of flow angles. The jet region (corresponding to high values of the mean velocity in Fig.20) show flow angles of about 10 deg. It is also worth noticing that the flow angles are smaller farther away from the plane of symmetry; this may be, at least partly, due to the jet periphery bending more rapidly than the center.

For the single jet case at $X/D = 10$ the flow angles in the vertical plane(Fig.76) show positive values near the center and negative values towards the edges. This behaviour was also observed in the flow visualization pictures (Fig.78). This confirms the establishment of the pair of counter-rotating vortices .

Fig.77 shows large values of flow angles (maximum of about 20 deg) in the plane of symmetry, probably caused by the upward shift of the trajectory.

The flow angle data in general have larger scatter in comparison to the turbulence property data. Mean flow data

from hot-wire anemometry are known to be less reliable than turbulence data ; this may explain the increased scatter in the flow angle data.

The jets in side view and top view are shown in Figs.79 and 80. The jet boundaries in these plots were determined from the flow property variations and the flow visualization studies. The single jet trajectory is shown by the dotted lines in Fig.79. The marked straightening of the rear jet trajectory due to the presence of the leading jet, the upward shift of the merged jet trajectory, and the larger spread of the merged jets in the vertical direction can be seen in Fig.79. The lateral spread of the jets for the three configurations is shown in Fig.80. The jets in tandem have a slightly larger lateral spread when compared to the single jet.

5.5 FREQUENCY SPECTRA

This section describes a preliminary (very limited in scope) investigation of the turbulent energy spectra.

One dimensional energy spectra (streamwise component) were measured at several points across the single jet and side-by-side jets to provide a picture of the spectral energy distribution. The spectra were plotted as rms voltage e versus the frequency f using a resolution band width of 30

Hz and 200 second sweeping time. Fig.81 shows the spectra corresponding to $Z/D = 0$ (See Fig.19a) for the single jet. In all the spectra in Fig.81 corresponding to different values of Y/D , the energy is distributed in the range of 100 Hz to 300 Hz with a major peak around 150 Hz. The distributions are Gaussian-like above and below the jets. In the spectra in Fig.82, corresponding to the station, $Z/D = -2$ (See Fig.19a) for the single jet a smaller hump to the right of the major peak can be seen. This may indicate some kind of periodicity in the corresponding flow region. It is possible that this periodicity is related to the side vortices convected downstream by the jet.

The spectra corresponding to the side-by-side jet configuration, were taken at only three locations; they are shown in Fig.83. These spectra indicate the existence of somewhat broadened high-energy frequency range, as well as humps to the right and/or left from the major peak. These features may be due to the interaction of the side vortices of the two jets.

These preliminary measurements of the spectra tend to indicate some spatial variation of the streamwise energy spectra. The spectra are also dependent on the jet configuration. The frequency corresponding to the major energy peak appears to remain largely unaffected by the location in the

jet and/or the jet configuration. A detailed , thorough study of the three-dimensional spectra would be needed in order to understand the turbuents energy distributions in the jets.

Chapter VI

ANALYSIS

The double jet behaviour is analyzed in this chapter for tandem as well as side-by-side jets using the integral approach of Ref.4. It was assumed in Ref.4 that the drag coefficient of the jets are the same as that of circular solid cylinders. It is reported in Ref.4 that the analysis for the single jet case using this assumption has given good agreement with data.

6.1 GOVERNING EQUATIONS

The governing equations from Ref.4 for a jet with average exit conditions are given below. Fig.84 shows the natural coordinate system in which the equations are written.

Mass continuity:

$$E = \frac{d}{ds} (\rho A v) \quad (12)$$

Where E is the mass entrainment, s is the coordinate along the trajectory, ρ is the density, A is the jet cross-sectional area, and v is the cross-sectional mean jet velocity.

Entrainment function:

$$E = (A/C) \rho_{\infty} E^* (v - U_{\infty}) \quad (13)$$

In this expression C is the jet circumference, E* is the entrainment coefficient.

In the analysis of turbulent flows using integral methods, the entire effect of turbulence is accounted for by the entrainment of fluid at the boundary. The determination of the entrainment coefficient is, therefore, crucial for obtaining meaningful results from the analysis. Morton (Ref.6) and Ricou and Spalding (Ref.20) have determined the entrainment coefficient for simple jets and wakes. Keffer and Baines (Ref.3) determined mass entrainment for a jet in cross-flow for different velocity ratios and plotted the entrainment coefficient, E* as a function of the distance along the jet trajectory (Fig.85); Campbell and Schetz (Ref.4) obtained an empirical expression for these curves for the entrainment coefficient and successfully used it in their analysis. Their expression for the entrainment coefficient is given by

$$E^* = 0.2 (s/D)^{1.37} / (v/U_{\infty})^{0.6} \quad (14)$$

Here D represents the jet exit diameter. This expression is used in the present analysis with some reservation because it is realized that it may not truly represent the entrainment mechanism in the case of multiple-jet cases; its use is nevertheless partially justified by the subsequent good agreement obtained between the theory and the available data.

s-Momentum:

$$\frac{d}{ds} (\rho A v^2) = -A \frac{d\bar{p}}{ds} - gA(\rho - \rho_\infty) \sin \alpha + EU_\infty \cos \alpha - \Gamma h \tau \quad (15)$$

where \bar{p} is the average jet static pressure, g is the gravity, α is the jet inclination with respect to the freestream velocity, τ is the longitudinal shear stress, and h is the lateral width of the jet.

This equation represents the balance of forces along the jet trajectory. The contributing terms are due to the rate of change of tangential momentum, the pressure gradient along the trajectory, the buoyancy, the mass entrainment and the shear stress. In order to evaluate the pressure gradient term, the assumption is made that the static pressure field around a solid cylinder imposes itself on the jet flow. This is a rather simplified model for the pressure field ar-

ising from the complicated process of turbulent jet injection into a cross-flow. However, the procedure has been found to be adequate for use in the present mathematical model. Differentiating the expression for freestream static pressure yields

$$\frac{d\bar{p}}{ds} = -q_{\infty} \sin\alpha \cos\alpha \frac{d\alpha}{ds} \quad (16)$$

The viscous shear stress in the s-direction is proportional to the velocity gradient in that direction and can be expressed by

$$\tau = \rho(\nu + \epsilon) \frac{dU}{dn} \quad (17)$$

where n represents the coordinate normal to the jet trajectory. The kinematic viscosity ν is neglected in the present study since, for turbulent mixing flows, it is small compared to the eddy viscosity ϵ . The eddy viscosity is estimated using Prandtl's hypothesis (Ref.21) for free turbulent flows. The eddy viscosity is represented by

$$\epsilon = \beta b (U_{\max} - U_{\min}) \quad (18)$$

where β is an empirical constant and b is the representative width of the jet. The maximum velocity in this expression is defined as the mean jet velocity in order to be compatible with the mean flow assumptions of the present study, and the minimum velocity is the freestream velocity compo-

ment in the s-direction. Thus the expression for the shear stress becomes

$$\tau = \rho \beta (v - U_{\infty} \cos \alpha)^2 \quad (19)$$

The buoyancy term is significant only in cases where the jets are non-isothermal and/or the jets and the freestream consist of gases of different densities. Substituting for the pressure gradient term, Eq.16, and the shear stress term, Eq.19, into Eq.15, the final s-momentum equation becomes

$$\begin{aligned} \frac{d}{ds} (\rho A v^2) = q_{\infty} A \sin \alpha \cos \alpha \frac{d\alpha}{ds} - gA (\rho - \rho_{\infty}) \sin \alpha + E U_{\infty} \cos \alpha \\ - \pi h \rho \beta (v - U_{\infty} \cos \alpha)^2 \end{aligned} \quad (20)$$

where C_D is the drag coefficient and q_{∞} is the freestream dynamic pressure. Similarly, the n-momentum equation may be written as

$$-\rho A v^2 \frac{d\alpha}{ds} = C_D q_{\infty} h \sin^2 \alpha + gA (\rho - \rho_{\infty}) \cos \alpha + E U_{\infty} \sin \alpha \quad (21)$$

The n-momentum equation represents the balance of forces acting perpendicular to the jet trajectory. The term on the left hand side represents the centrifugal force resulting from the curvature of the jet trajectory. This centrifugal

force is balanced by the components of the drag force, the buoyancy, and the mass entrainment. The drag term arises due to the blockage of the freestream; this is postulated to be the drag on an equivalent cylindrical shape inclined at an angle to the freestream flow.

Energy:

$$\frac{d}{ds} (\rho A V C_p T) = E C_p T_\infty + \bar{h} C (T_\infty - T) \quad (22)$$

In this expression C_p represents the specific heat, T the jet temperature, and \bar{h} the film heat transfer coefficient. The energy equation represents the energy balance of the jet fluid due to temperature increase, mass entrainment and convection at the jet boundary. This equation becomes trivial for isothermal jets.

When there are two or more jets, their influence on each other may be represented through changes in the effective drag coefficient, C_D , sensed by each jet. Hoerner (Ref.22) gives drag coefficients of two circular cylinders when they are placed one behind the other and also side-by-side for Reynolds number of 10^5 as shown in Figs. 86 and 87. This value of Reynolds number is reasonable in many jet problems. In Fig. 86 the drag coefficient, C_D , tends to an asymptotic

value of 1.18 for large separation distances. Note that the drag on the rear cylinder (and, hence rear jet) can actually be counter to the main flow.

Eq.12, 20, 21 and 22 form a set of coupled, nonlinear ordinary differential equations which may be solved by using standard routines available. Notice that for the tandem jet configuration, each jet has a set of four equations and the two sets must be solved simultaneously. The equations are presented here in the dimensional form; however, it was found more convenient to solve them in non-dimensional form. The freestream conditions and the jet exit diameter were used for nondimensionalizing the equations. Haming's Predictor-Corrector Method with a fourth order Runge-Kutta starter, as given in Ref.23, has been employed for the solution of these equations. The equations were solved in the order of continuity, n-momentum, s-momentum and energy. Since the mass-flow term $\rho A v$ appears in all the four equations, the continuity equation was solved first. The n-momentum equation was solved next to yield the jet inclination, α . The s-momentum yielded the term $\rho A v^2$; which in conjunction with the mass flow term was used to calculate the jet velocity, v . The energy equation was solved last completing one step in the solution procedure. The jet cross-sectional

area was calculated using continuity. The jet circumference was obtained from the assumed shape of the jet cross-section. The entrainment coefficient was then calculated using Eq.14. The perpendicular distance between the two jets was calculated at each step in the integration; it was then used to compute the drag coefficient, C_D from Figs.86 and 87 using a cubic spline interpolating routine. The most recent values of the dependent variables were used at each step in the integration. Double precision arithmetic was employed in all the calculations. It was determined by means of interval-halving method that the solution converged for a step-size of $s/D = 0.05$, the results agreeing up to the first four significant digits. A step-size of $s/D = 0.01$ was subsequently used in the present calculations. The computations were terminated when the jet cross-sections grew and coalesced into each other.

6.2 RESULTS

Figs. 88 to 91 show data of Ref.16 along with the present calculations for a 60 deg injection angle for tandem jets and a 90 deg injection angle for side-by-side jets. The single jet trajectory is also shown for reference. The sparseness of the data prevents any definitive conclusions from being drawn from the comparison of the data and the

present analysis. The agreement is good in the case of the rear jet trajectory. The most important result of the present analysis is that the rear jet trajectory is significantly modified by the presence of the front one even when the jets are spaced far apart, thus confirming the experimental observation presented earlier. As expected, the jet in front is influenced less by the presence of the rear one than vice versa. For the case in Fig. 90, the trajectory of the front jet is significantly affected, and the analysis correctly predicts the observed influence.

The data of Ref.16 indicate that , for the side-by-side case, the out of plane deflection of the jets is considerable for small separation distance($2.5D$); hence no attempt is made to compare the data and the present analysis for this separation distance. However, for a separation distance of $7.5D$, it is seen that the sideways deflection of jets is not significant. It is, therefore, concluded that the analysis is valid when the jets are not too close to each other.

Finally, Fig.92 shows the comparison of the trajectory results from the present analysis with the data. The present data also are included along with that of other investigators. The prediction is good for the nearfield; however, it overpredicts the trajectory for the downstream stations.

The main purpose of the analytical study has been to show the significant results which could be obtained by a simple extension of the earlier approach, and the attempt seems to have been fruitful.

Chapter VII

CONCLUSIONS AND SUGGESTIONS

In closing, several conclusions are drawn from the investigation of multiple jets presented in the previous chapters and a few suggestions are made for future work.

There is strong interaction between the jets for the jet spacing used in the present study. For the tandem jet configuration the rear jet trajectory is nearly straight, a consequence of the shielding effect of the leading jet. For the side-by-side jets, the flowfield in the region between the two jets undergoes intense mixing and the mean flow loses much of its momentum in this region.

After the two jets merge, the tandem jet trajectory is shifted upward in comparison to the single jet trajectory; this may be due to the large vertical momentum retained by the rear jet before the two jets merge.

The tandem jets show a larger spread in the vertical as well as the lateral direction when compared to single jet; the differences between the jet widths for the two cases are, however, small.

The width to height ratio of the jet cross-section is seen to be smaller than the generally accepted value of 5:1. The present study shows the ratio to be more near 2:1.

The mean velocity profile shows a defect rather than a velocity excess. This is in contrast to the similarity profiles of the previous investigators for higher velocity ratios.

Although the tandem jet mean flow and turbulence property distributions cover a wider region, in magnitude they are very nearly the same as the single jet.

The shape of the mean velocity, turbulence intensity, and shear stress profiles for the single jet, tandem jets, and the side-by-side jets (about the jet center) are strikingly similar for higher values of X/D ; therefore, it can be suggested that the counter-rotating vortices are the dominant agents in determining the structure of the downstream flowfield. This points to the fact that after the jets merge, the double jet flowfield behaves somewhat similar to the single jet flowfield.

The study shows that even in the complex flowfield of a double jet in a cross-flow there is good correlation between the mean velocity gradients and the shear stresses.

The flow visualization pictures show a circulating flow in the transverse plane for the single and the tandem jets; this confirms the observation of several of the previous investigators.

The spectral analysis shows no clear variations of the dominant frequencies with location in the jet and/or jet configuration. Further away from the plane of symmetry, a second hump is observed in the power spectral density distribution. This may be caused by the periodicity of the side vortices associated with the jets.

By way of suggestions for future experimental work, it is felt that more work in the area of flow visualization would yield very useful information. The hot-wire measurements in the nearfield was hampered by large values of turbulence intensities. Some other method of investigation (eg. laser-doppler velocimetry) may be of help in increasing the level of confidence of the nearfield data. Data at different velocity ratios and jet spacings are definitely needed to draw more general conclusions.

The analytical results supports the experimental finding regarding tandem jet trajectories, before the two merge. The side-by-side jet trajectory is not significantly altered from that of the single jet. A logical next step in the analytical study would be to extend the analysis to the region of the merged jets, the initial conditions for which may be obtained by taking the mean properties of the two jets.

It is pertinent to ask the question how the present study is applicable to a practical engineering problem such as environmental pollution. The turbulence data, as presented, may not be directly applicable to such an engineering situation; however, their usefulness may be realized when considering the diffusion of a scalar such as a pollutant gas, or in checking the validity of the turbulence models used in the solution of Navier Stokes equations. It may be more appropriate to view the present data as a part of an extensive and thorough study of multiple jets in a cross-flow.

An associated question is what parameters are to be matched in order to meaningfully compare single and double jets. In the present study which was primarily concerned with the interaction of two jets in the tandem and side-by-side configurations, the Reynolds number based on the free-stream velocity and the jet exit diameter, and the velocity ratio have been kept the same. For the problems dealing with comparison of single versus double (multiple) jets, matching the mass flow of single and double (multiple) jets may be equally important. Therefore, it is recommended for future work that the velocity ratio, the Reynolds number, and the mass flow be matched for the single jet and the double jets.

This study was conceived as a modest beginning towards understanding the complex nature of the flowfield arising

out of multiple jets in the presence of a cross-stream. It is hoped that the results and conclusions presented will uphold the purpose of the investigation.

REFERENCES

1. Abramovich, G.N., The Theory of Turbulent Jets. The MIT Press, Cambridge, Mass., 1963, pp. 541-553.
2. Schetz, J.A., Injection and Mixing in Turbulent Flow Progress in Astronautics and Aeronautics. Volume 68. 1980.
3. Keffer, J.F. and Baines, W.D., "The Round Turbulent Jet in a Cross-Wind," Journal of Fluid Mechanics. Vol. 15, Pt. 4, 1963, pp. 481-496.
4. Campbell, J.F. and Schetz, J.A., "Flow Properties of Submerged Heated Effluents in a Waterway," AIAA Journal, Vol. 11, Feb. 1973, pp. 223-230
5. Kamotani, Y. and Greber, I., "Experiments on a Turbulent Jet in a Cross-Flow," AIAA Journal, Vol. 10, Nov. 1972, pp. 1425-1429.
6. Morton, B.R., "On a Momentum-Mass Flux Diagram for Turbulent Jets, Plumes and Wakes," Journal of Fluid Mechanics, Vol. 10, Part 1, Feb. 1961, pp. 101-122.

7. Hoult, D.P., Fay, J.A. and Forney, L.J., "A Theory of Plume Rise Compared to Field Observations," Journal of Air Pollution Control Association, Vol. 19, No. 8, Aug. 1969, pp. 585-590.
8. Jordinson, R., "Flow in a Jet Directed Normal to a Wind," British Aeronautical Research Council, R&M 3074, Oct. 1956.
9. Ziegler, H and Wooler, P.T., "Analysis of Stratified and Closely Spaced Jets Exhausting into a Cross-Flow," NASA-CR-132297, 1973.
10. Makihata, T., and Miyai, Y., "Trajectories of Single and Double Jets Injected into a Crossflow of Arbitrary Velocity Distribution," Journal of Fluids Engineering, Vol. 101, Jun. 1979, pp. 217-223.
11. Chien, C.J. and Schetz, J.A., "Numerical Solution of the Three-Dimensional Navier-Stokes Equations with Application to Channel Flows and a Buoyant Jet in a Cross-Flow," Journal of Applied Mechanics, Vol. 42, September, 1975, pp. 575-579.
12. Patankar, S.V., Basu, D.K., and Alpay, S.A., "Prediction of the Three-Dimensional Velocity Field of a Deflect-

- ed Turbulent Jet," ASME Journal of Fluids Engineering, vol. 99, December, 1977, pp.758-762.
13. Jones, W.P., and McGuirk, J.J., "Computation of a Round Turbulent Jet Discharging into a Confined Cross-Flow," Turbulent Shear Flows 2, Springer Verlag, Heidelberg, 1980.
 14. Chassing, P., George, A., Claria, A., and Sannes, F., "Physical Characteristics of Subsonic Jets in a Cross-Stream," Journal of Fluid Mechanics, Vol. 62, part 1, 1974, pp.41-64.
 15. Crabb, D., Durao, D.F.G., and Whitelaw, J.H., "A Round Turbulent Jet Normal to a Cross-Flow," Paper presented at the ASME Winter Annual Meeting at Chicago, Illinois, Nov.16-21, 1980.
 16. Schwendemann, M.F., "A Wind Tunnel Investigation of Stratified Jets and Closely Spaced Jets Exhausting into a Cross-Flow," NOR 73-98, Northrop, Aircraft Division, Hawthorne, California, May, 1973.
 17. Hussain, A.K.M.F., and Ramjee, V., "Effects of the Axisymmetric Contraction Shape on Incompressible Turbulent Flow," ASME Journal of Fluids Engineering, Vol. 98, March, 1976.

18. Corrsin, S., and Uberoi, S., "Further Experiments on the Flow and Heat Transfer in a Heated Turbulent Air Jet," NACA TN 1865, 1949.
19. Champagne, F.H., and Sleicher, C.A., "Turbulence Measurements with Hot-Wires," part 2, Journal of Fluid Mechanics, Vol. 28, part 1, 1967, pp. 177-182.
20. Ricou, F.P., and Spalding, D.B., "Measurements of Entrainment by Axisymmetric Turbulent Jets," Journal of Fluid Mechanics, Vol. 11, 1961.
21. Schlichting, H., Boundary-Layer Theory, 6th Edition, McGraw-Hill Book Company, New York, 1968.
22. Hoerner, S.F., Fluid Dynamic Drag, Hoerner Fluid Dynamics, Brick Town, New Jersey, 1965, pp. 8-1, 8-3.
23. Carnahan, B.L. Luther, H.A., and Wilkes, J.O., Applied Numerical Methods, John Wiley and Sons, Inc., New York, 1969, pp. 381-406.
24. Ramsey, J.W., "The Interaction of a Heated Air Jet with a Deflecting Flow," Ph.D. Thesis, University of Minnesota, June 1969.

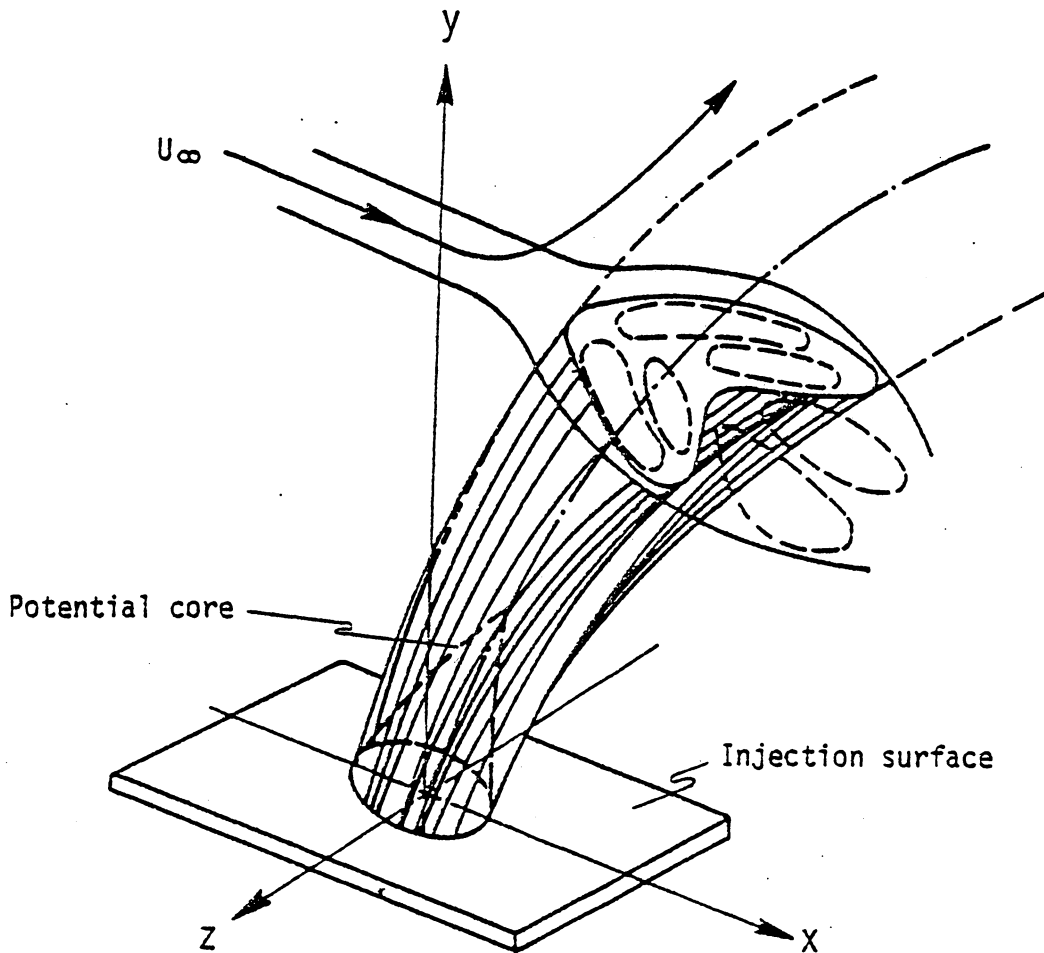


Figure 1 - Diagram of the interaction resulting from jet injection into a cross flow (after Abramovich (Ref.1))

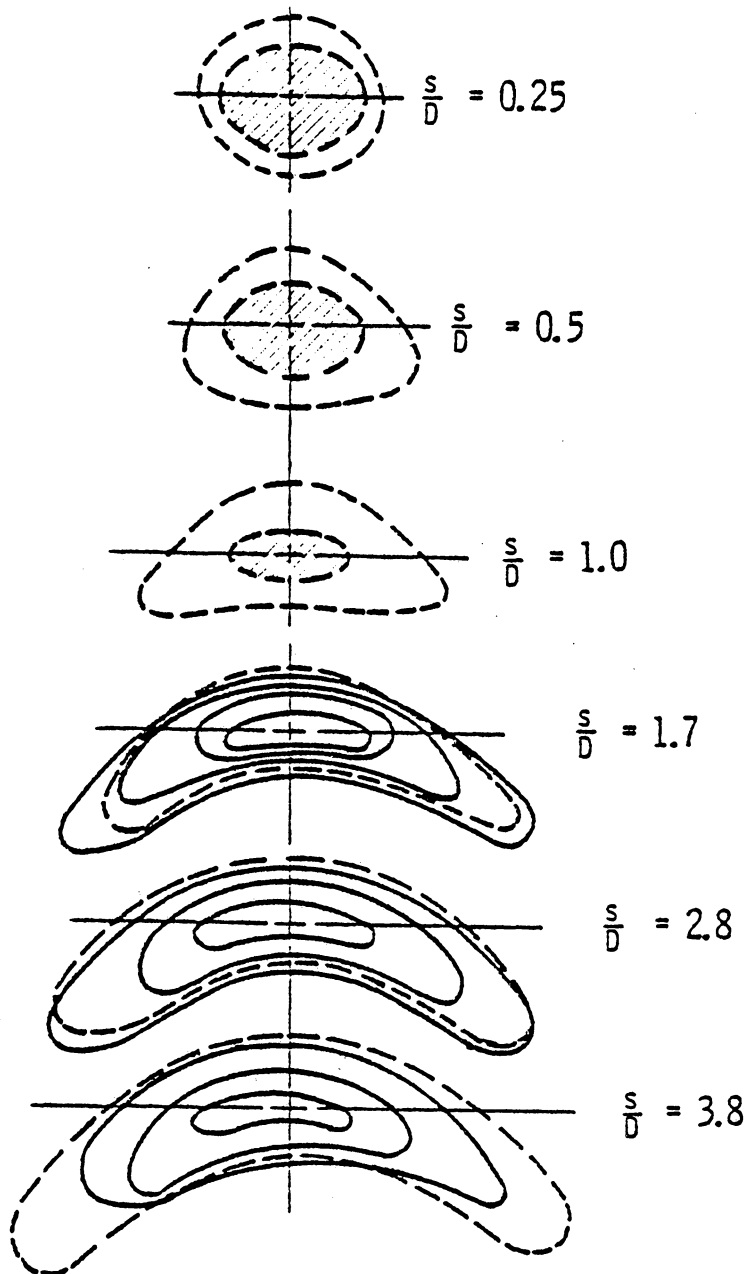


Figure 2 .- Cross-sectional pressure contours of a jet injected normally into a cross flow, $V_j/U_\infty = 2.2$ (after Abramovich (Ref.1) solid and dashed lines represent lines of constant total and static pressure, respectively, and the shaded areas indicate the potential core region.

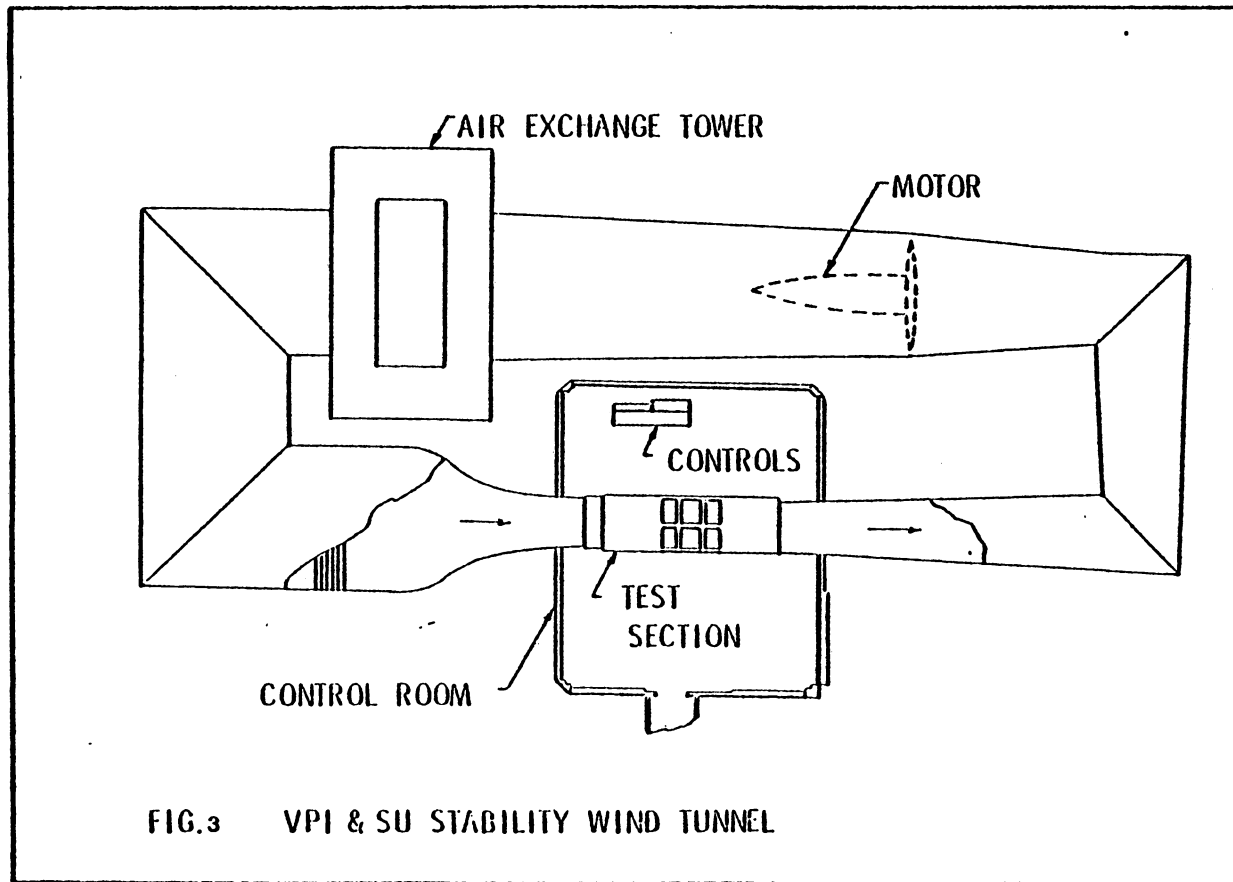


FIG.3 VPI & SU STABILITY WIND TUNNEL

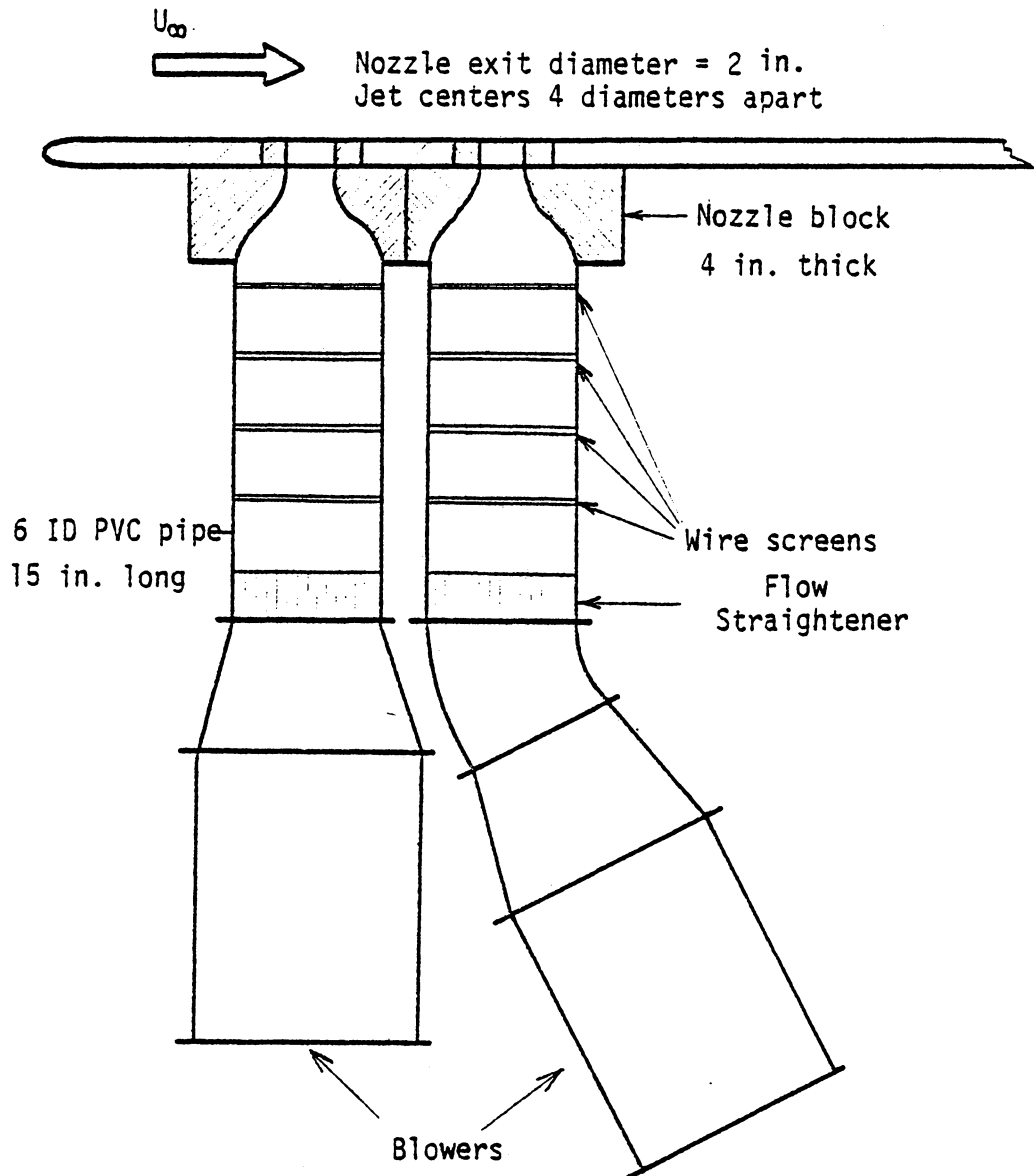


Fig.4 - Schematic diagram of the jets

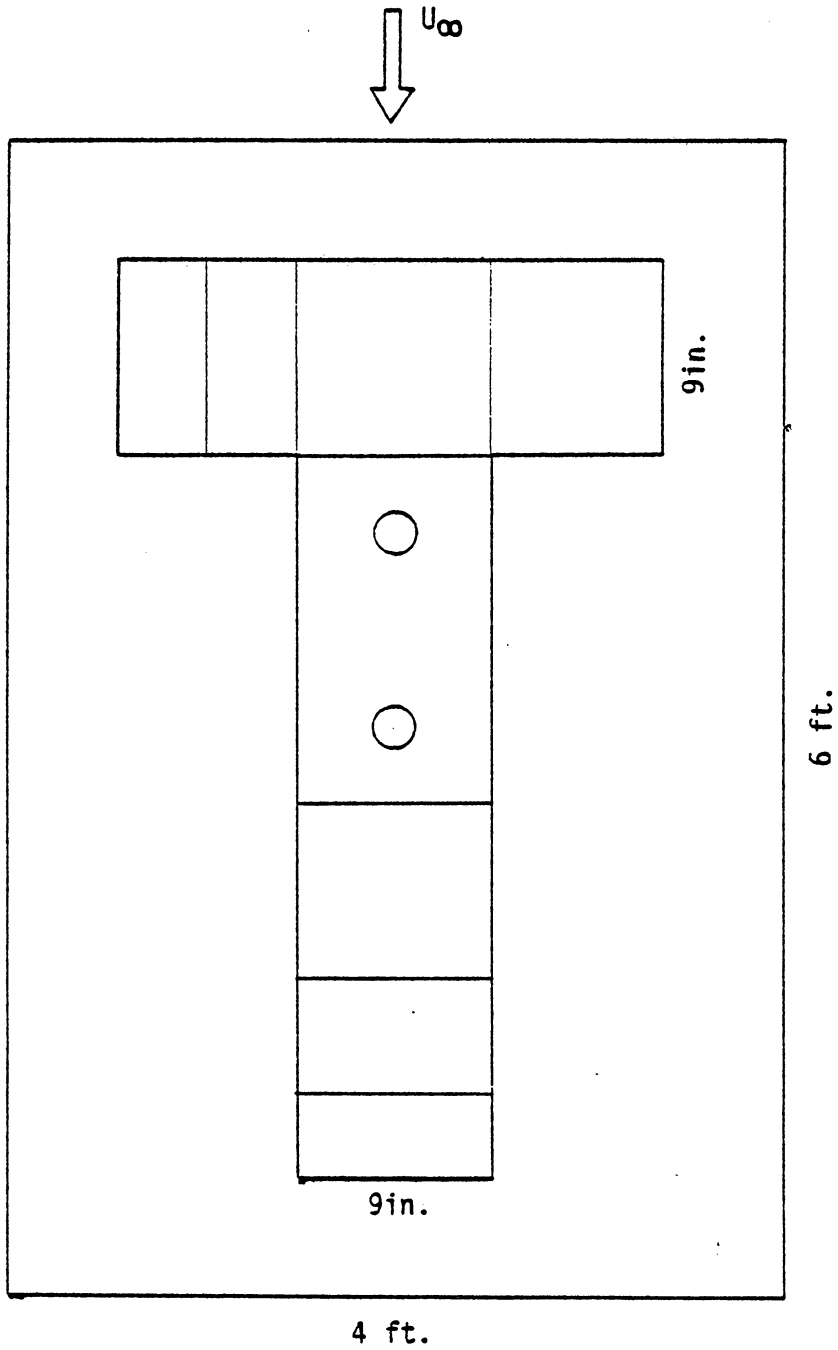


Fig.5 - Injection plate and Spacing blocks

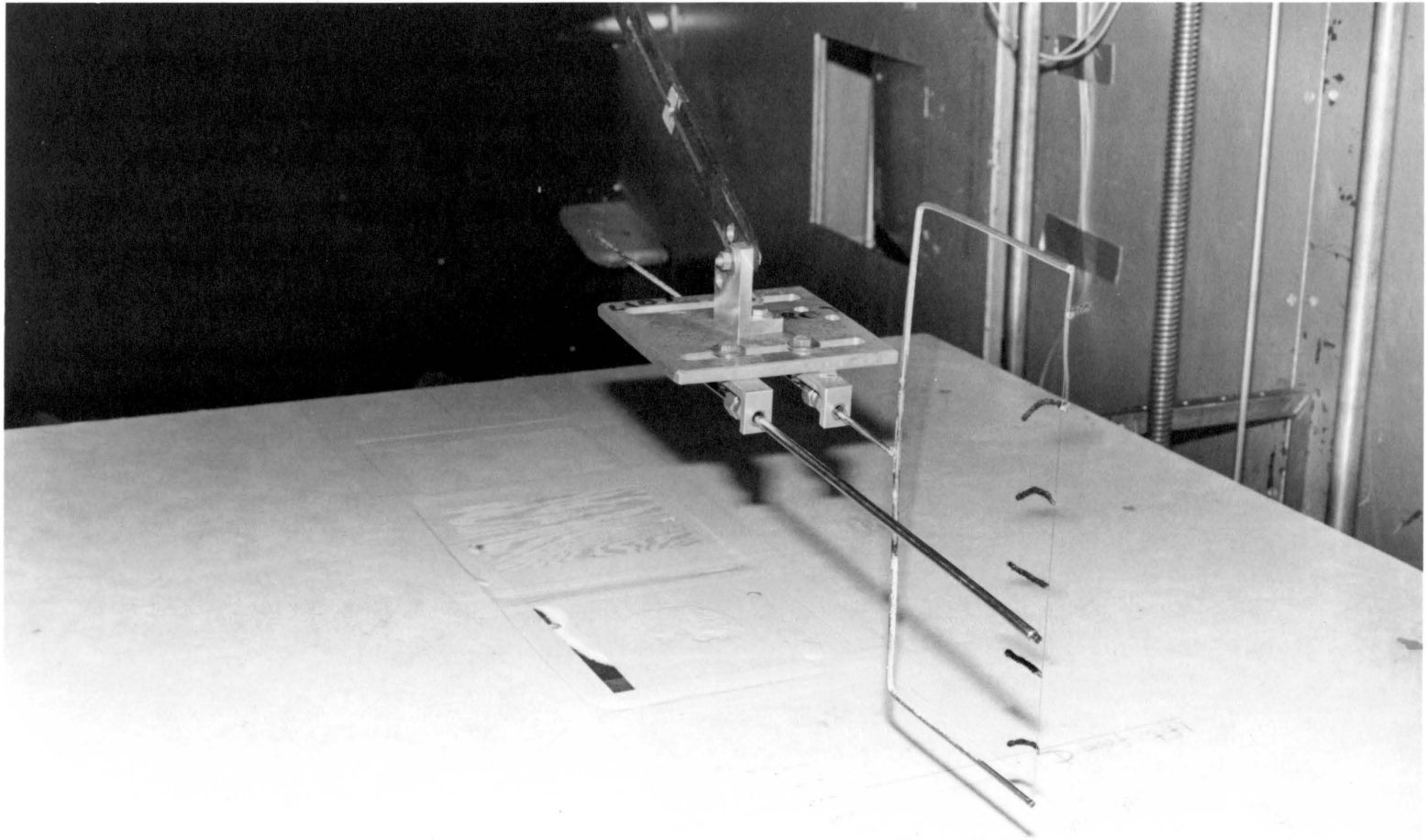


Fig.6 Hot Wire Rake and Tuft Wire

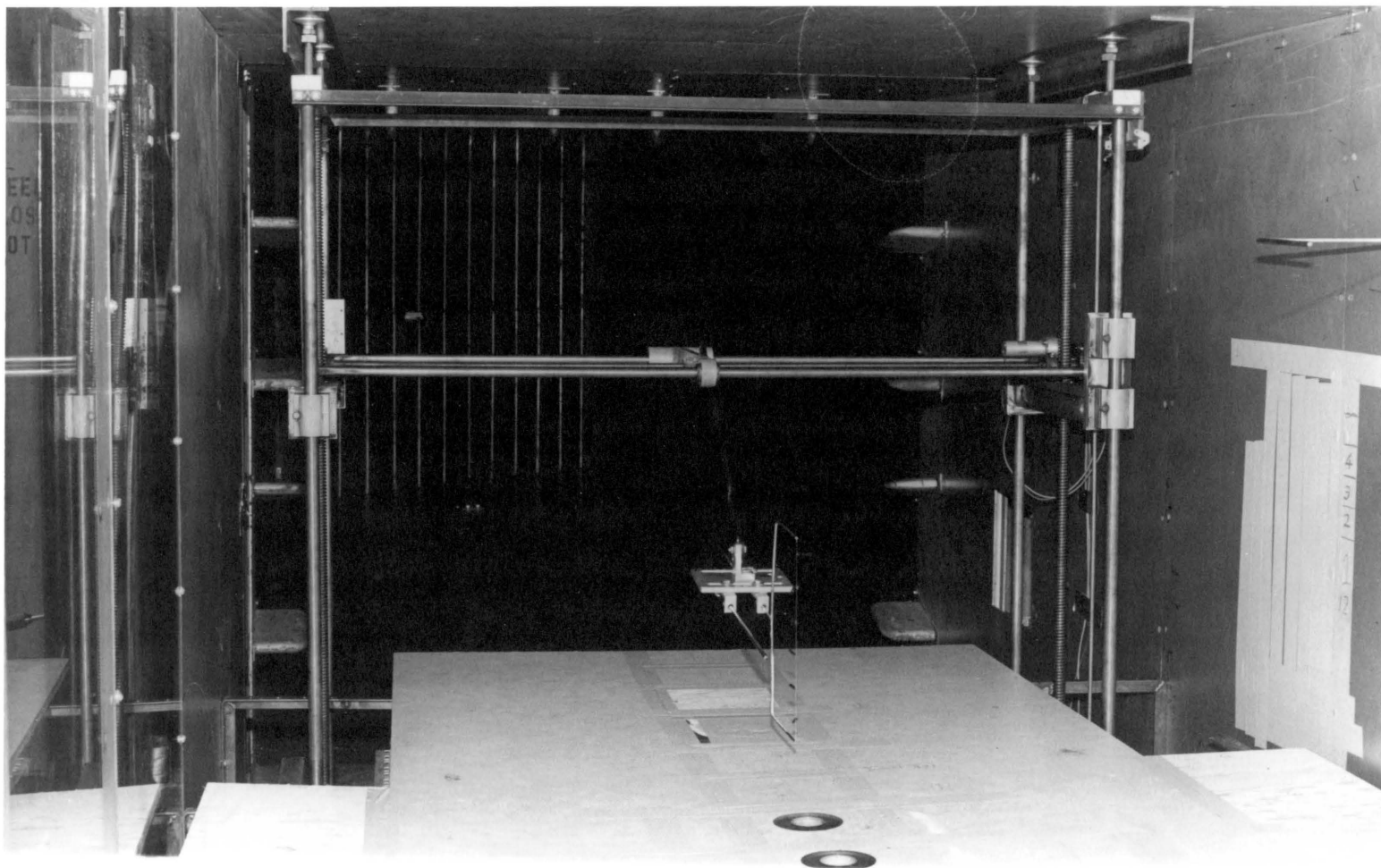
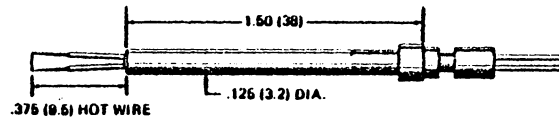


Fig.7 Automatic Transverse System

Model 1210 Standard Straight Probe

This Probe Is Used For Most Single Sensor Measurements – Either Parallel Or Perpendicular To Flow Direction



MODEL 1241 END FLOW "X" PROBE

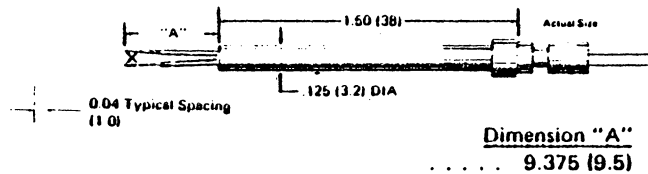


Fig. 8 - Types of probes used in the investigation

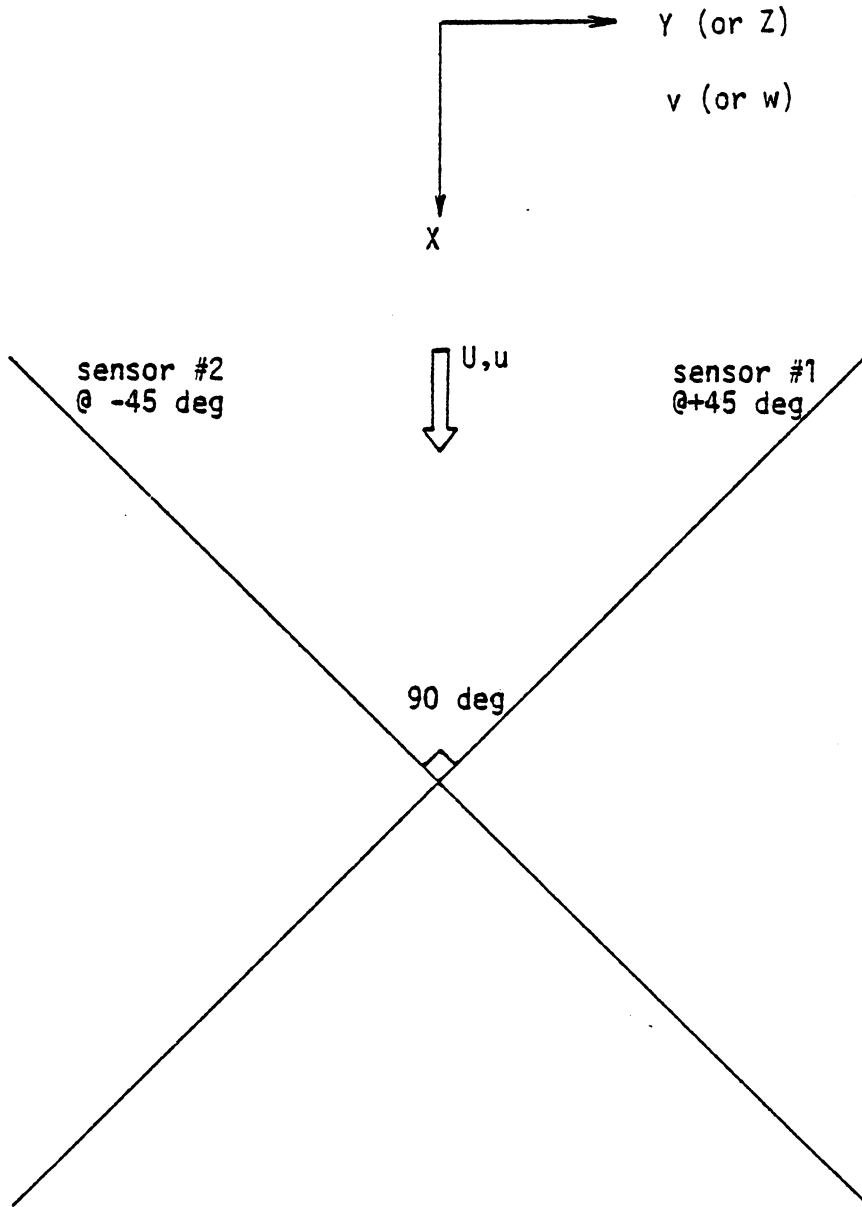


Fig.9 - Schematic diagram of an X-wire probe in relation to the mean flow.

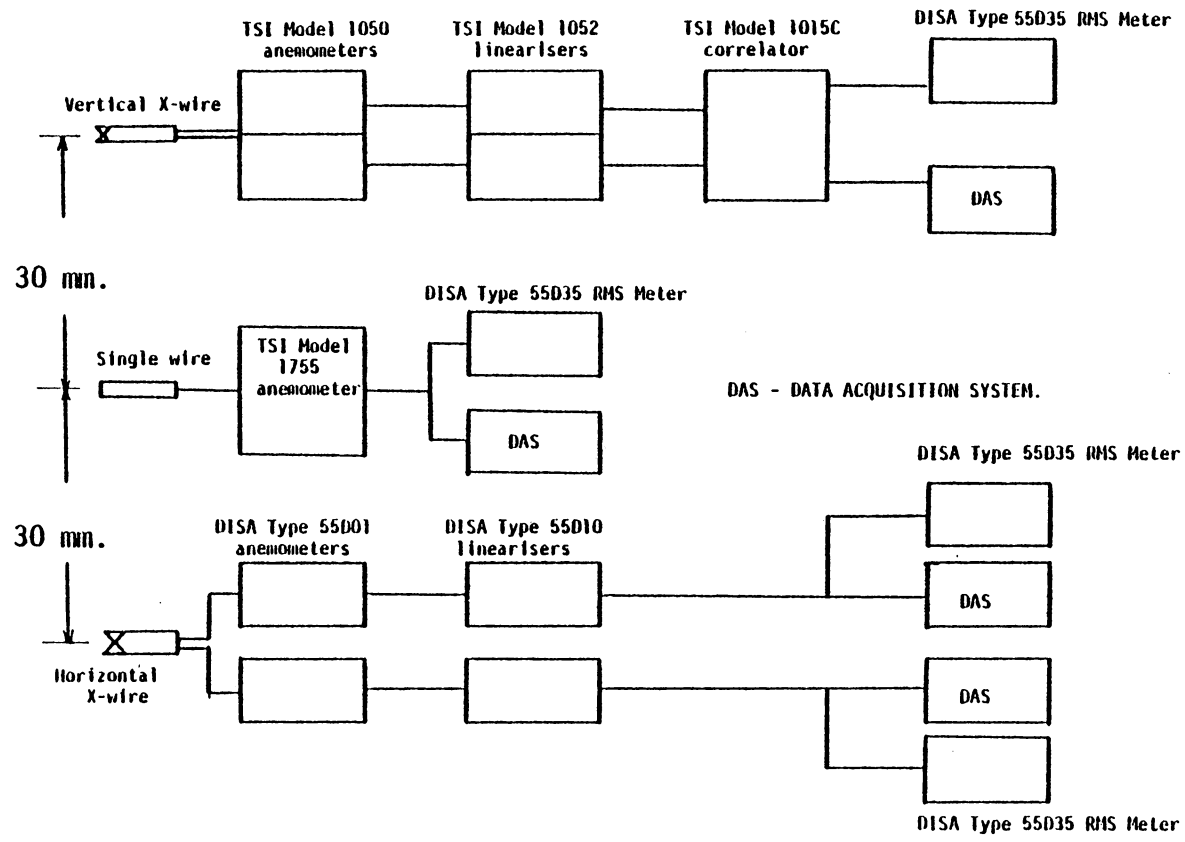


Fig.10 - Schematic diagram of the instrumentation for the first set of experiments

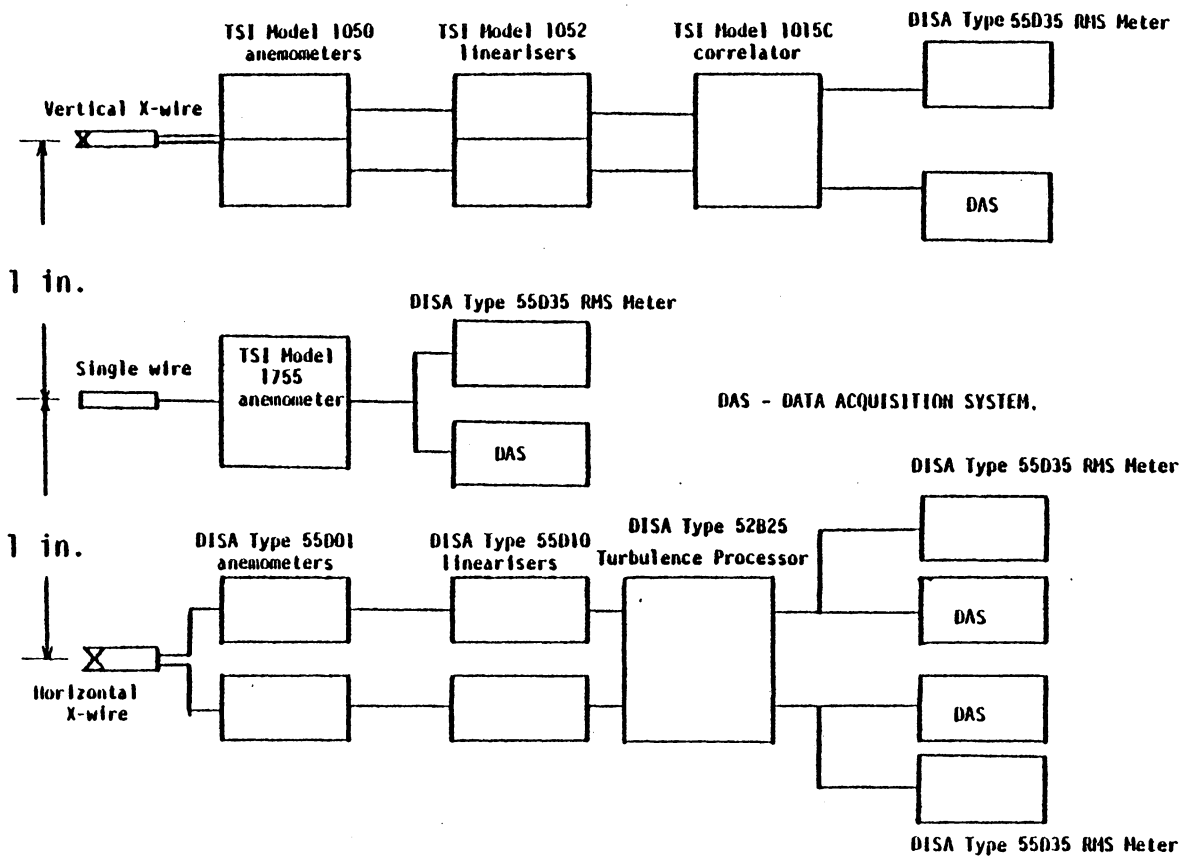


Fig.11 - Schematic diagram of the instrumentation for the second set of experiments.

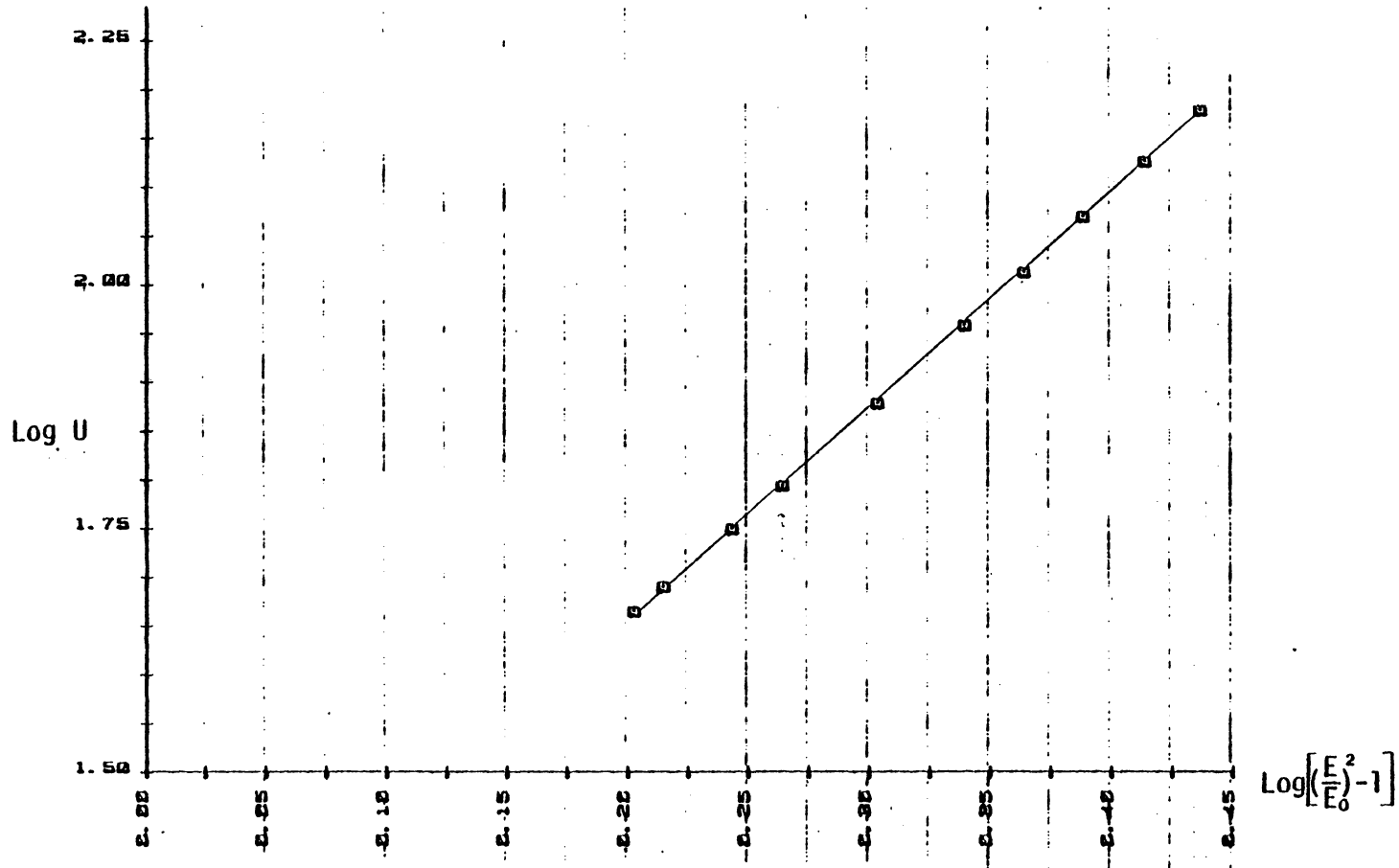


Fig.12 -Typical sensor calibration curve

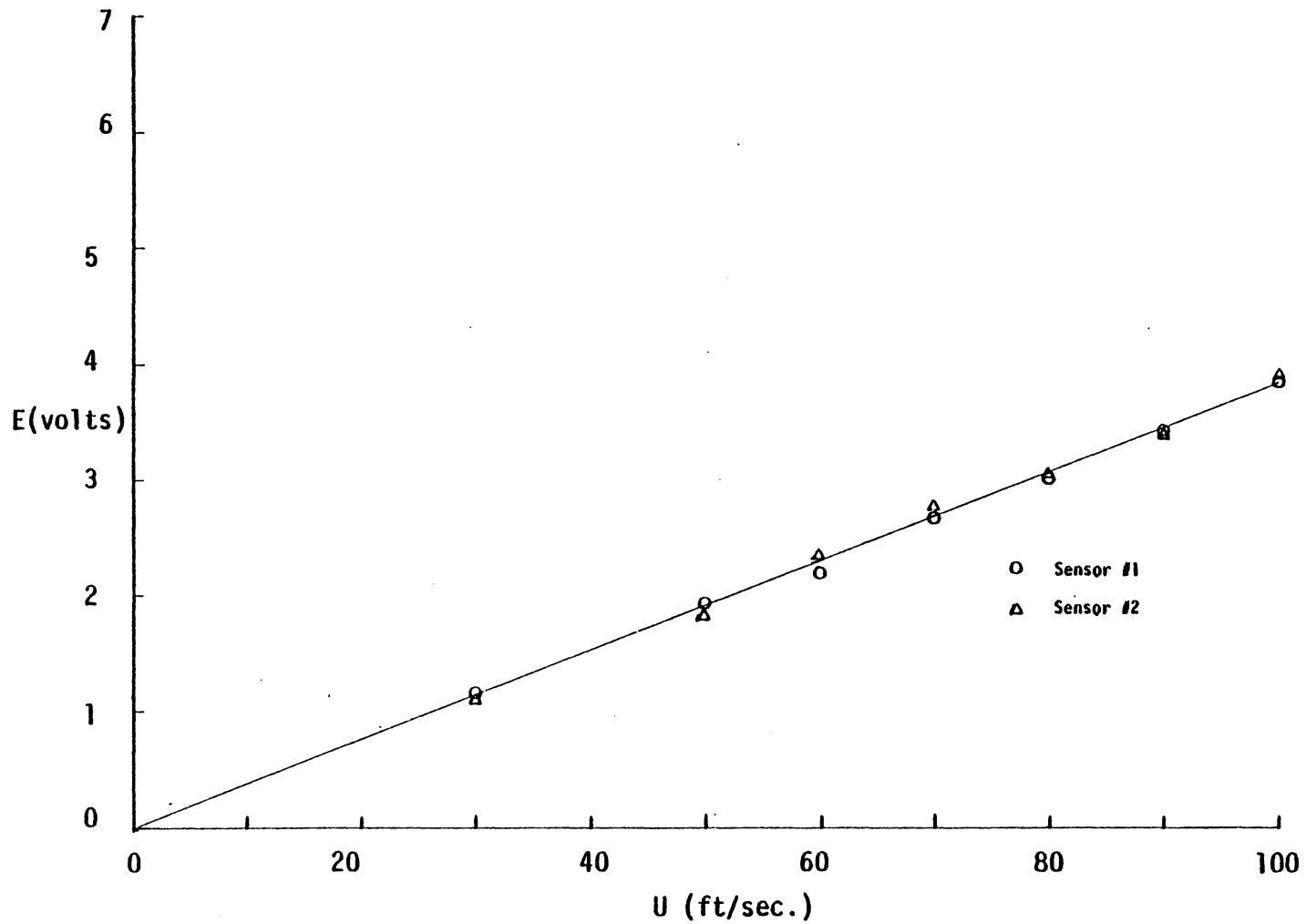


Fig.13 - Linearized output voltage of the hot-wire sensors oriented at 45 deg to freestream

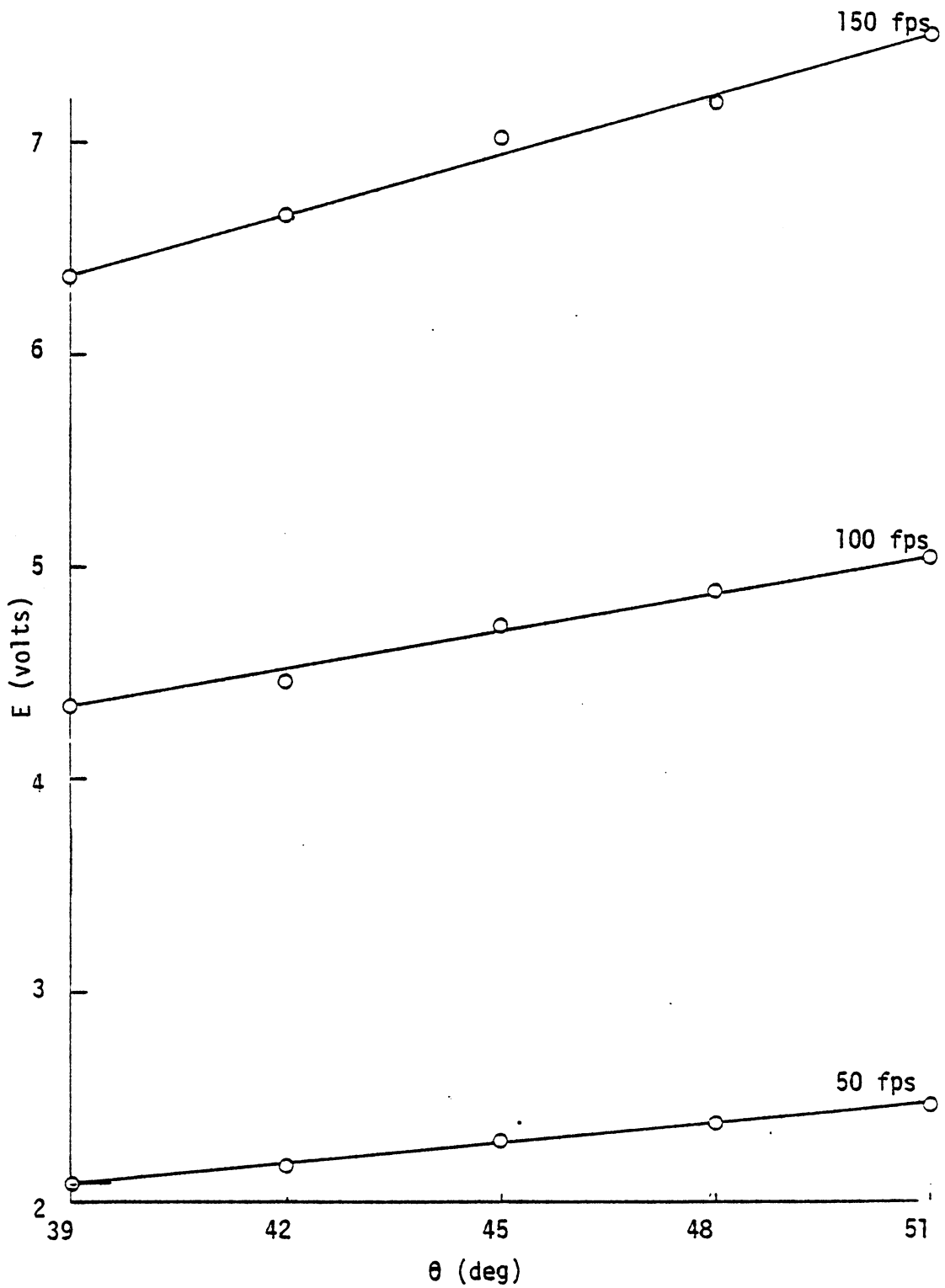


Fig.14 - Voltage output for different sensor orientations

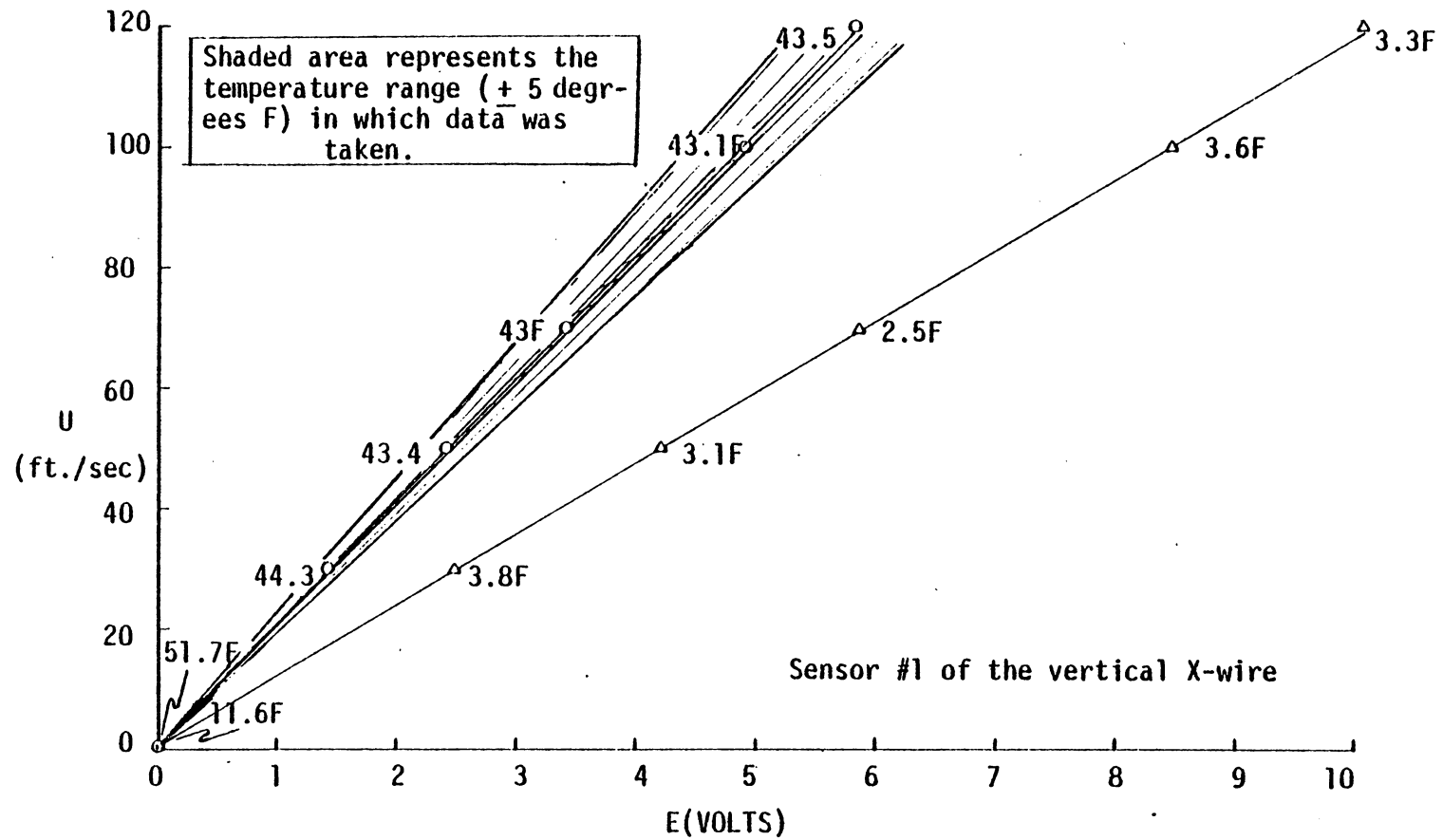


Fig.15 - Effect of temperature variation on the output voltage of the anemometer.

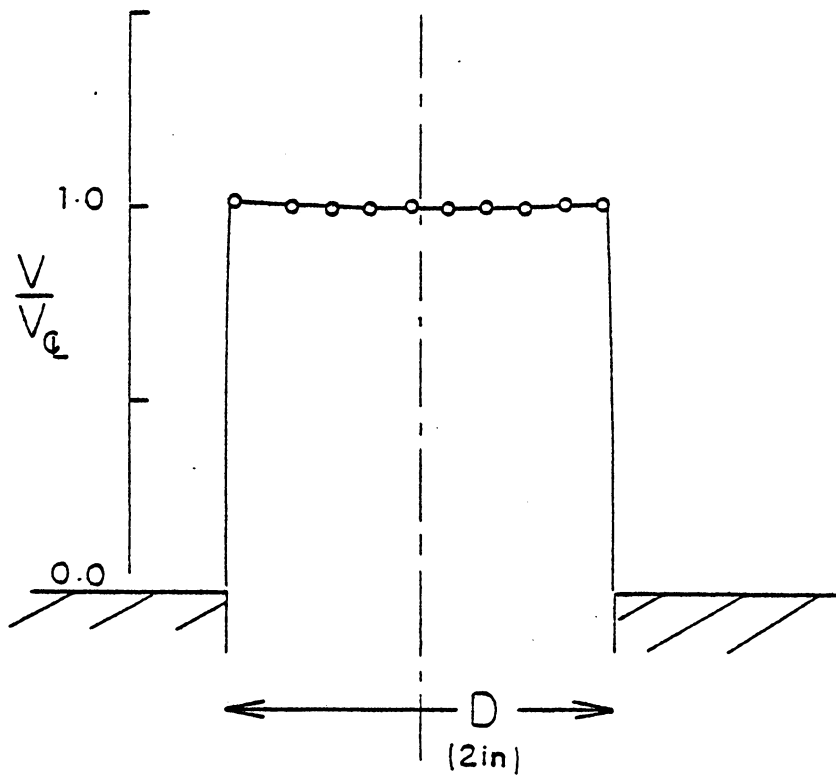


Fig.16 - Velocity profile at the jet exit

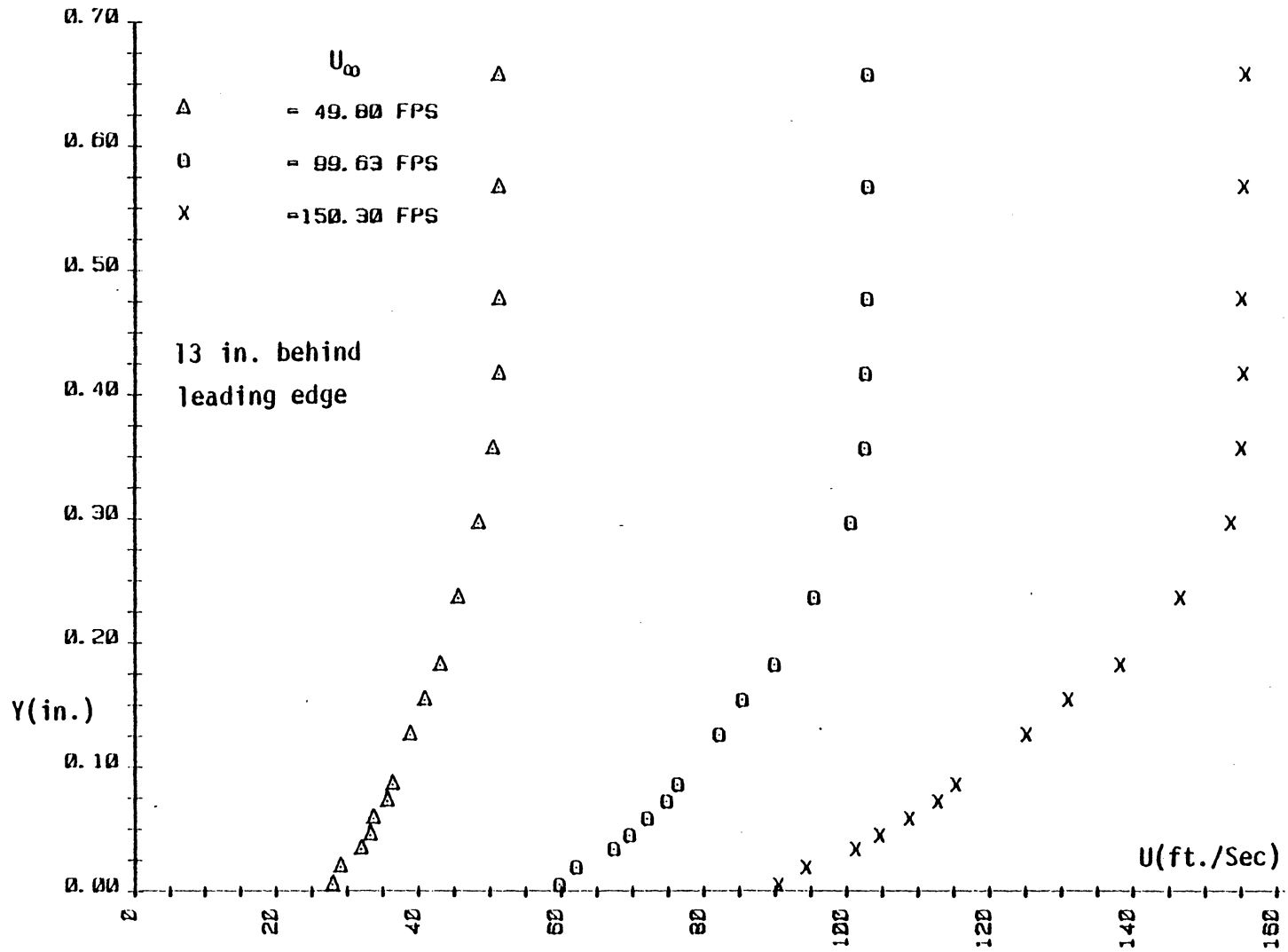


Fig.17 - Velocity profiles in the boundary layer of the injection plate with no injection; front edge of front jet

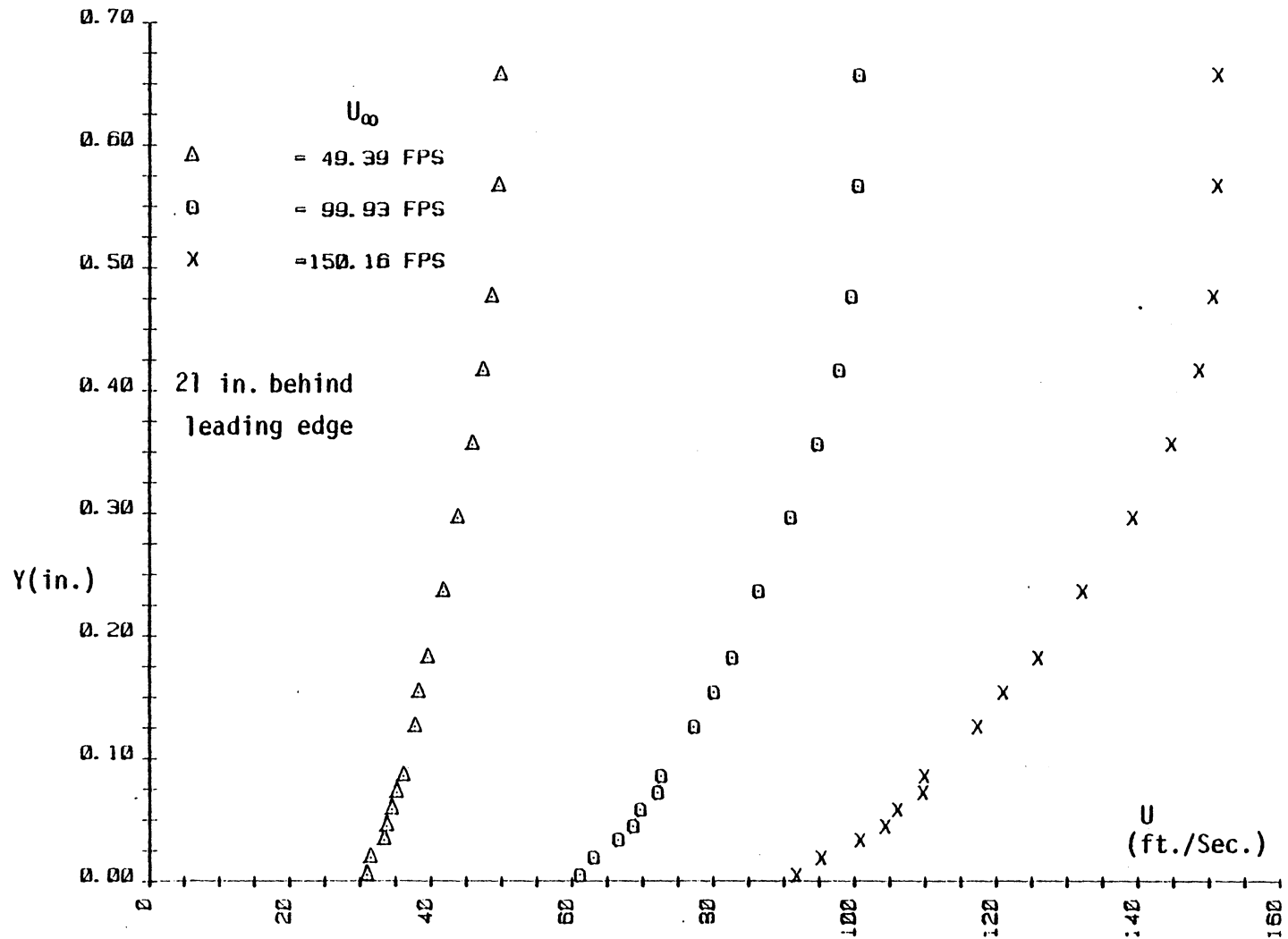


Fig.18 - Velocity profiles in the boundary-layer of the injection plate with no injection; edge of rear jet.

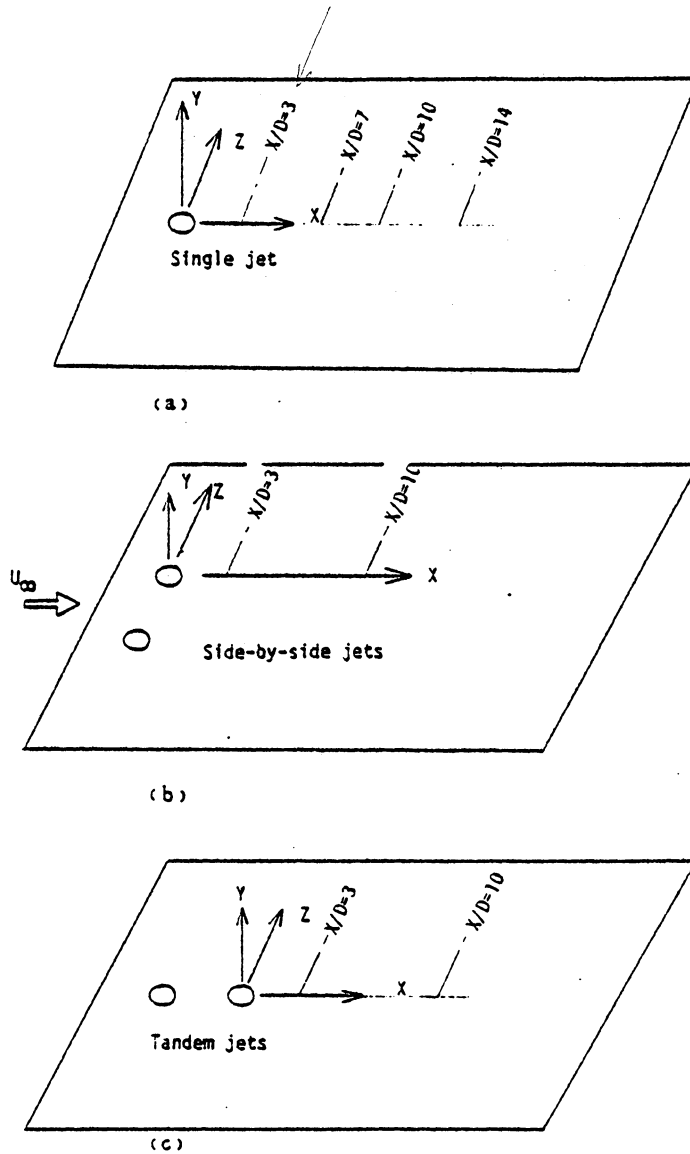


Fig. 19 Coordinate systems used for the three configurations

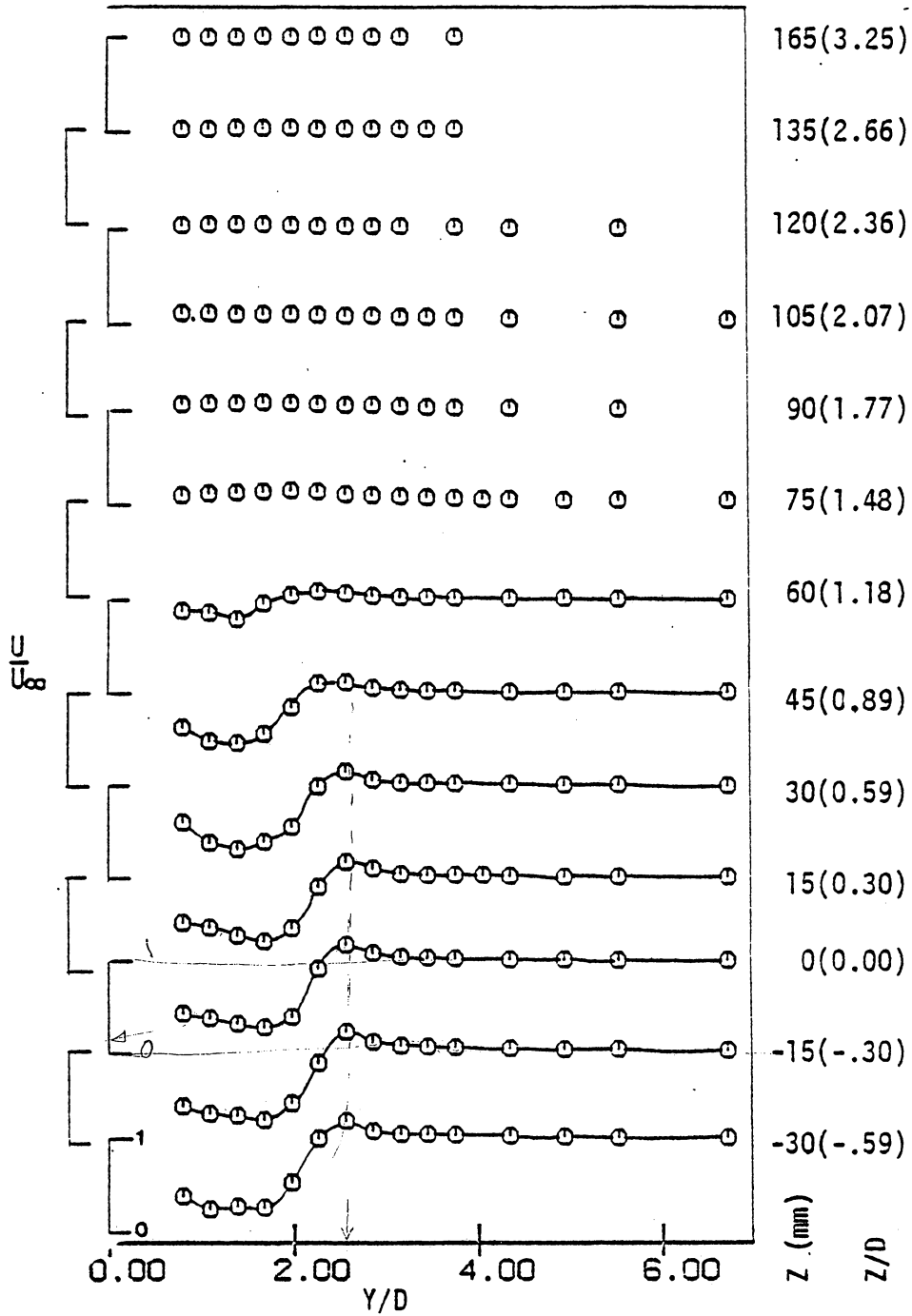


Fig.20 - Vertical distribution of axial mean velocity; single jet; $X/D = 3$.

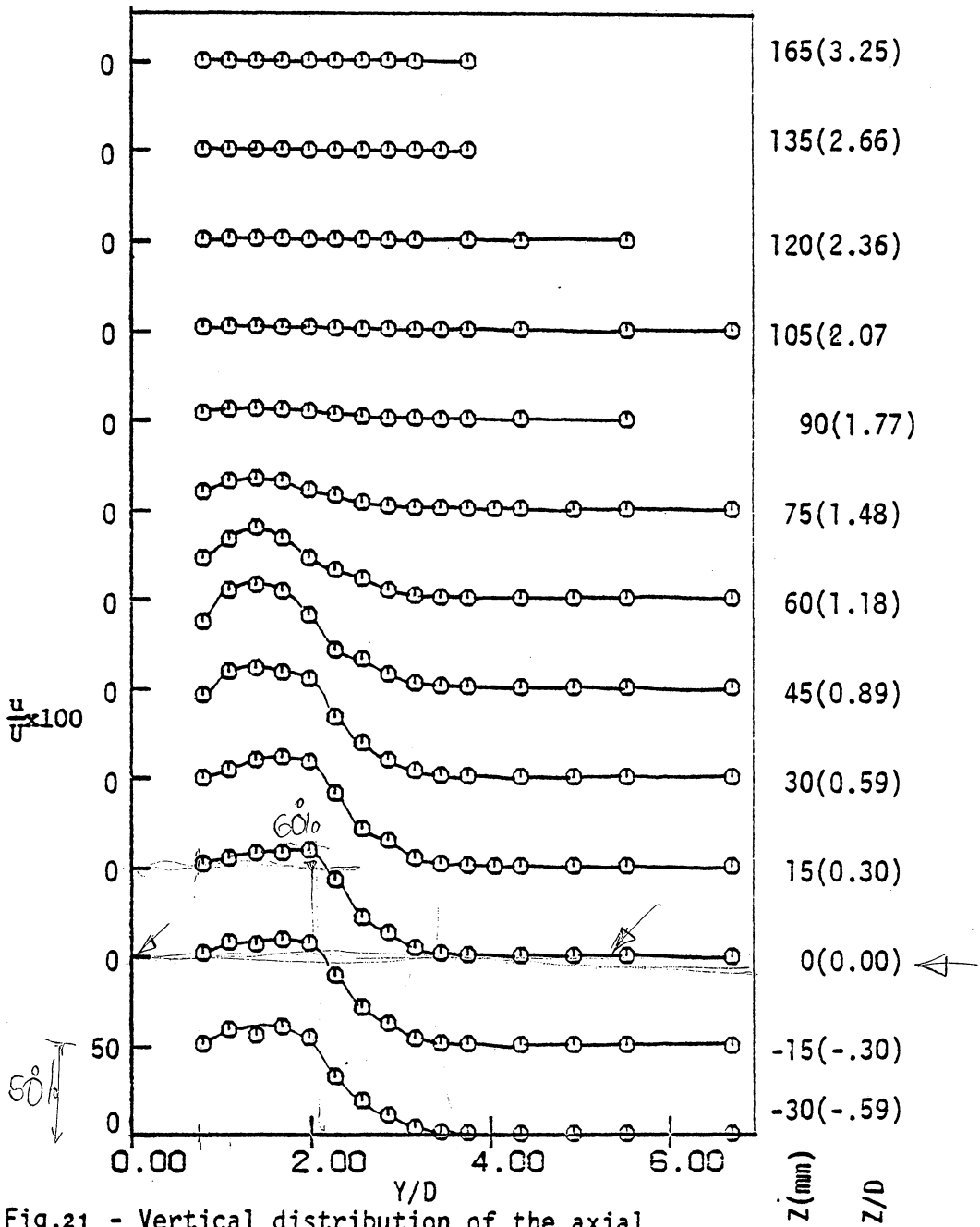


Fig.21 - Vertical distribution of the axial turbulence intensity; single jet; $X/D = 3$.

$VR = 2.0$

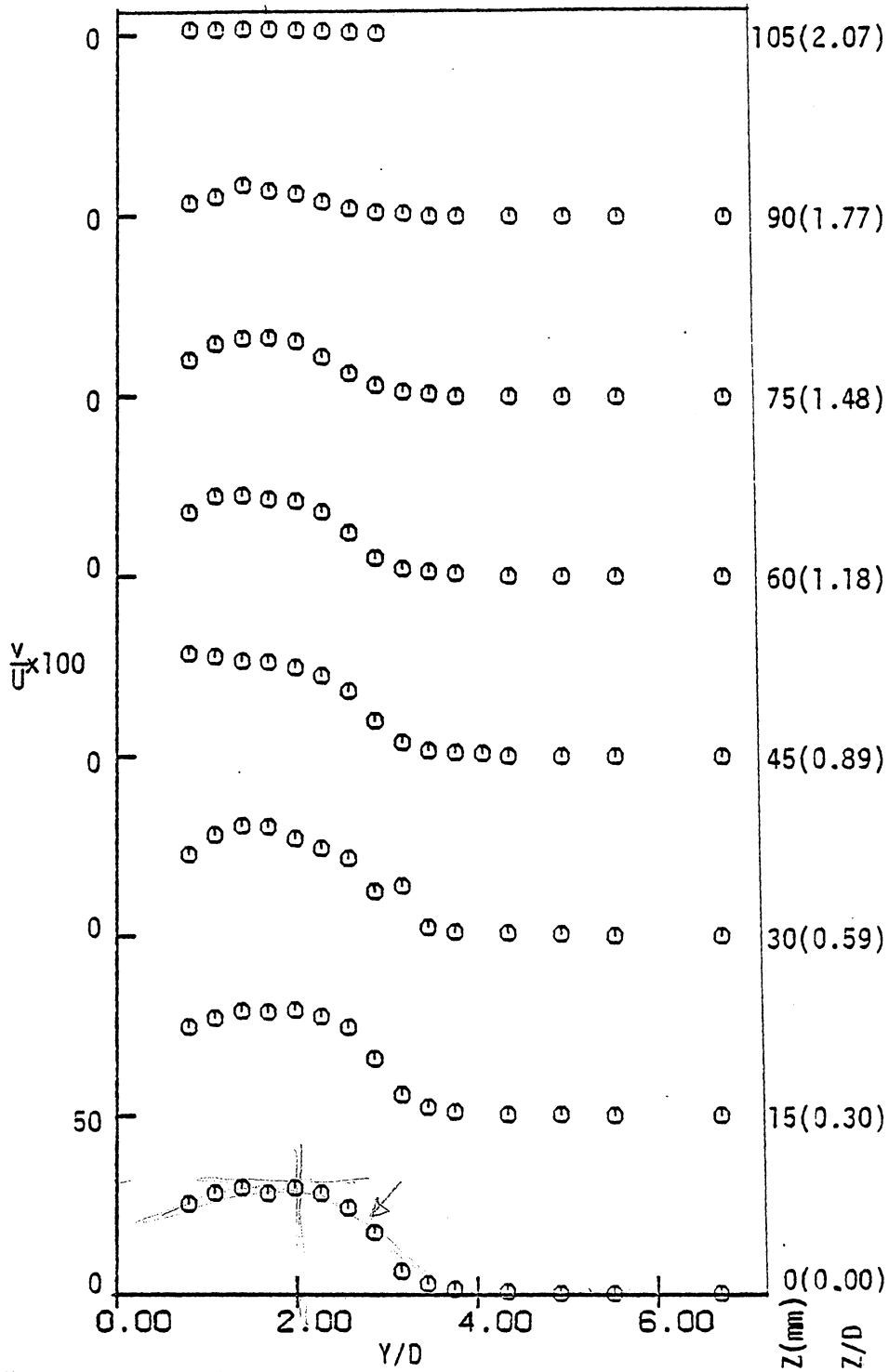


Fig.22 - Vertical distribution of the vertical turbulence intensity; single jet X/D = 3.

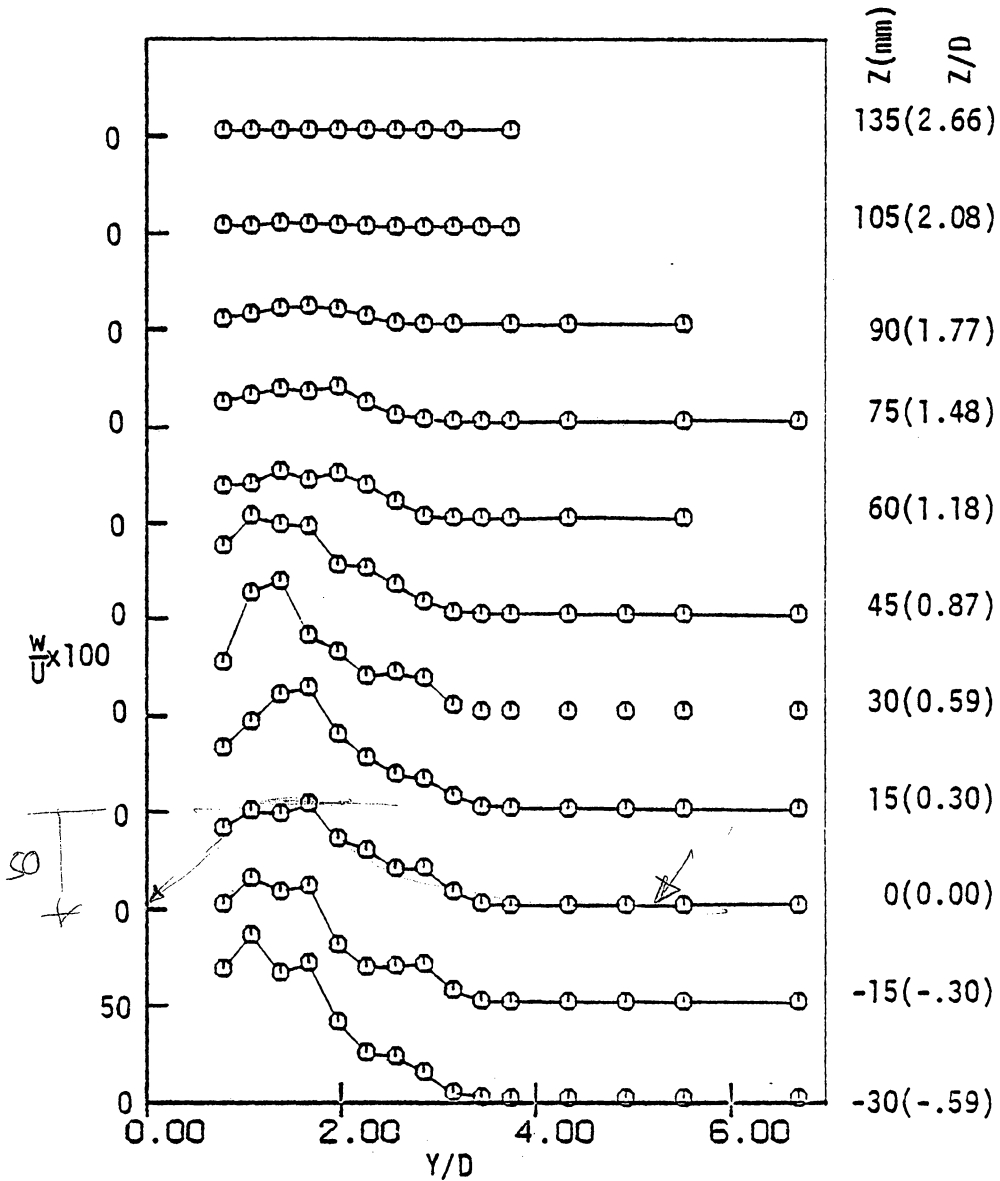


Fig.23 - Vertical distribution of the horizontal turbulence intensity; single jet; $X/D = 3$.

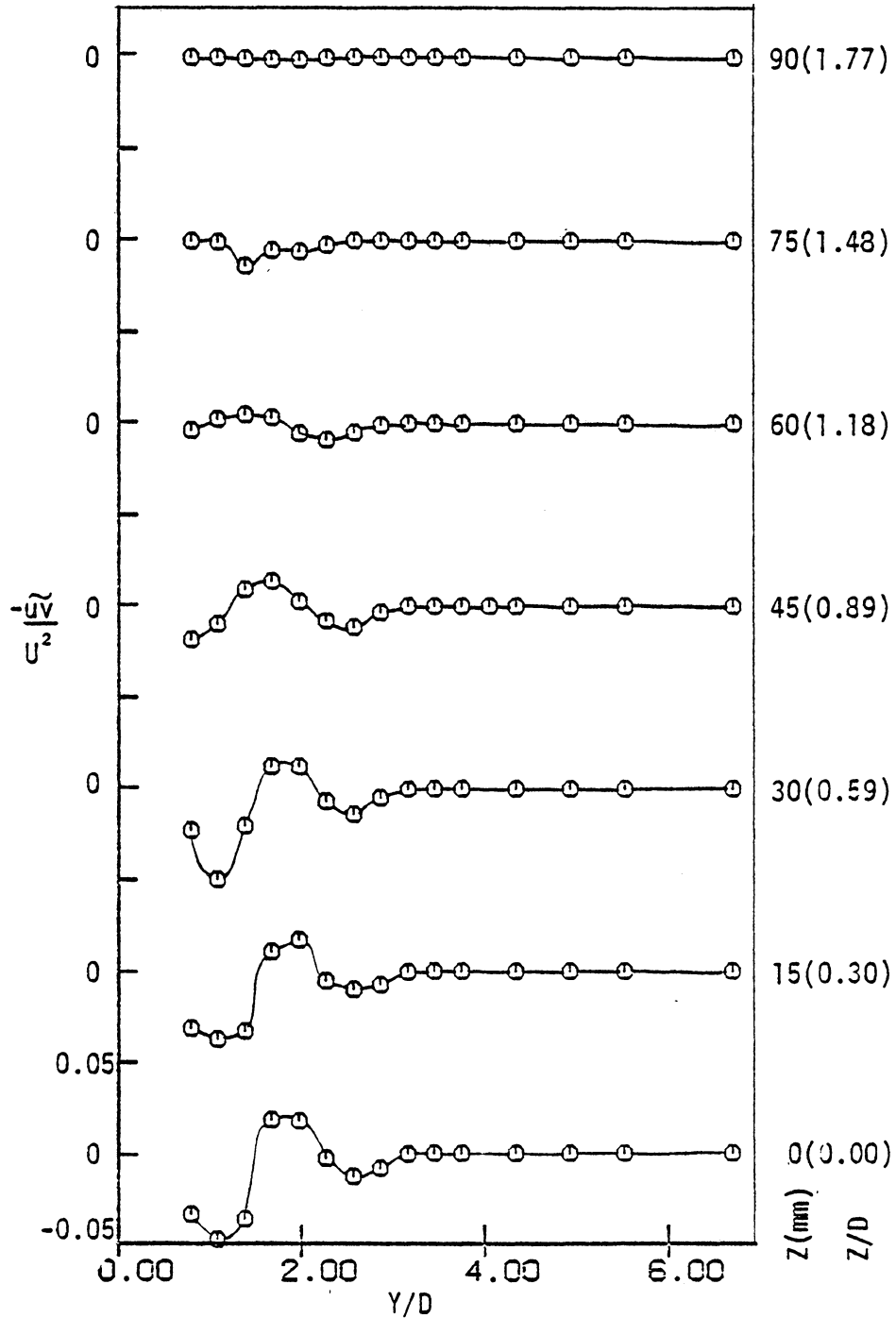


Fig.24 - Vertical distribution of the vertical shear stress; single jet; X/D = 3.

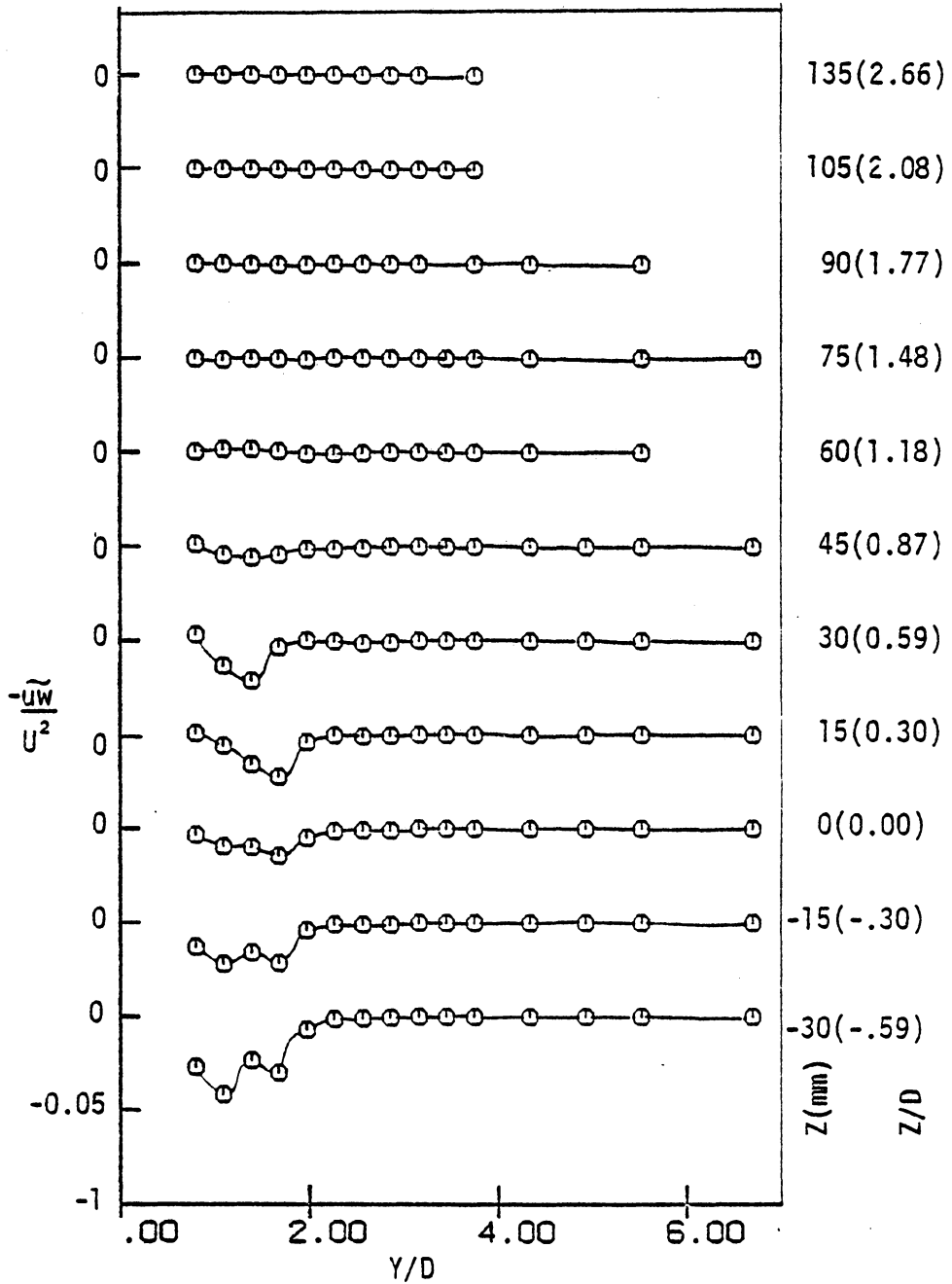


Fig.25- Vertical distribution of the horizontal shear stress; single jet; X/D = 3.

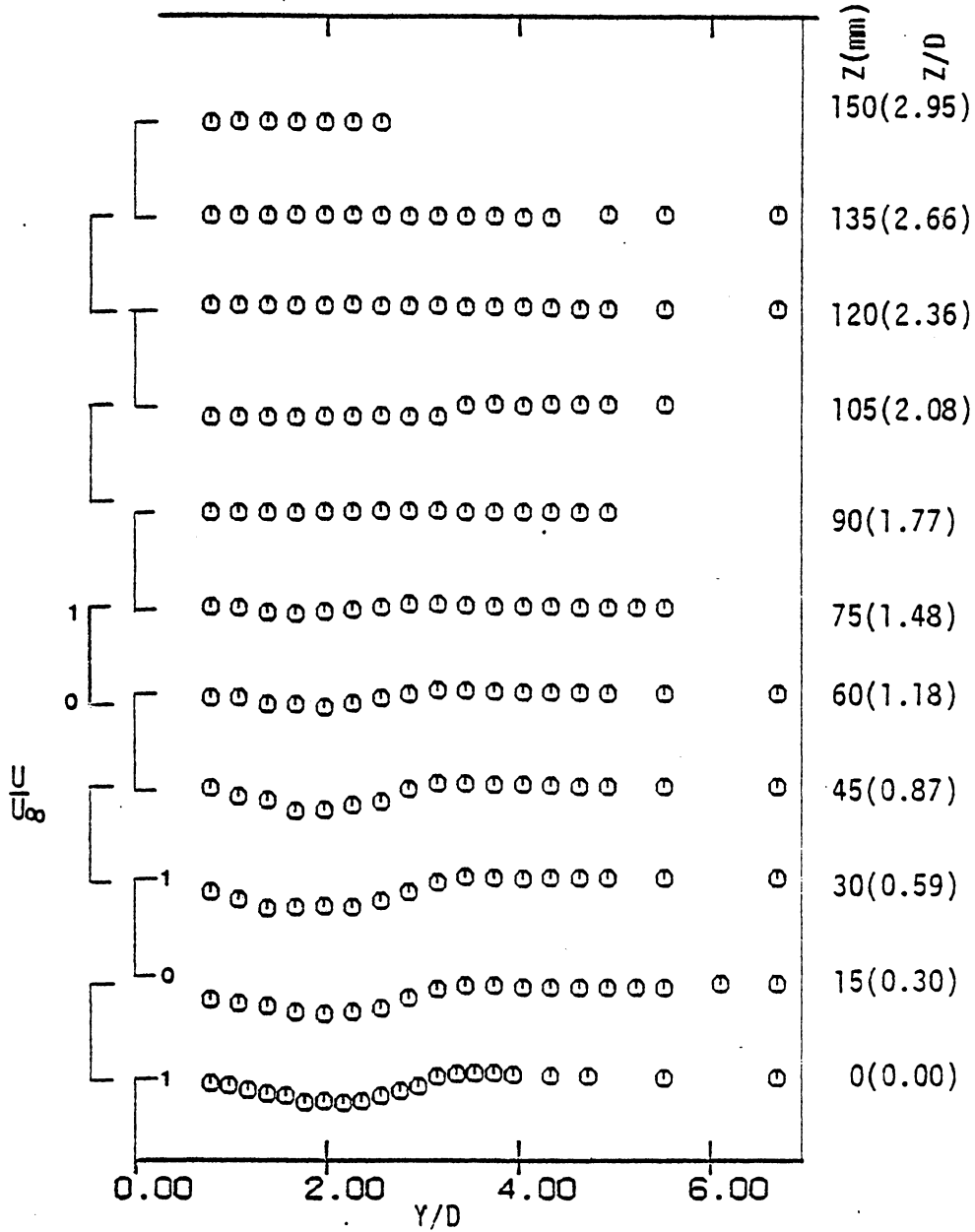


Fig.26 - Vertical distribution of the axial mean velocity; single jet; $X/D = 7$.

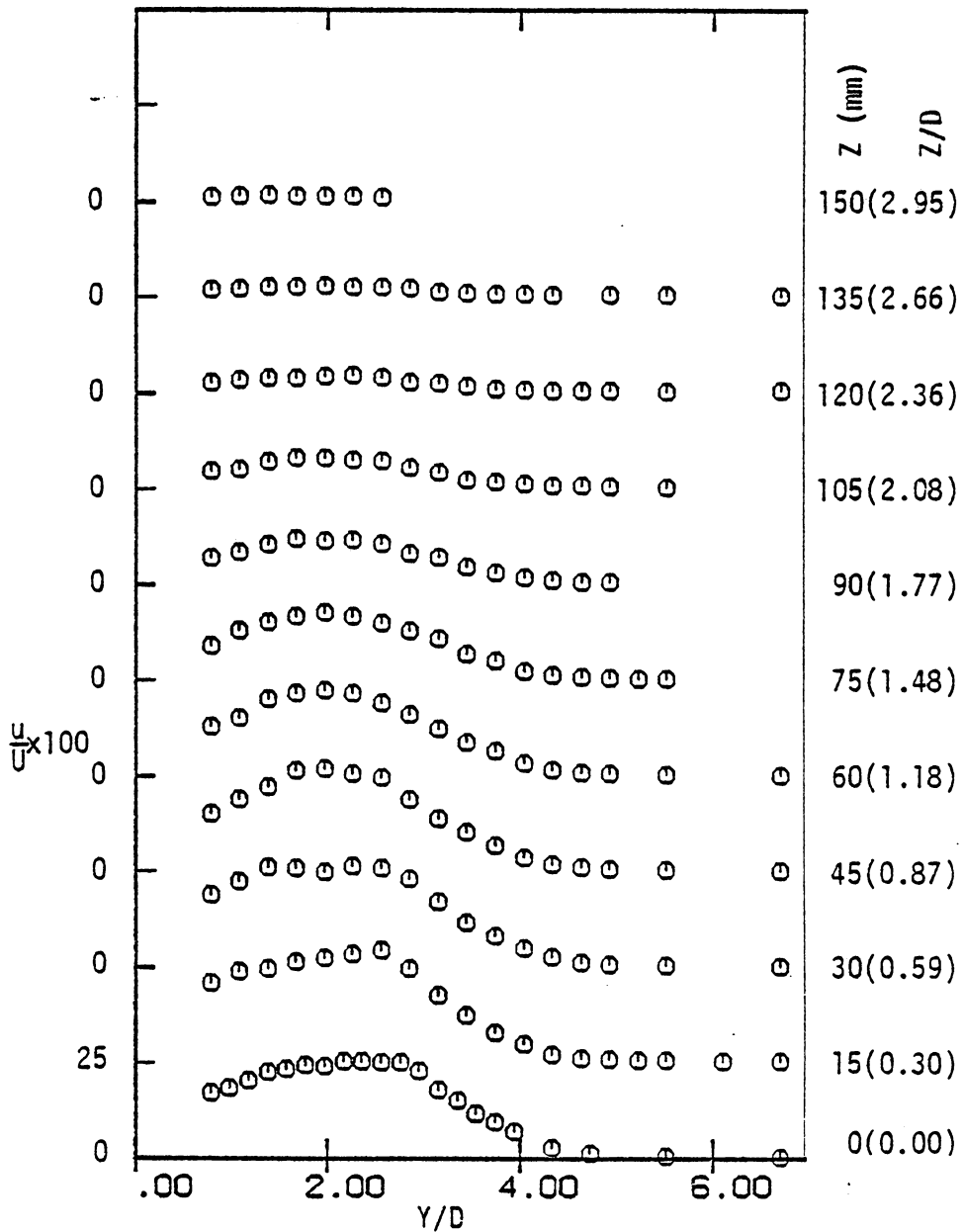


Fig.27 - Vertical distribution of the axial turbulence intensity; single jet; $X/D = 7$.

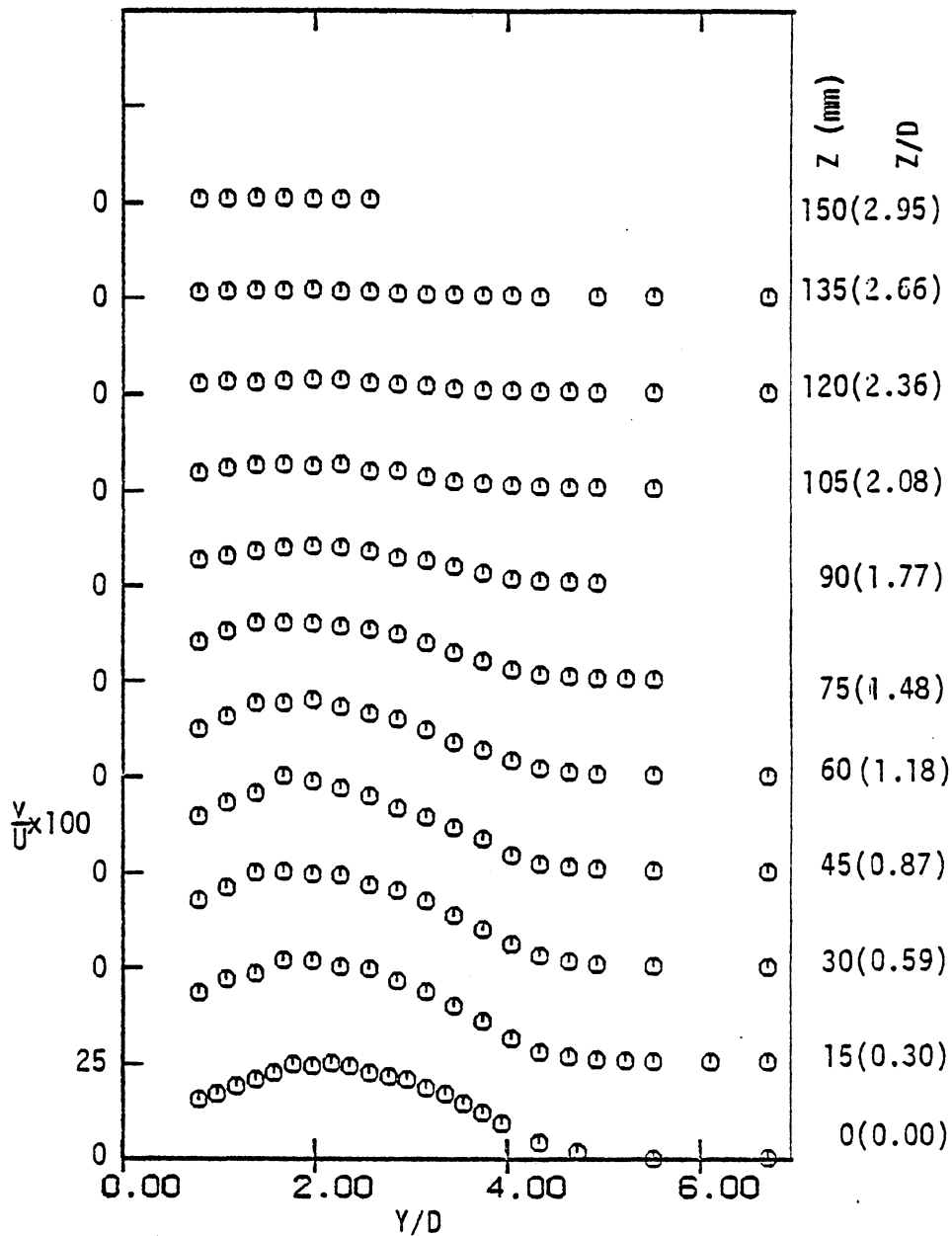


Fig.28 - Vertical distribution of the vertical turbulence intensity; single jet; $X/D = 7$

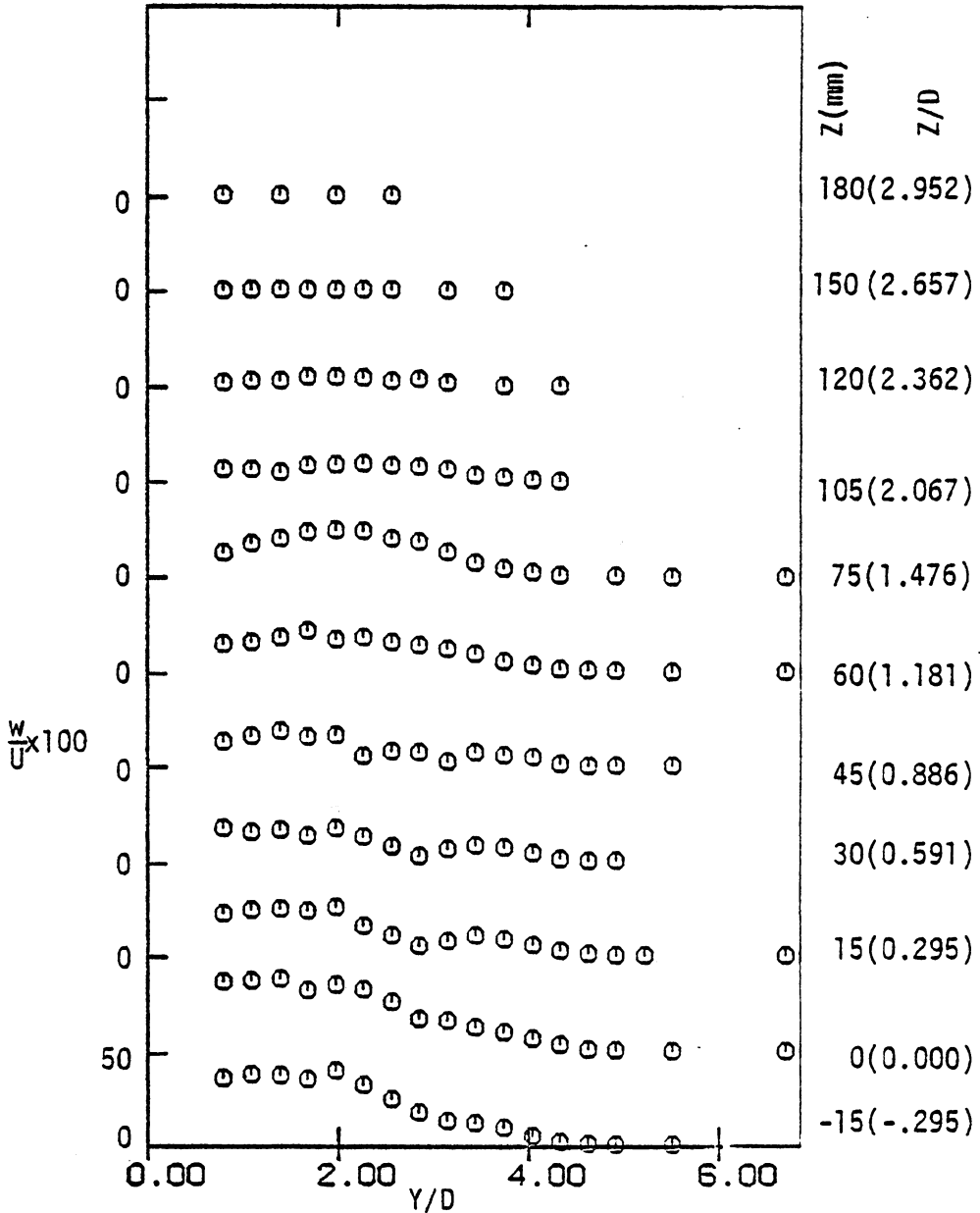


Fig.29 - Vertical distribution of the horizontal turbulence intensity; single jet; $X/D = 7$.

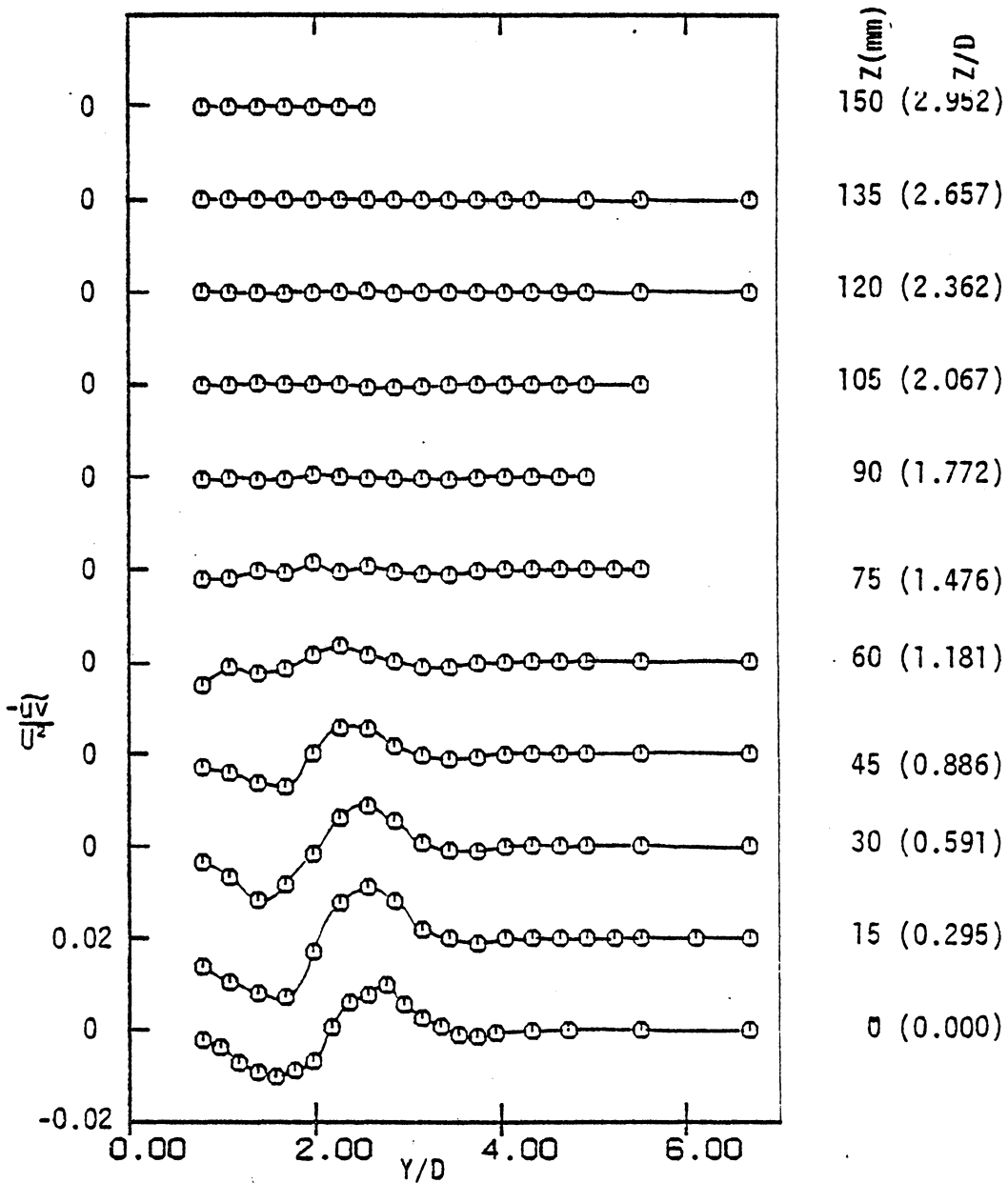


Fig.30 - Vertical distribution of the vertical shear stress; single jet; X/D = 7

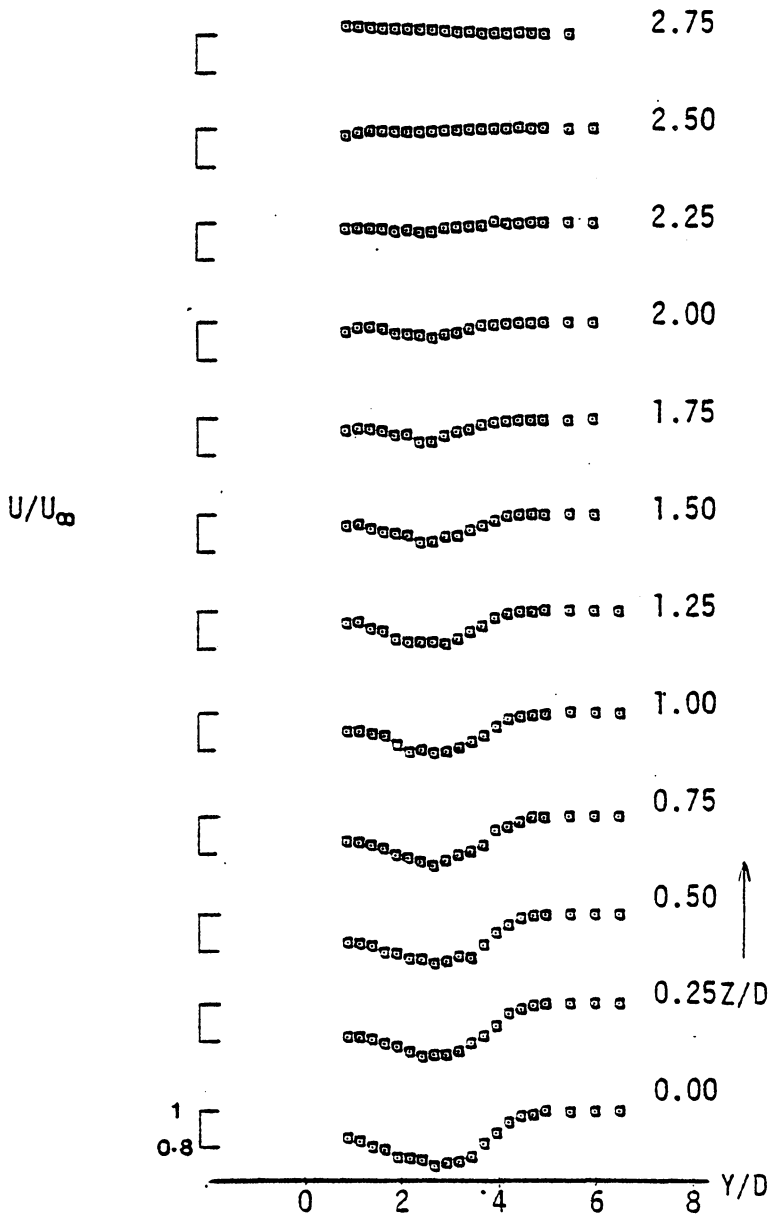


Fig.31-Vertical distribution of the axial mean velocity; single jet; X/D = 10.

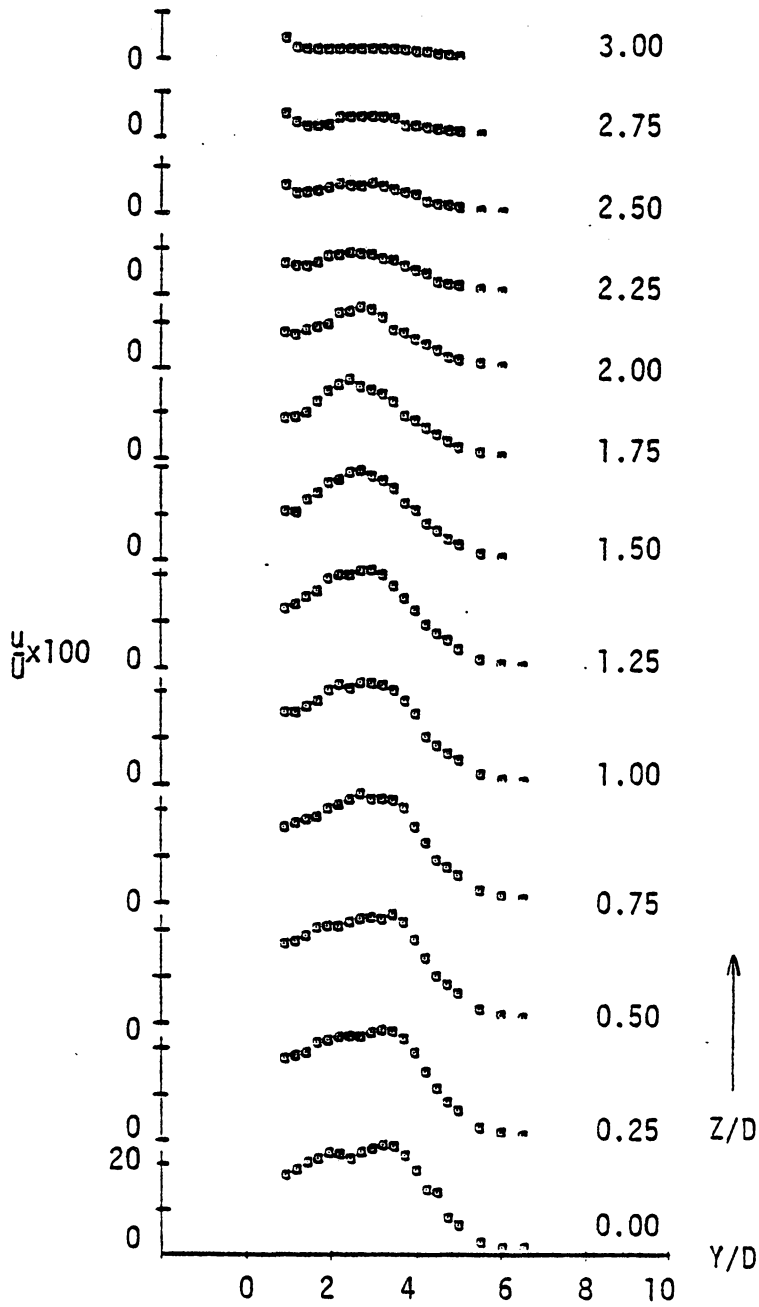


Fig.32 - Vertical distribution of axial turbulence intensity; single jet; $X/D = 10$.

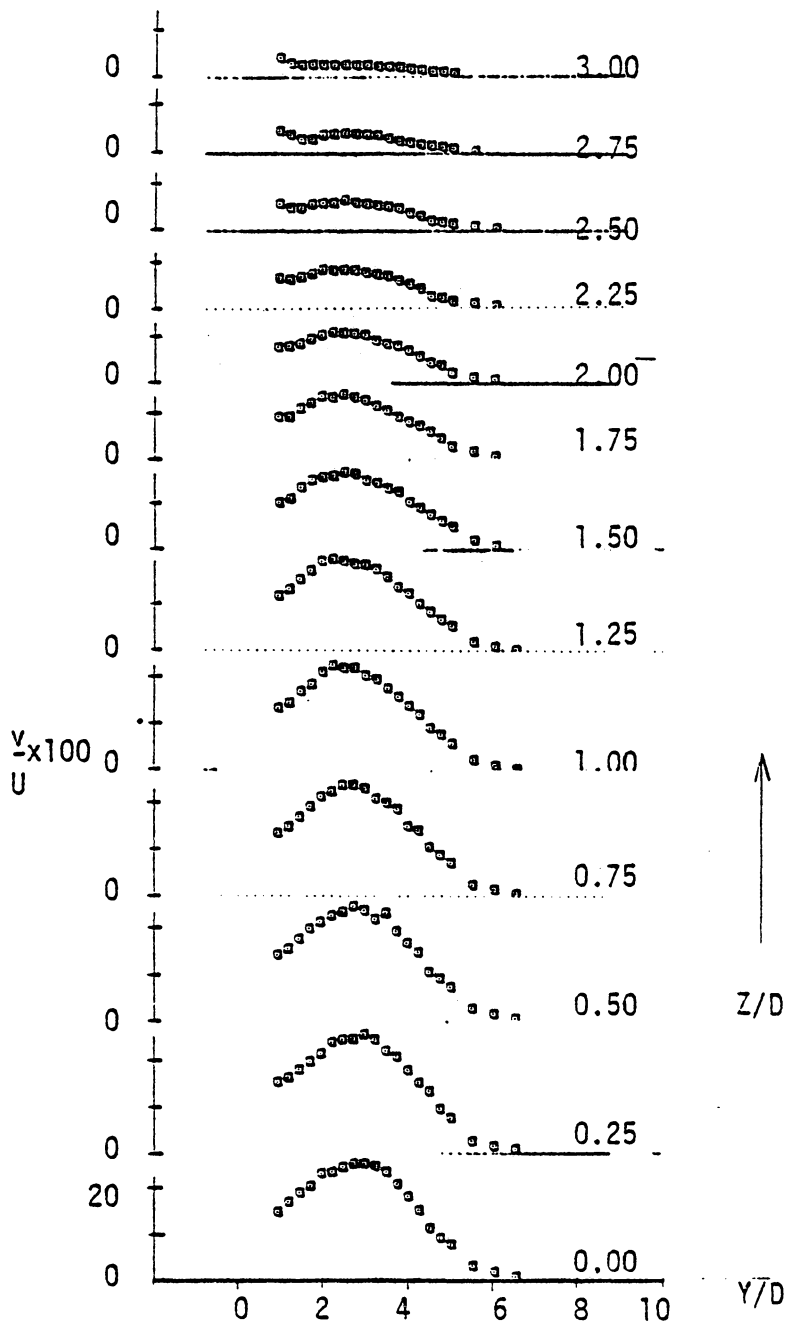


Fig.33 - Vertical distribution of the vertical turbulence intensity; single jet; $X/D = 10$.

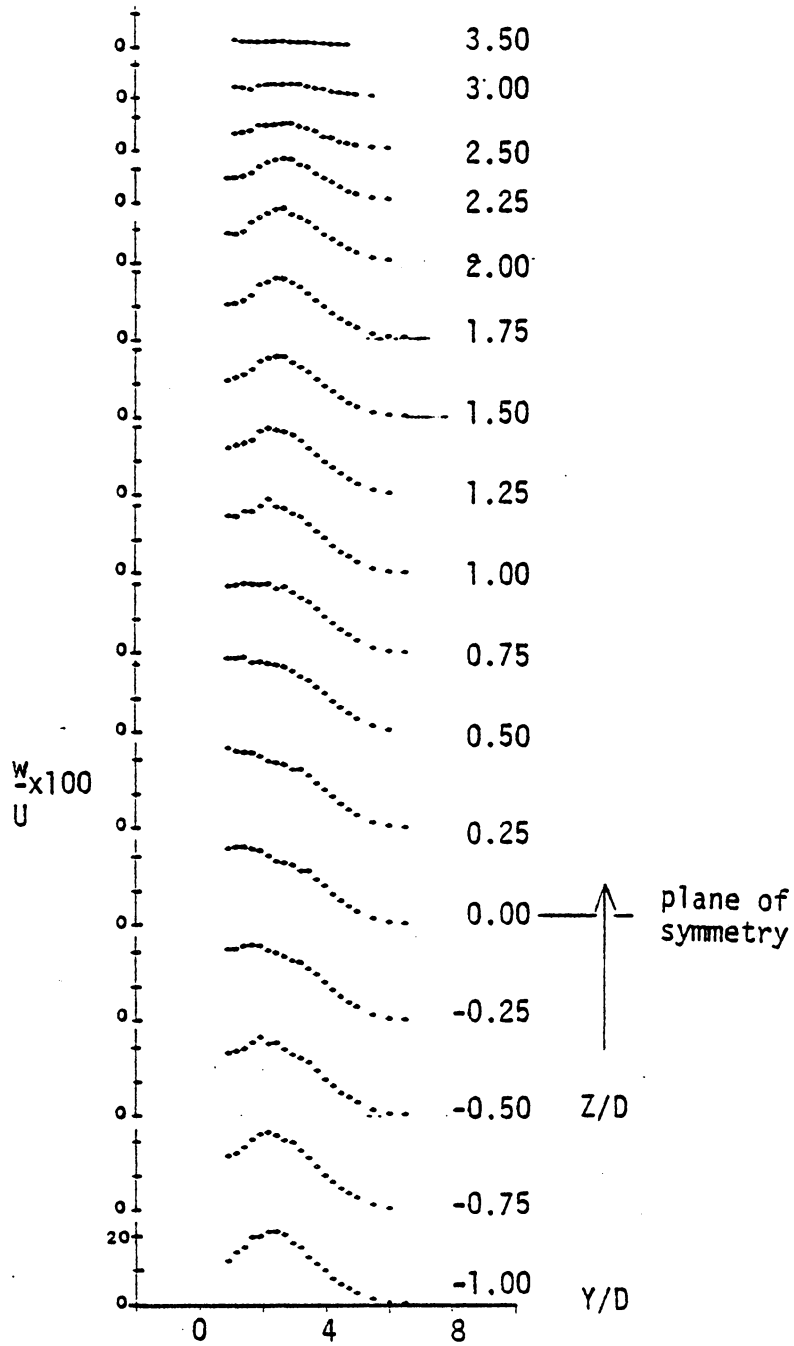


Fig.34 - Vertical distribution of the horizontal turbulence intensity; single jet; $X/D = 10$.

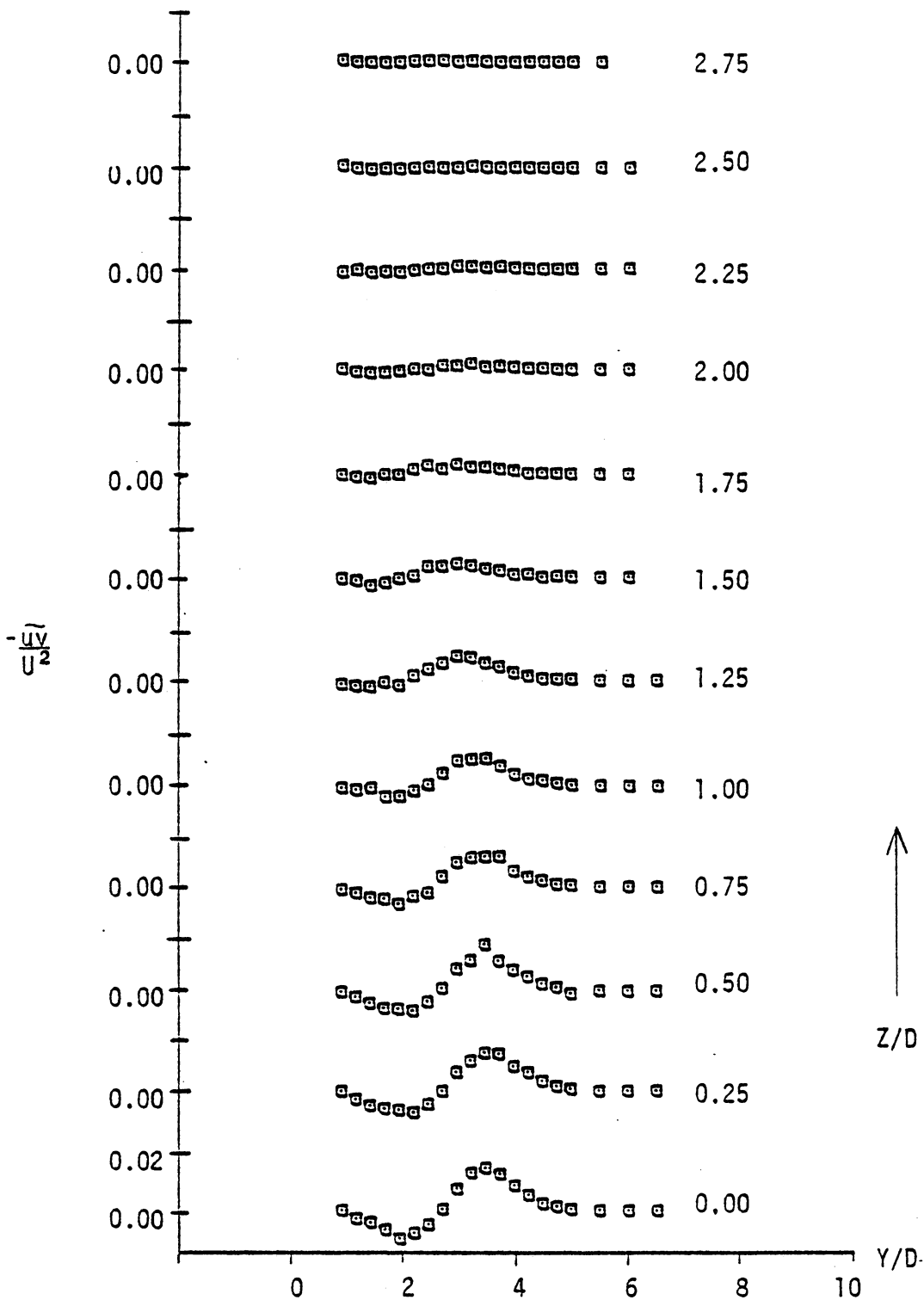


Fig.35 - Vertical distribution of the vertical shear stress; single jet; $X/D = 10$.

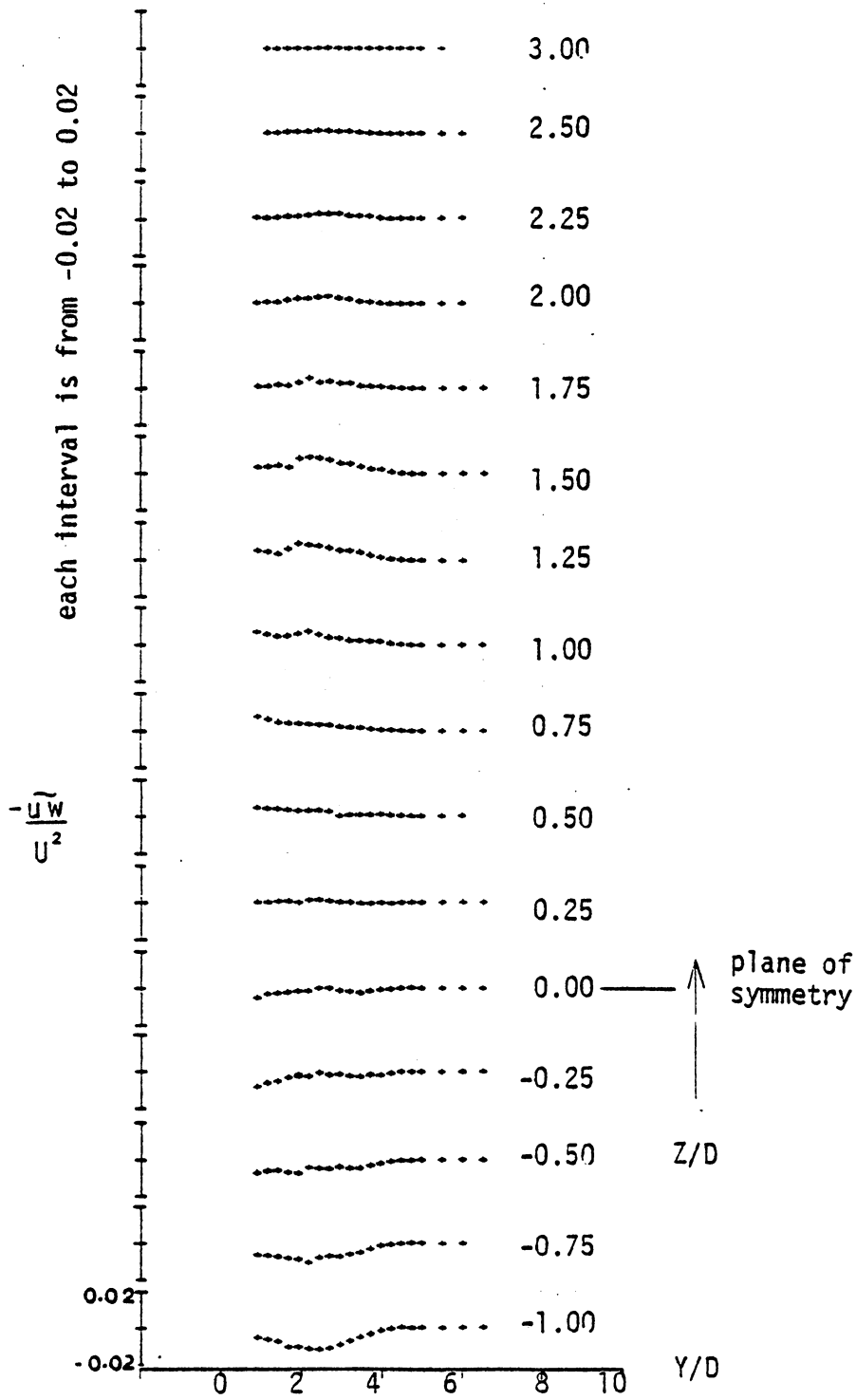


Fig.36 - Vertical distribution of the horizontal shear stress; single jet; X/D = 10.

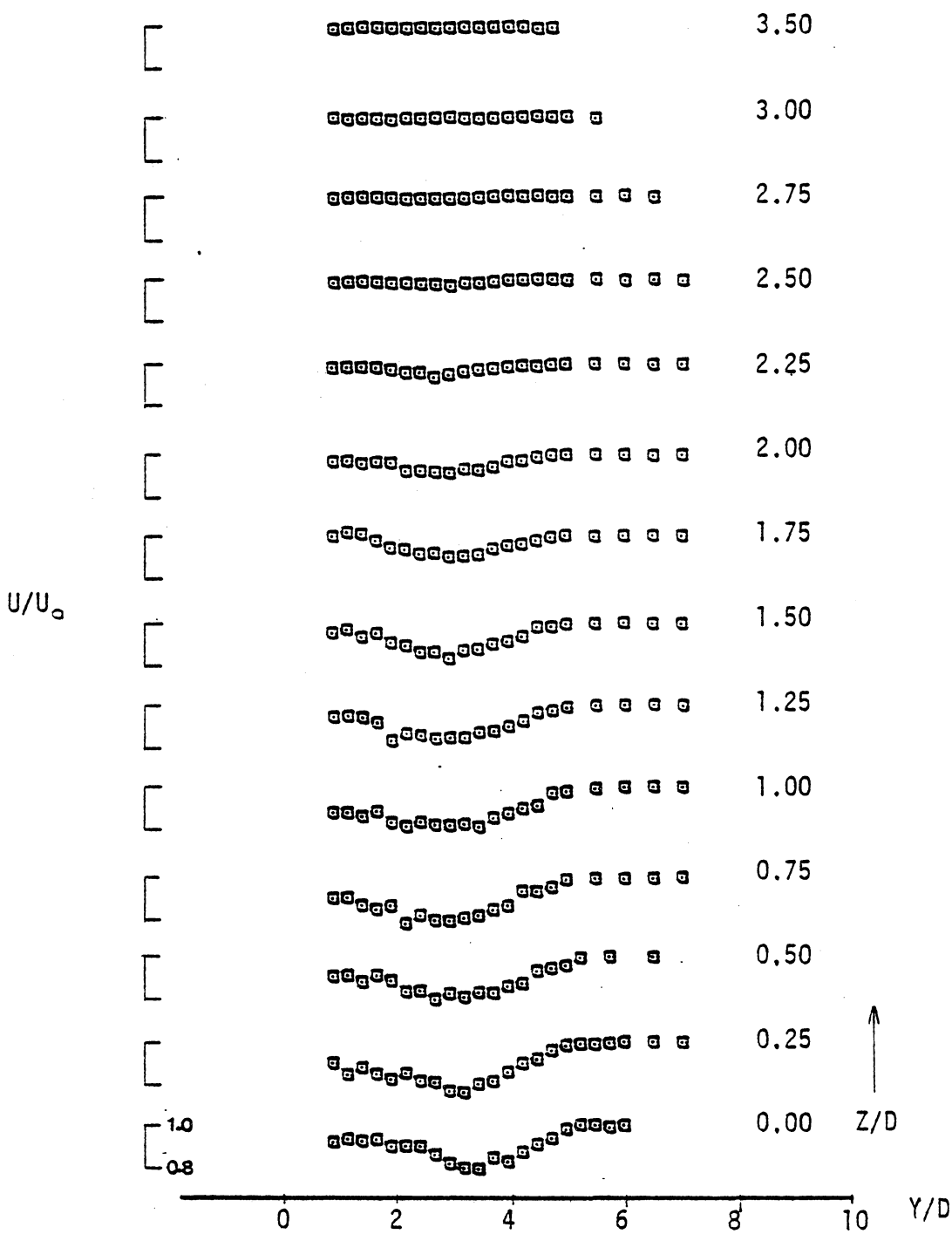


Fig.37 - Vertical distribution of the Axial mean velocity; single jet; X/D = 14

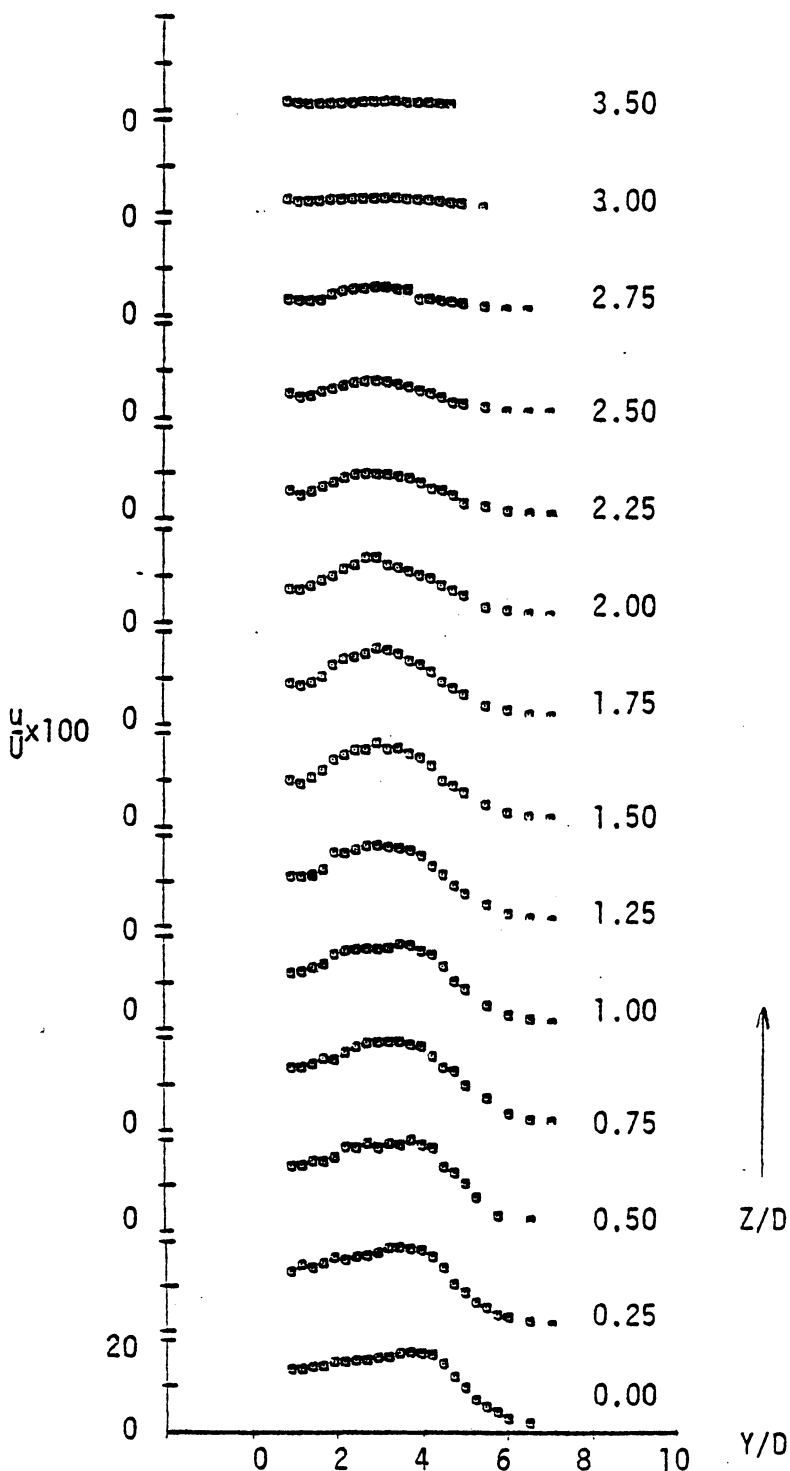


Fig.38 - Vertical distribution of axial turbulence intensity; single jet; $X/D = 14$.

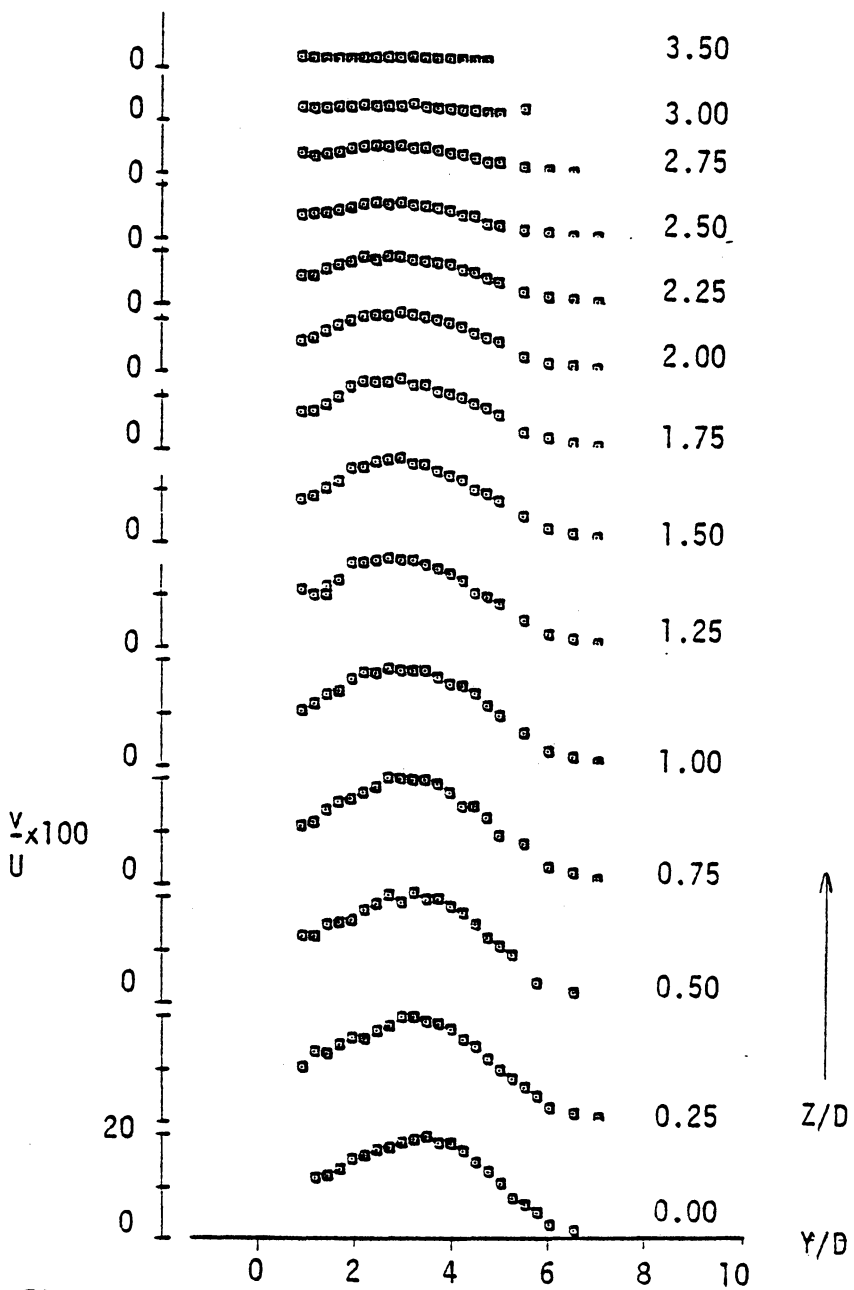


Fig.39 - Vertical distribution of the vertical turbulence intensity; single jet; $X/D = 14$.

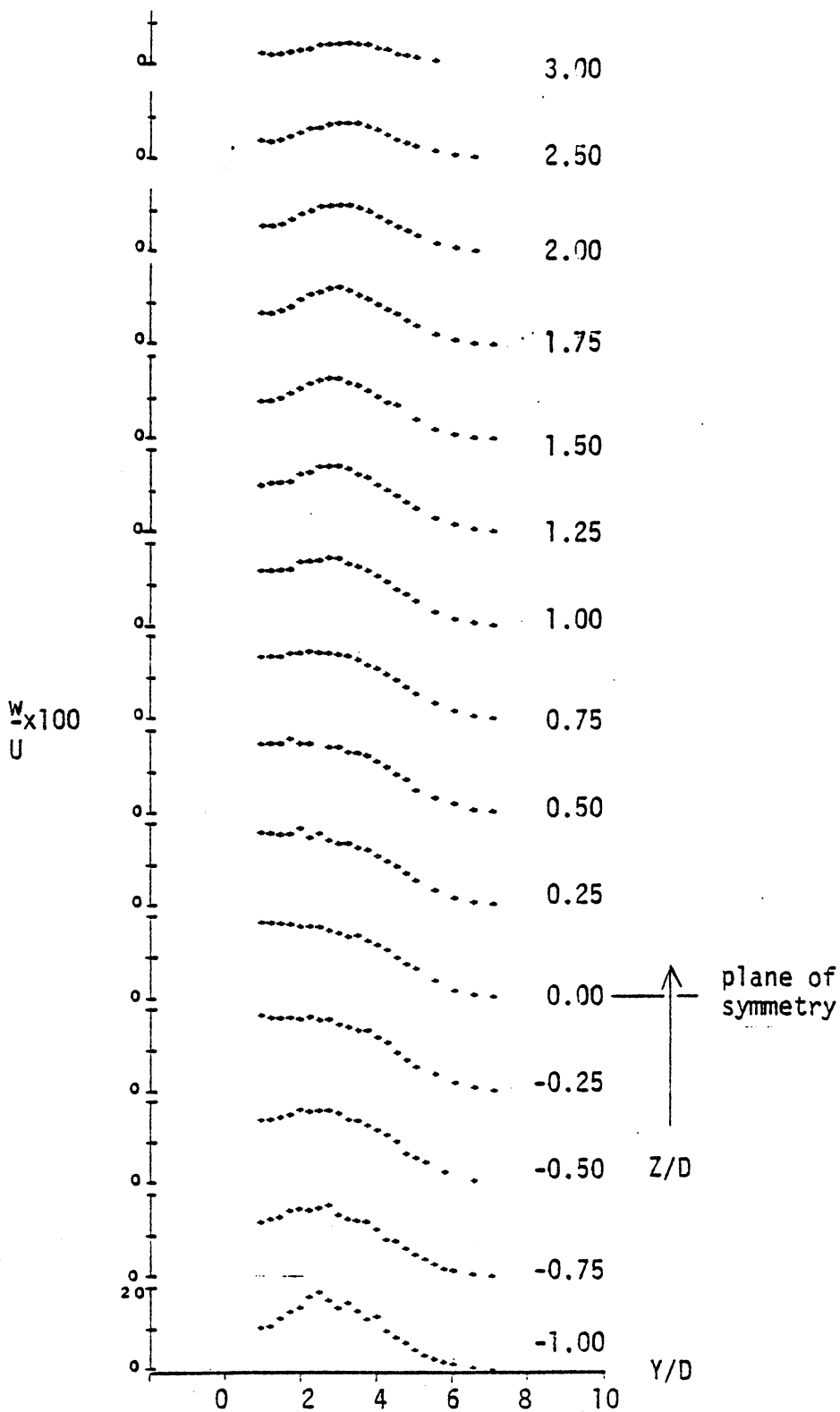


Fig.40 - Vertical distribution of the horizontal turbulence intensity; single jet $X/D = 14$.

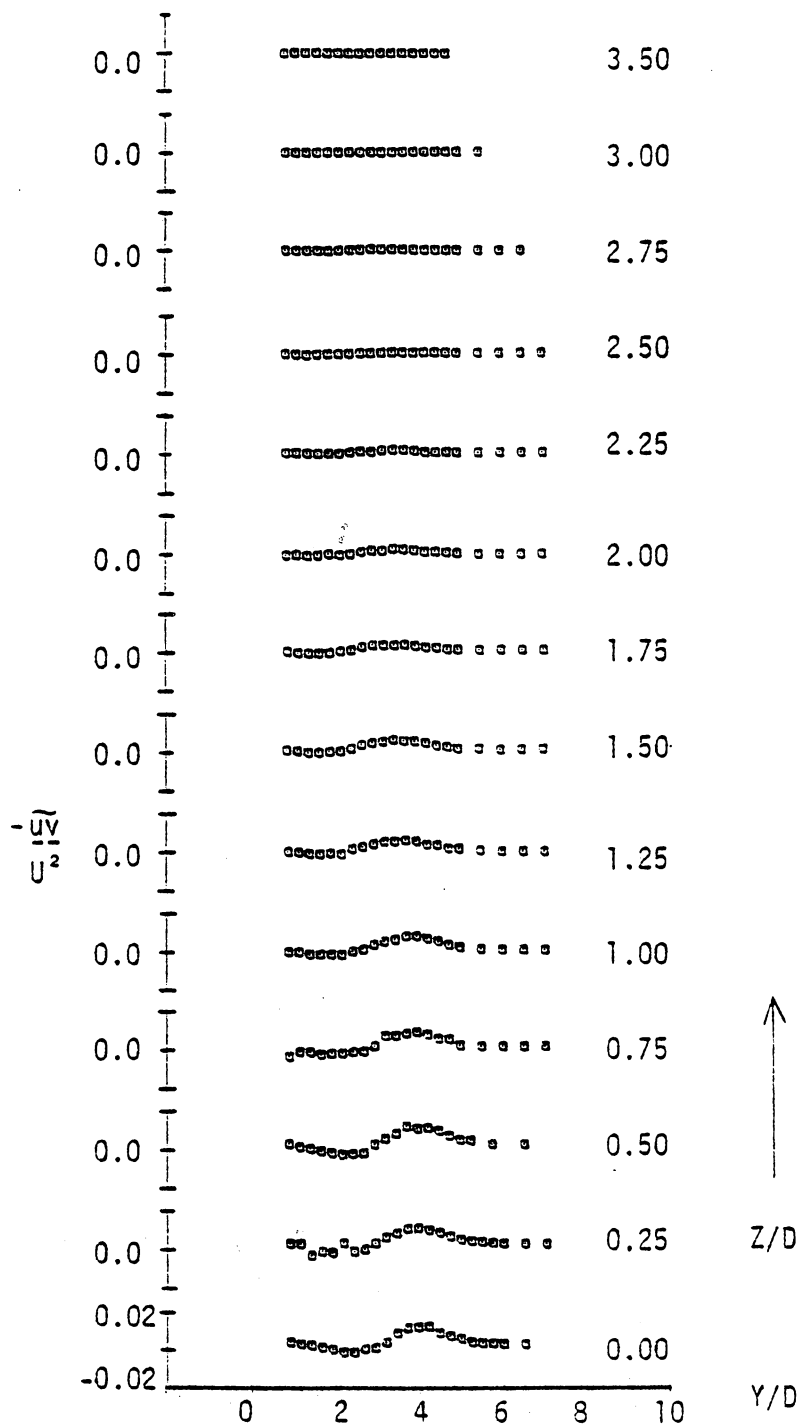


Fig.41 - Vertical distribution of the vertical shear stress; single jet; $X/D = 14$.

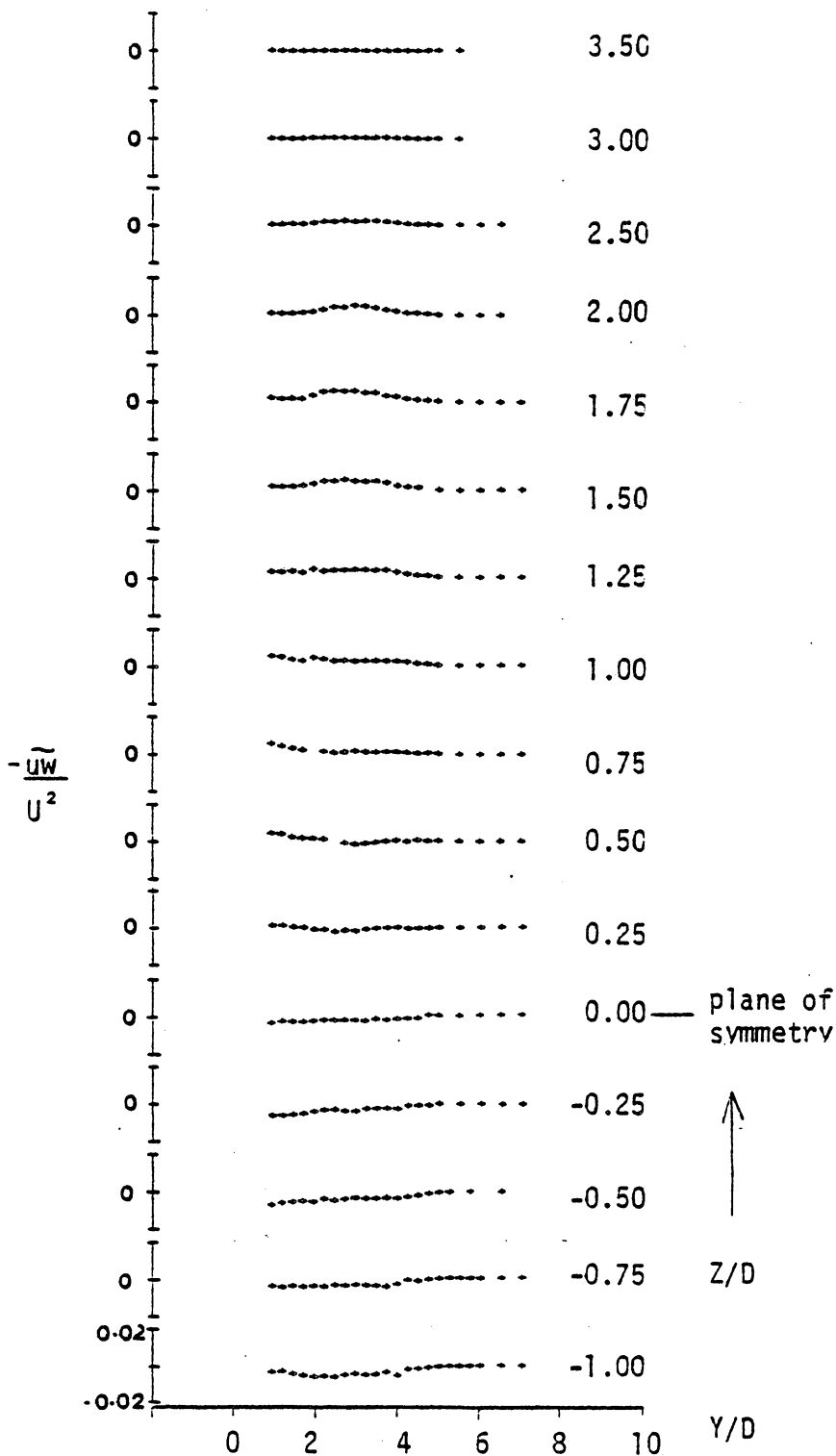


Fig.42 - Vertical distribution of horizontal shear stress; single jet; $X/D = 14$.

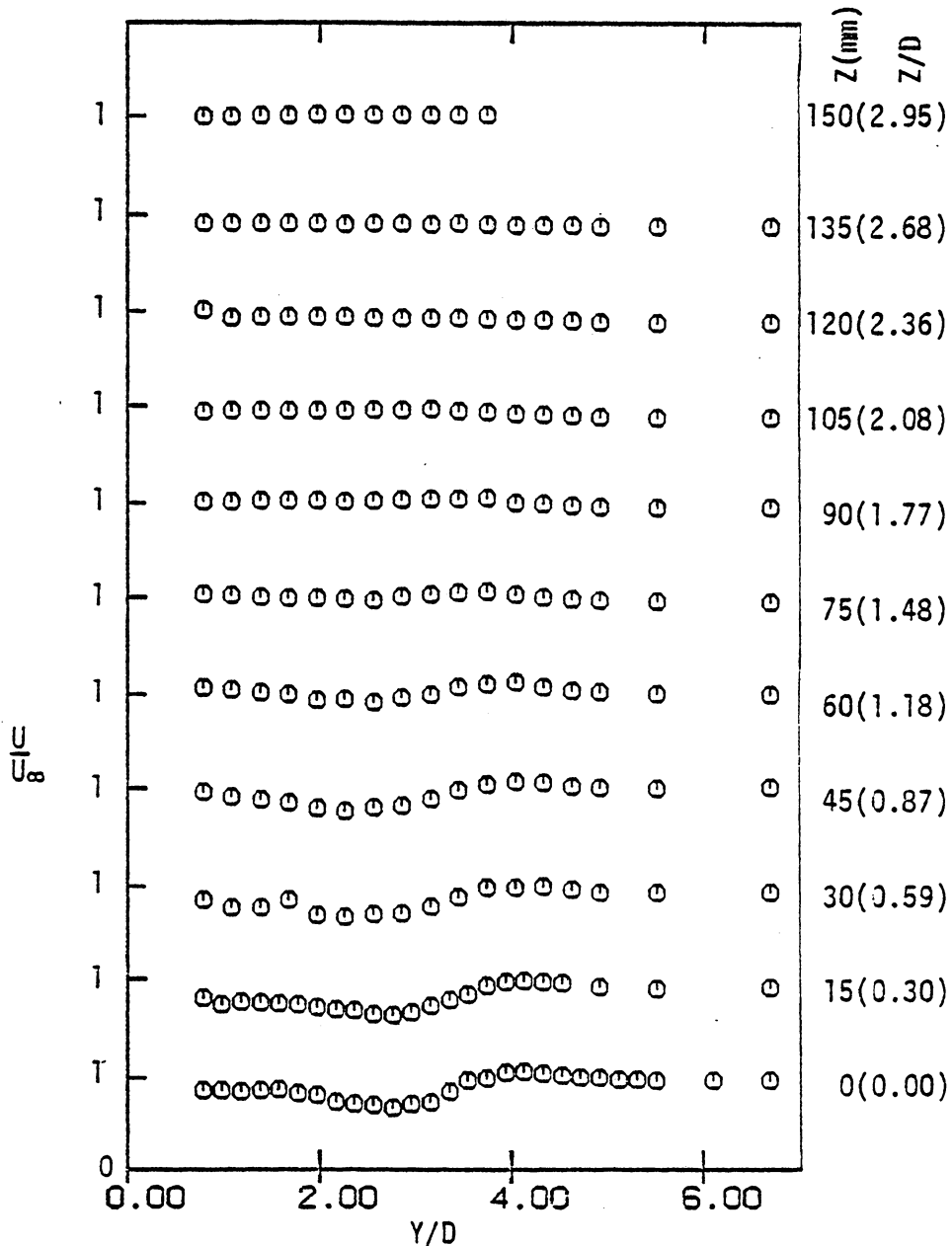


Fig.43 - Vertical distribution of the axial mean velocity; tandem plume configuration

X/D=3

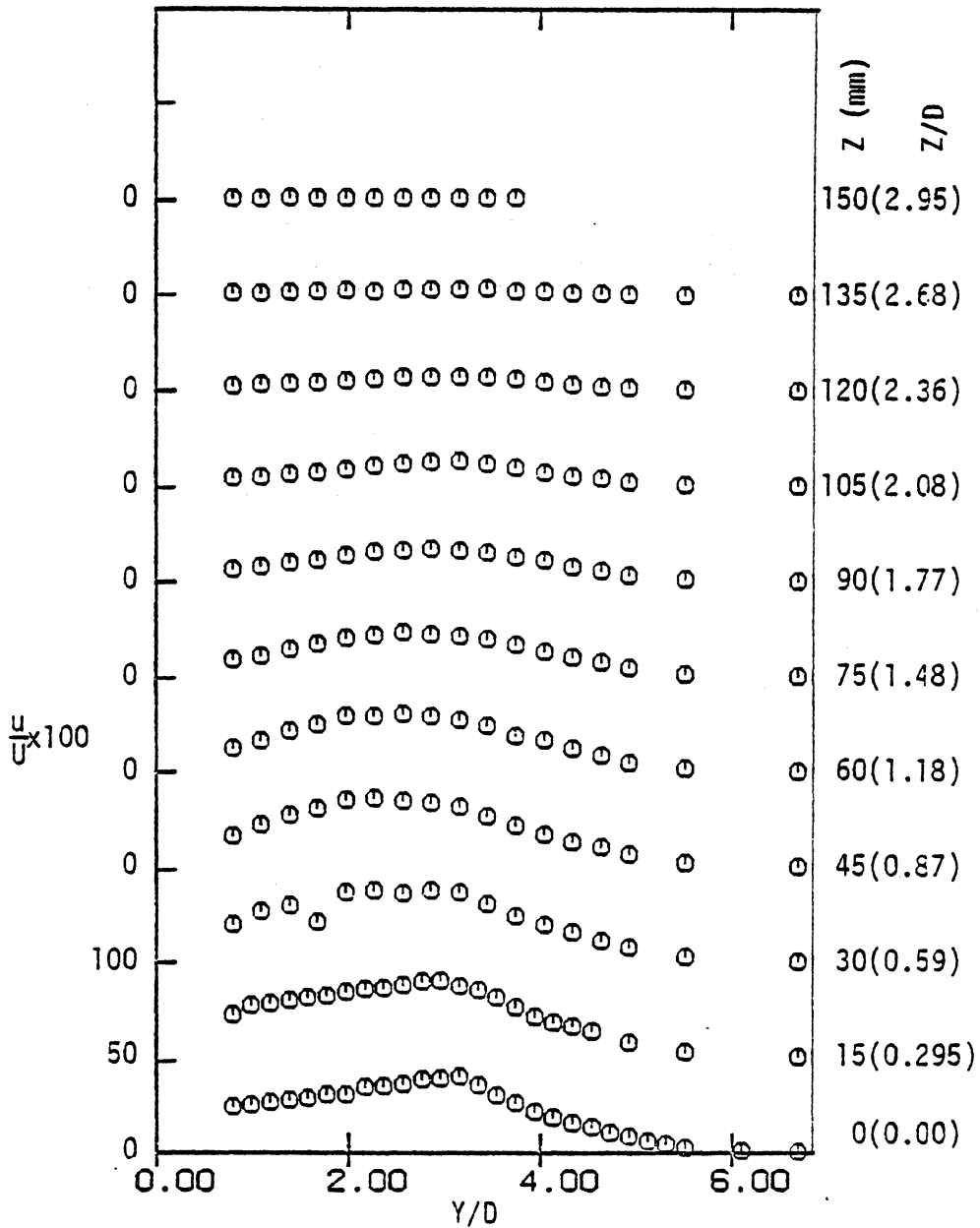


Fig.44 - Vertical distribution of the axial turbulence intensity; tandem plume configuration; X/D=3.

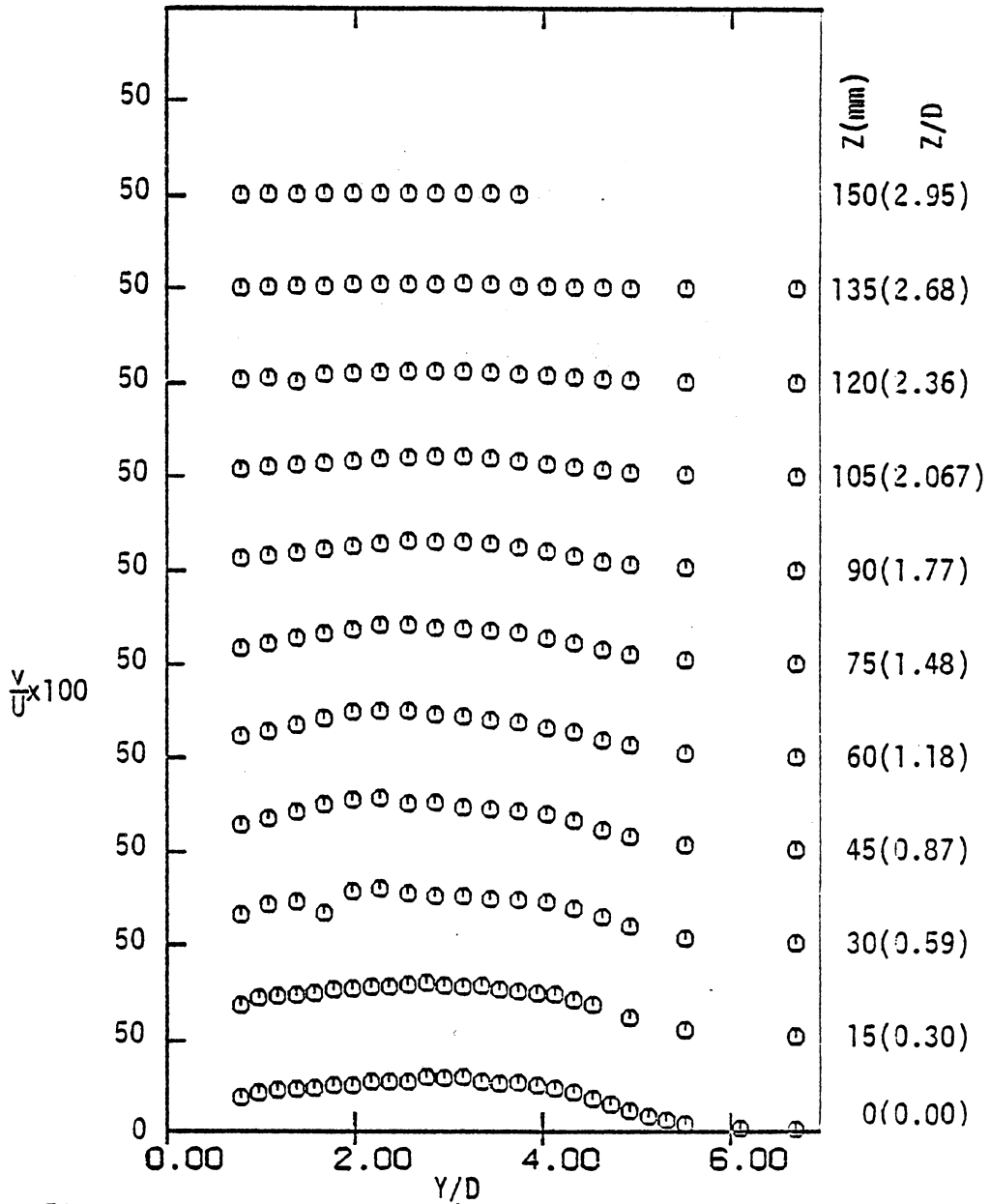


Fig.45 - Vertical distribution of the vertical turbulence intensity; tandem plume configuration; $X/D = 3$.

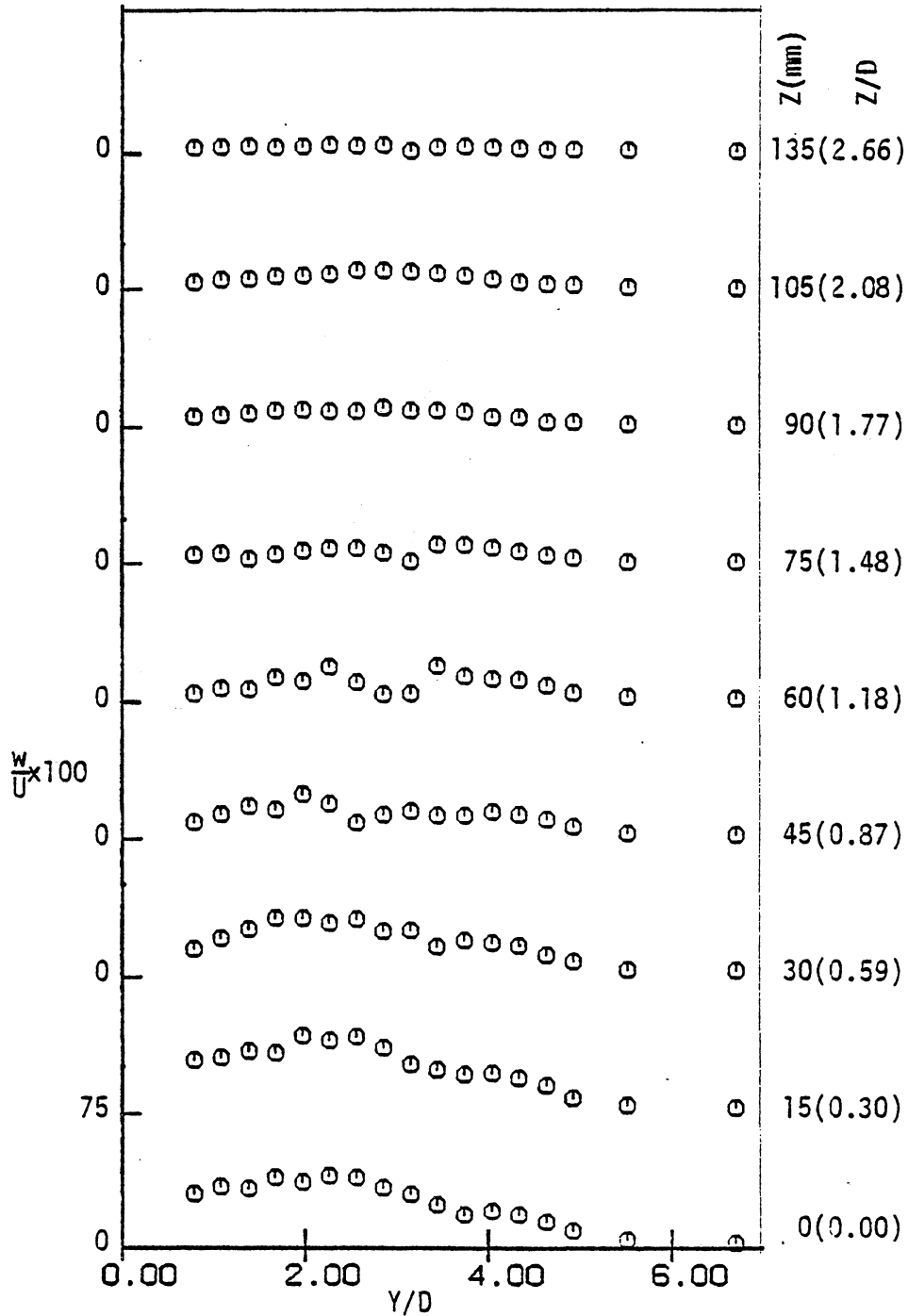


Fig.46 - Vertical distribution of the horizontal turbulence intensity; tandem plume configuration; X/D = 3.

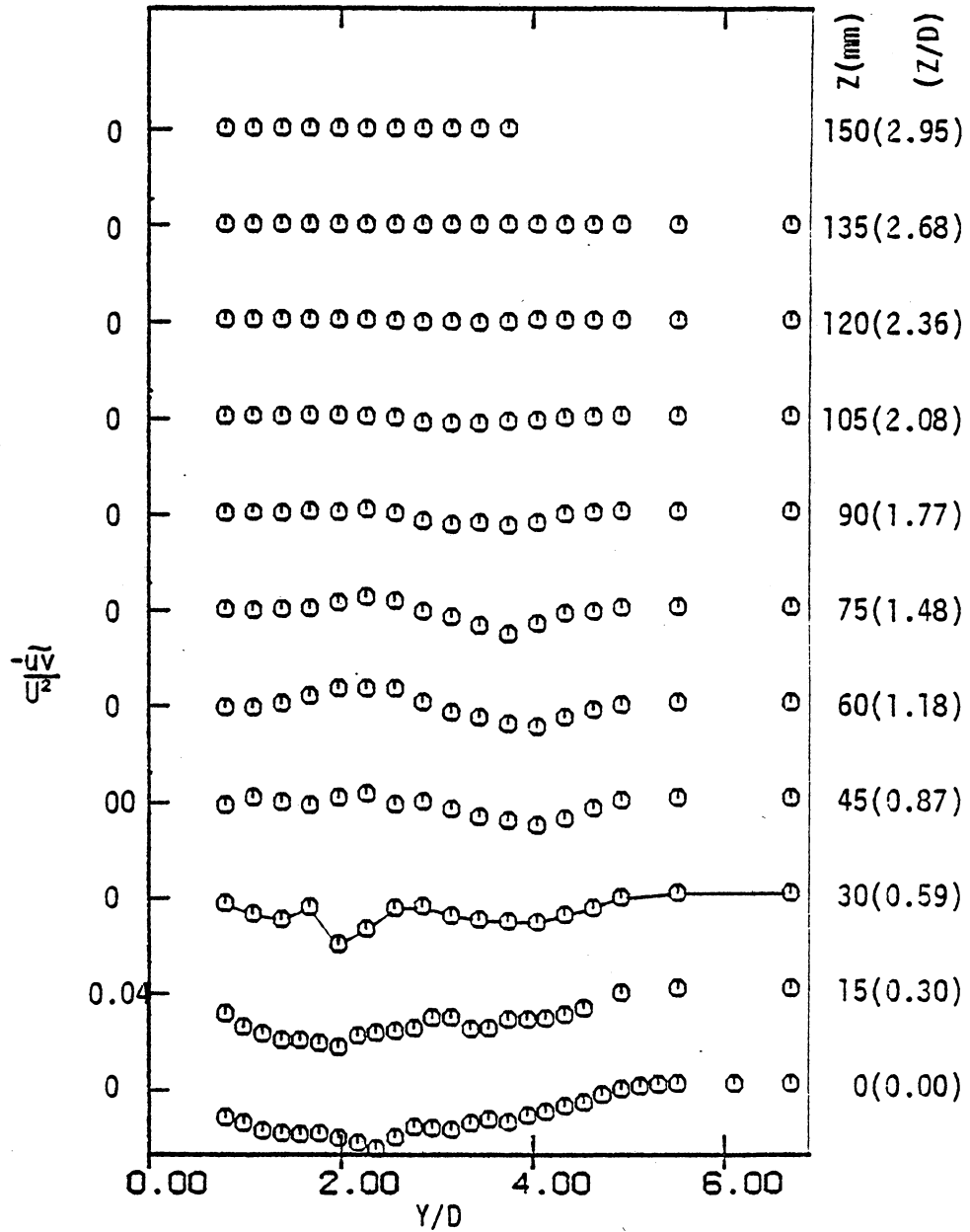


Fig. 47 - Vertical distribution of the vertical shear stress; tandem plume configuration; $X/D = 3$.

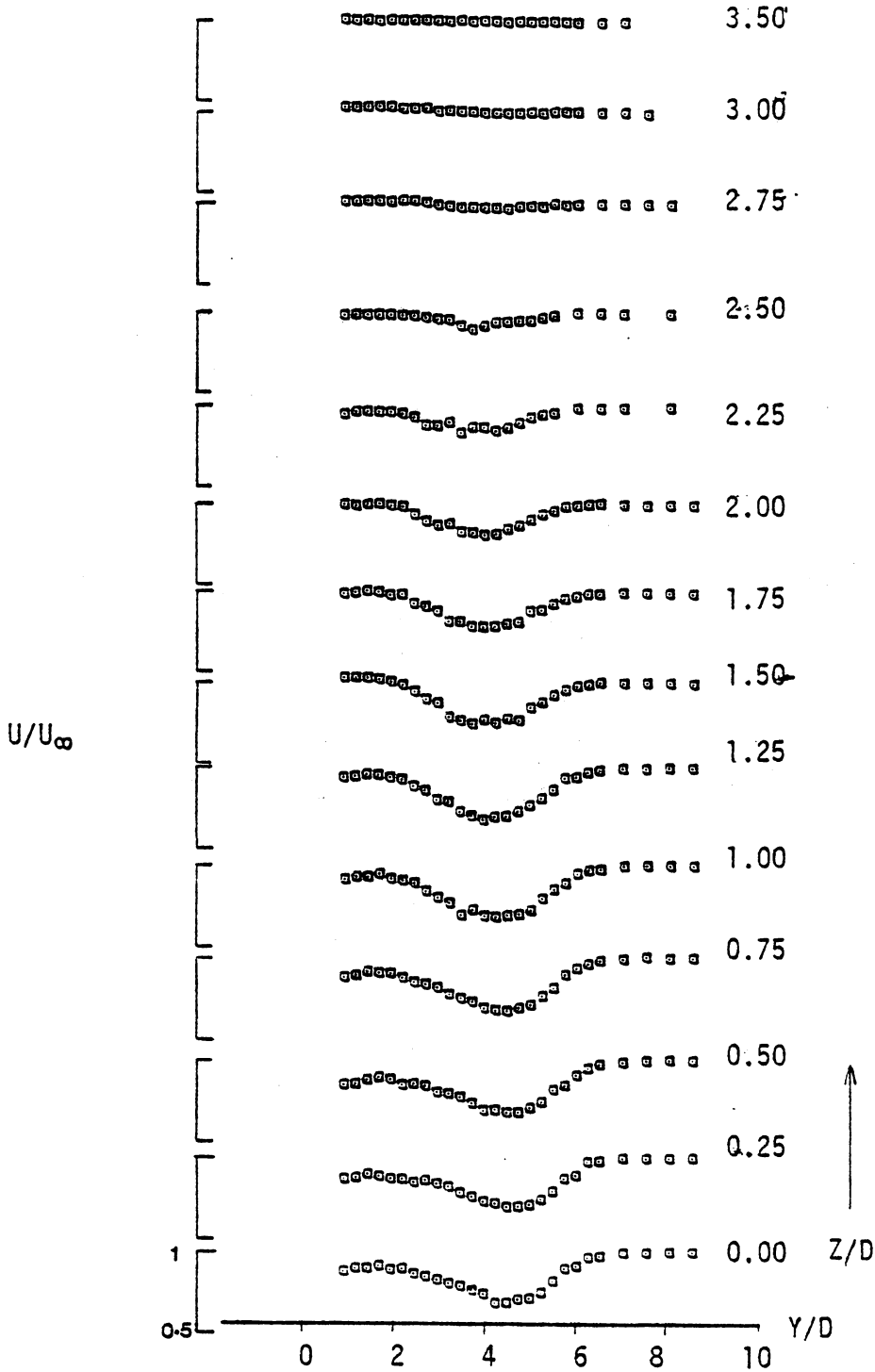


Fig.48 - Vertical distribution of the axial mean velocity; tandem plume configuration; $X/D = 10$

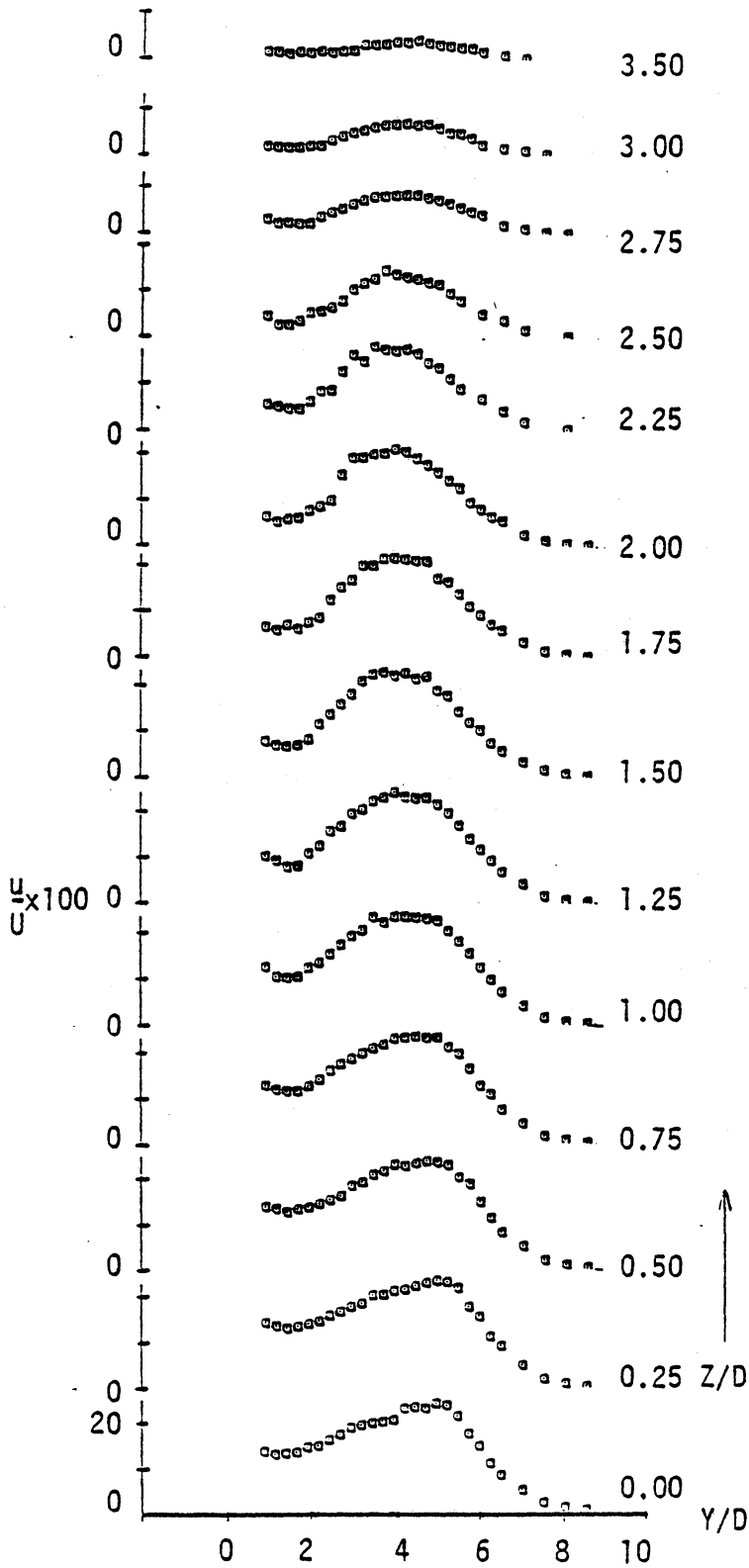


Fig.49 - Vertical distribution of axial turbulence intensity; tandem plume configuration; $X/D = 10$.

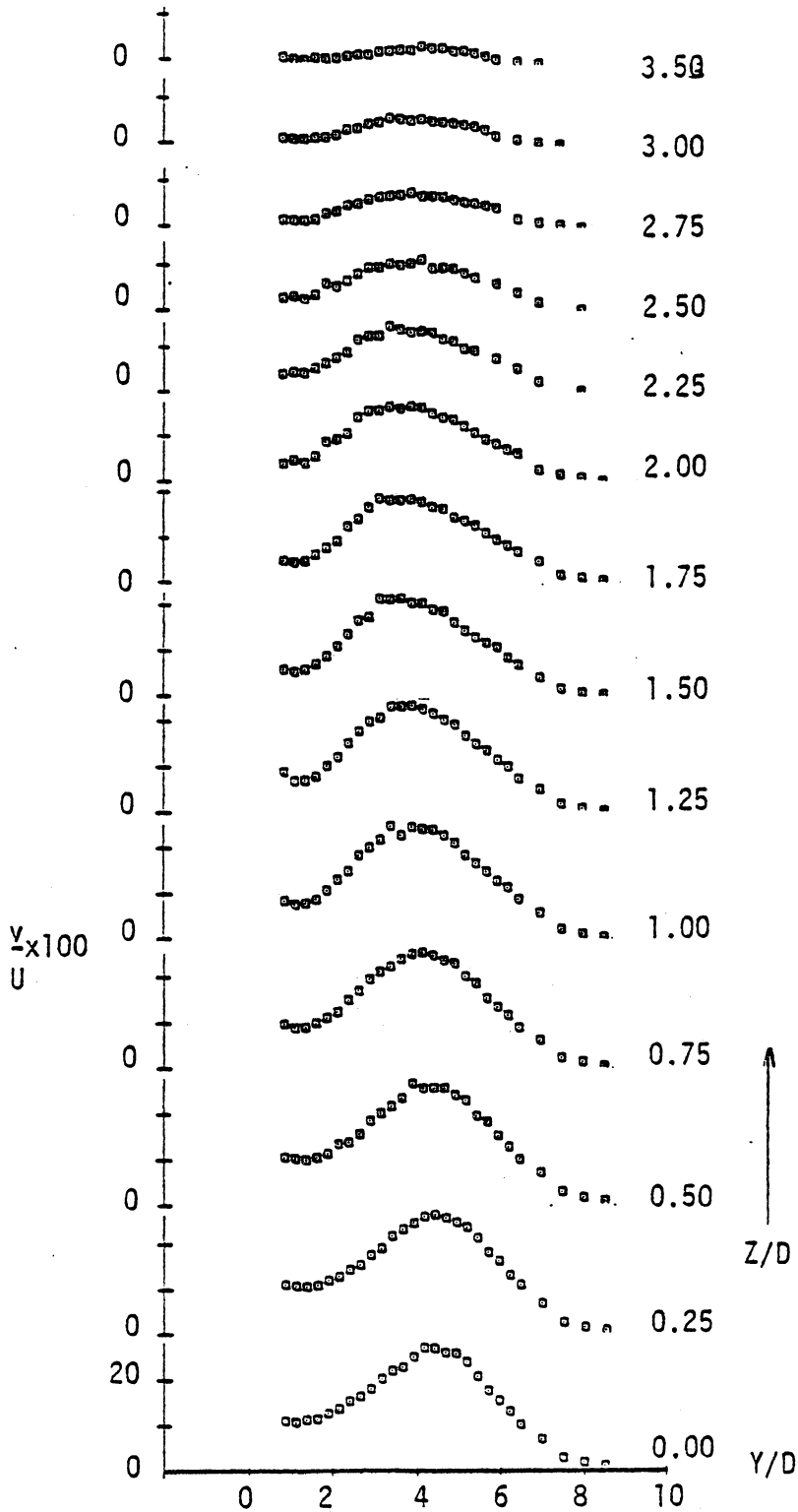


Fig.50 - Vertical distribution of the vertical turbulence intensity; tandem plume configuration; $X/D = 10$.

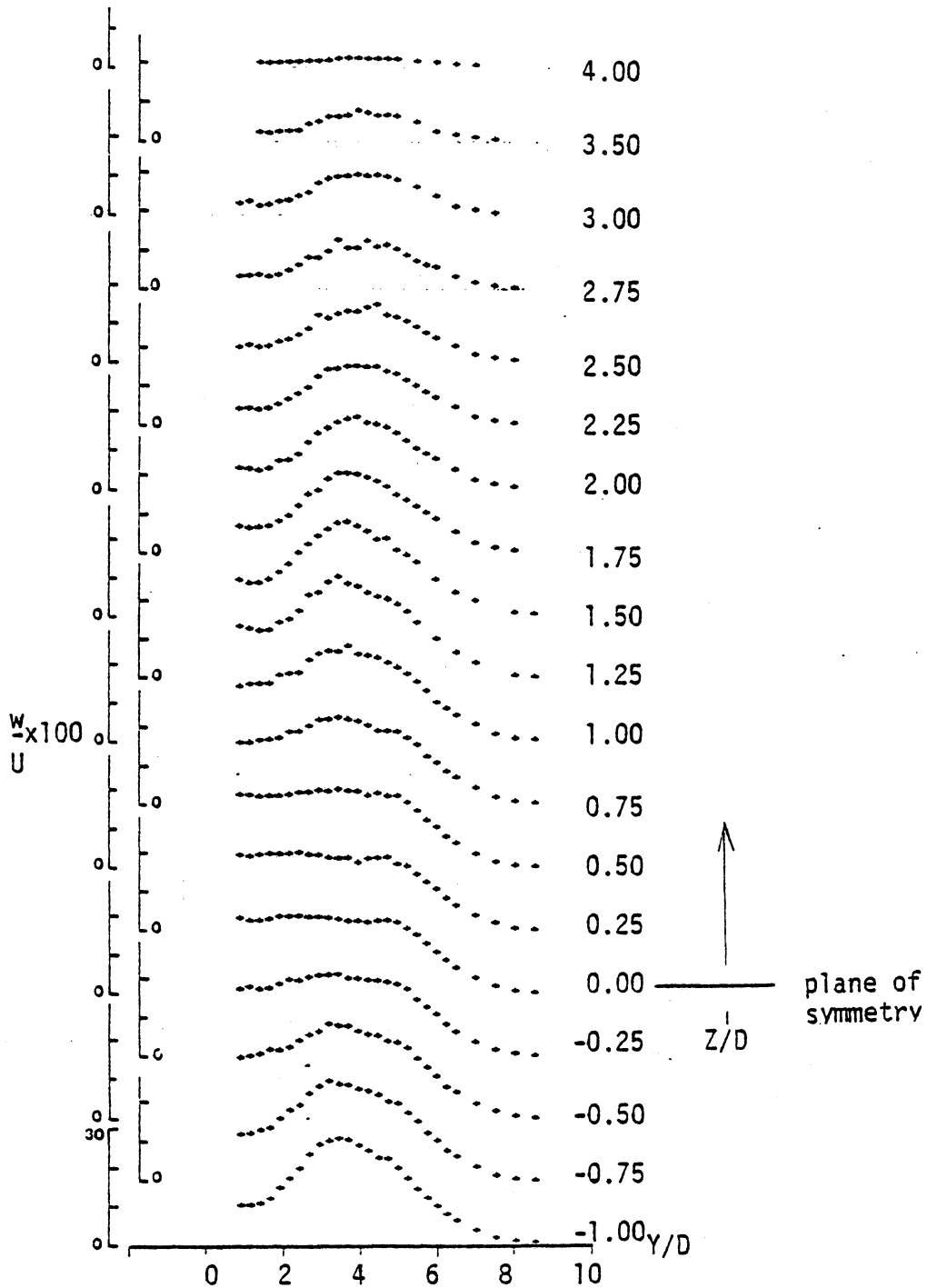


Fig. 51 - Vertical distribution of the horizontal turbulence intensity; tandem plume configuration; $X/D = 10$.

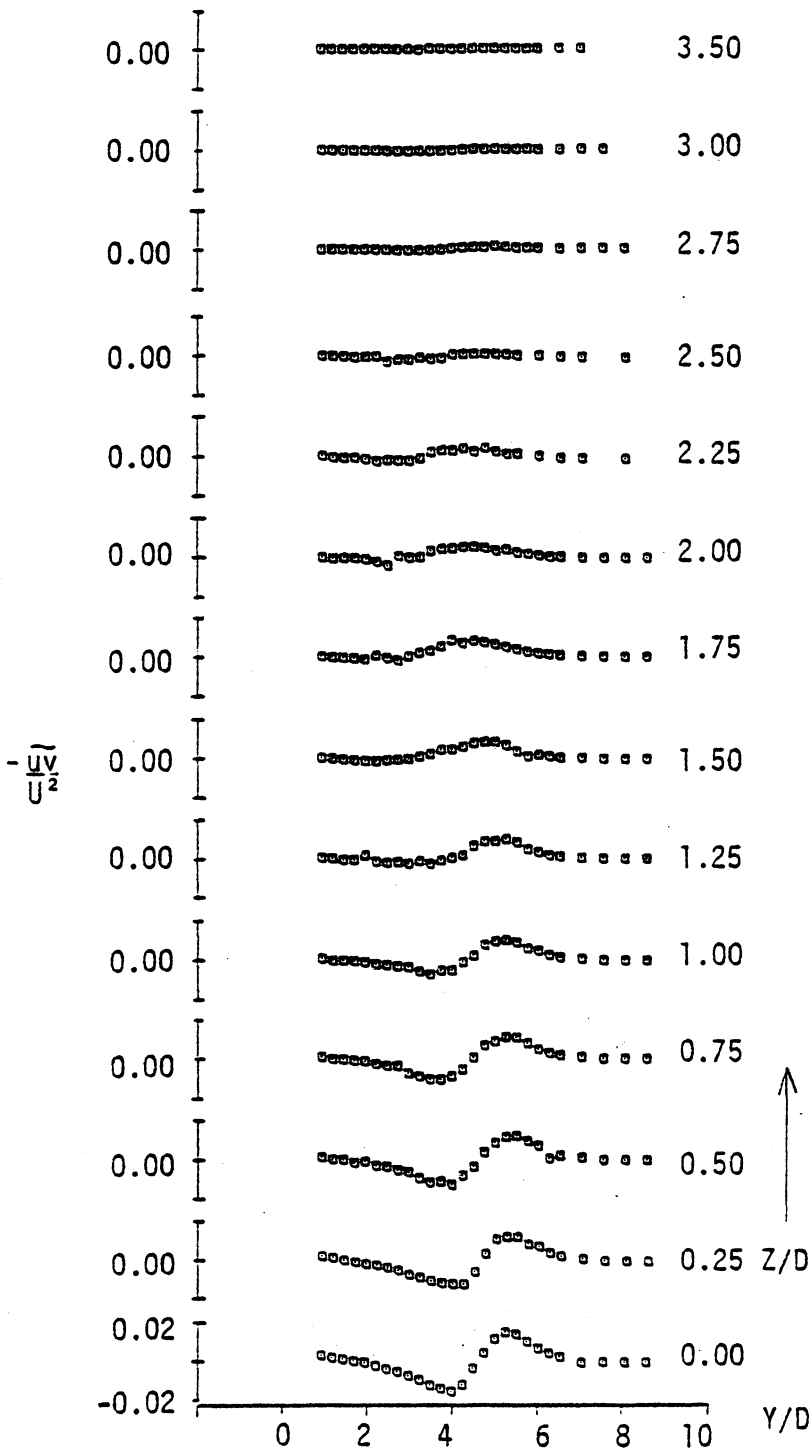


Fig.52 - Vertical distribution of the vertical shear stress; tandem plume configuration; $X/D = 10$.

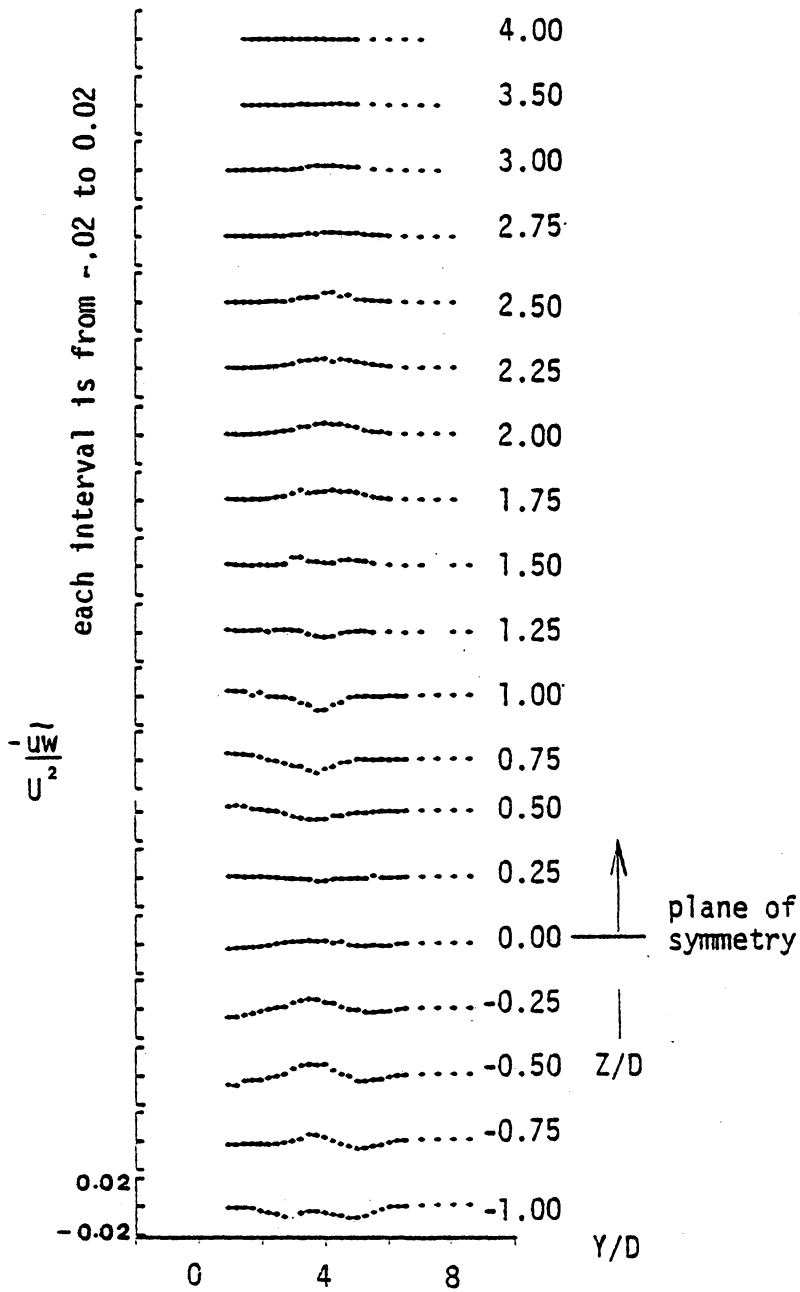


Fig.53 - Vertical distribution of the horizontal shear stress; tandem plume configuration; X/D = 10.

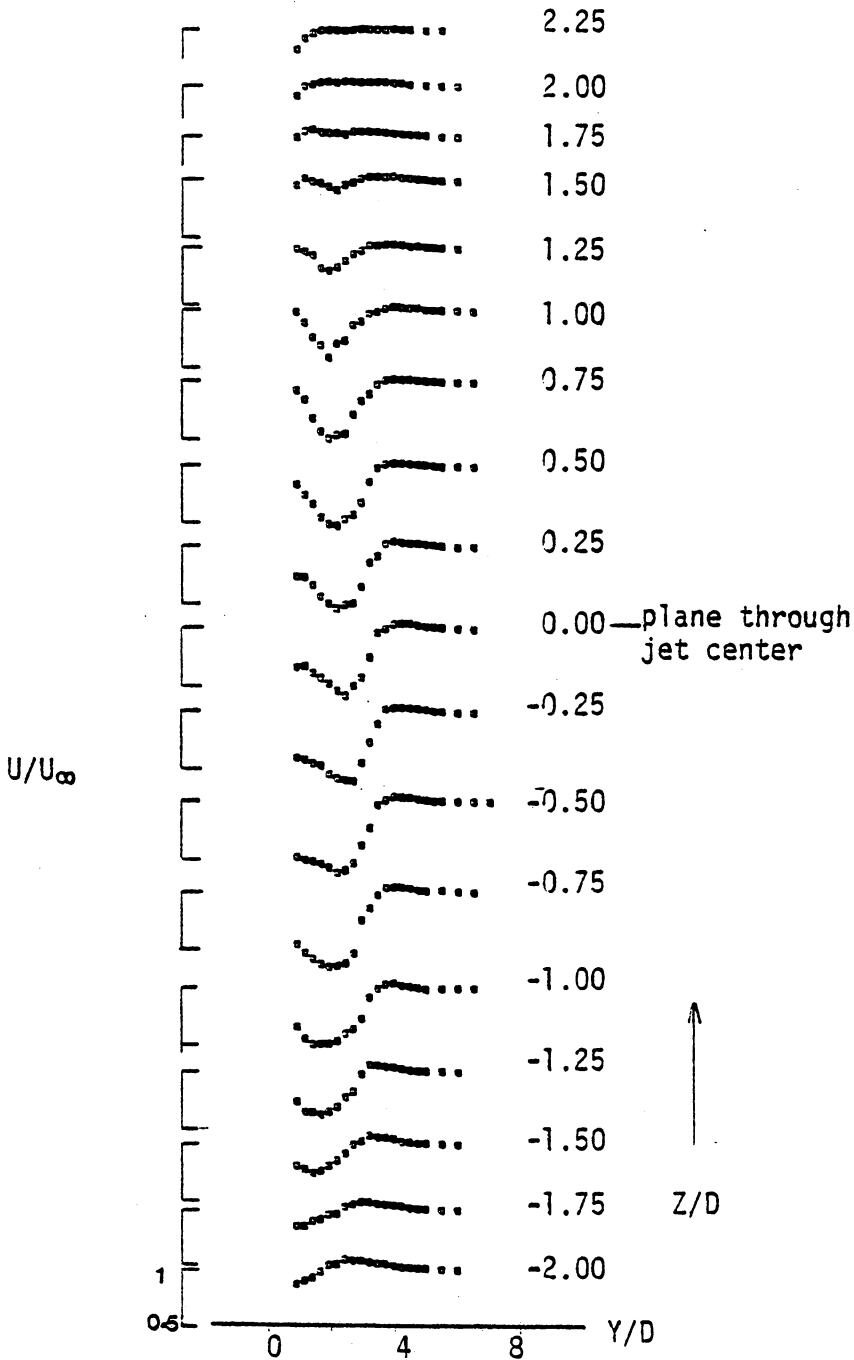


Fig.54 - Vertical distribution of the axial mean velocity: side-by-side plume configuration; $X/D=3$.

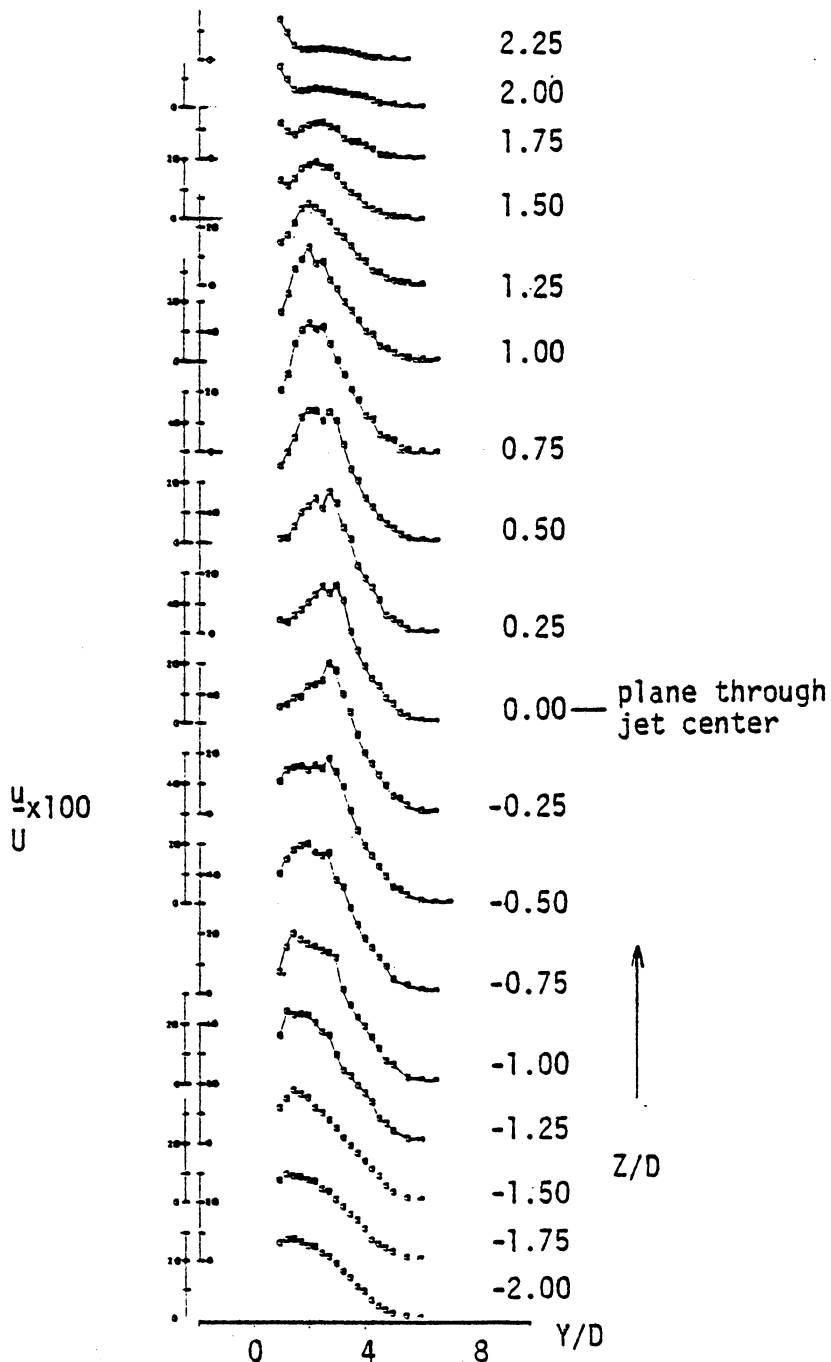


Fig.55 - Vertical distribution of the axial turbulence intensity; side-by-side plume configuration; $X/D = 3$.

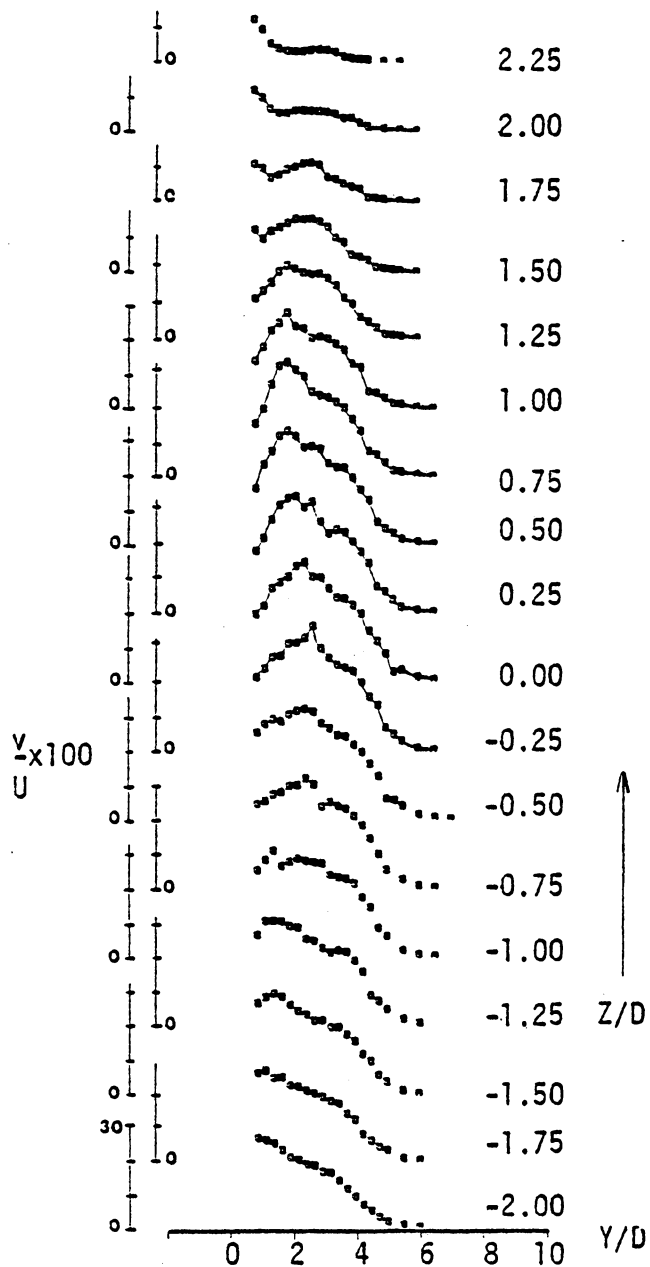


Fig.56 - Vertical distribution of the vertical turbulence intensity; side-by-side plume configuration; $X/D = 3$.

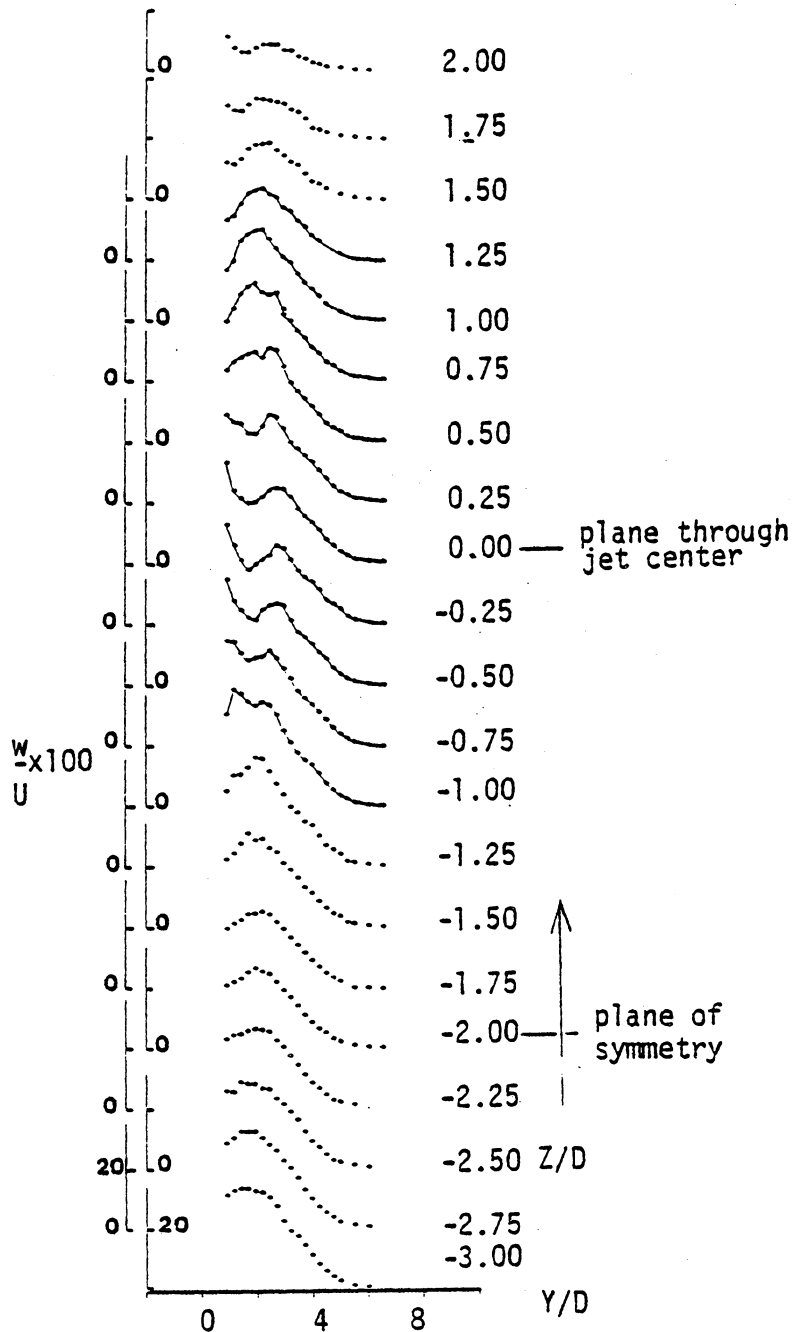


Fig. 57 - Vertical distribution of the horizontal turbulence intensity; side-by-side plume configuration; $Z X/D = 3$.

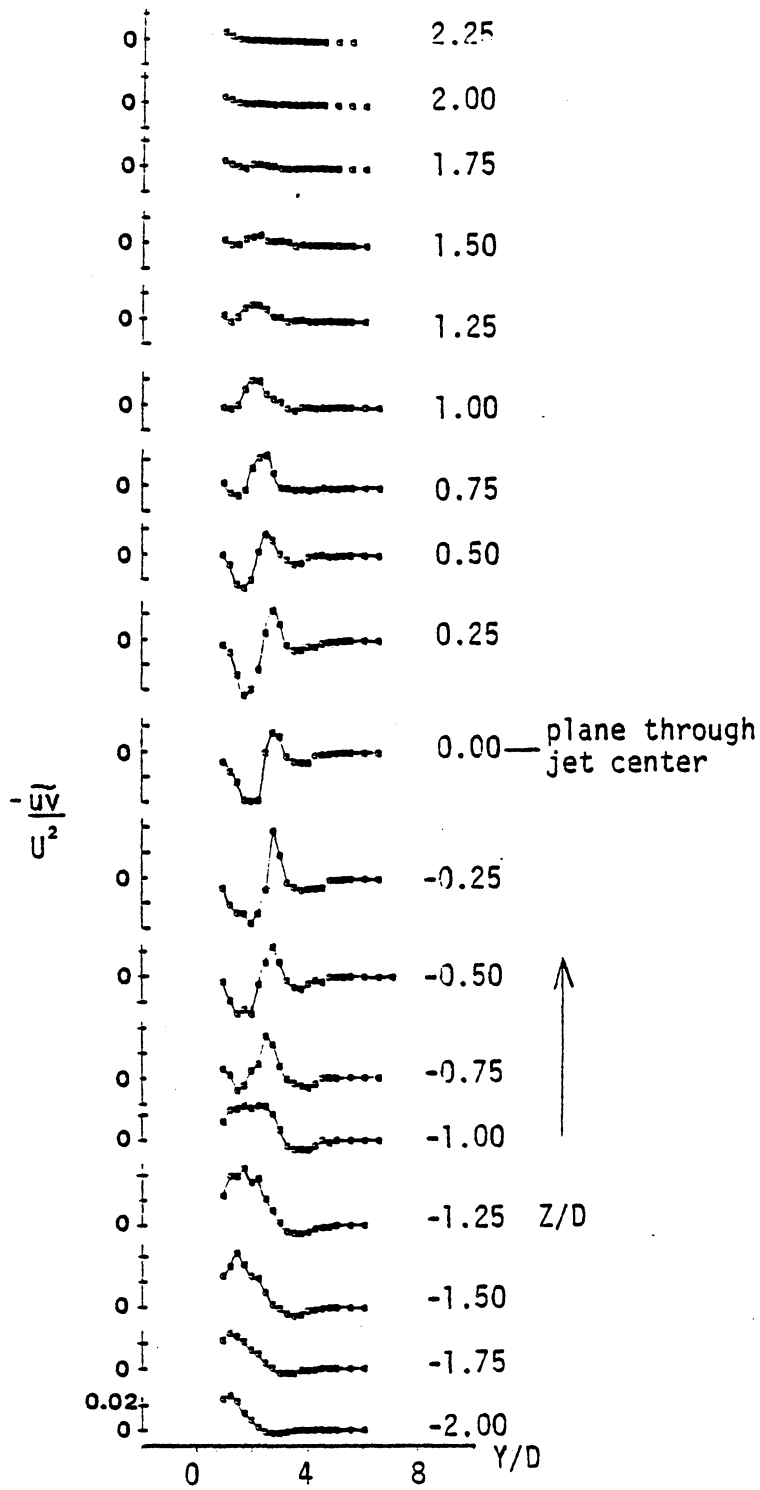


Fig.58 - Vertical distribution of the vertical shear stress; side-by-side jet configuration; $X/D = 3$.

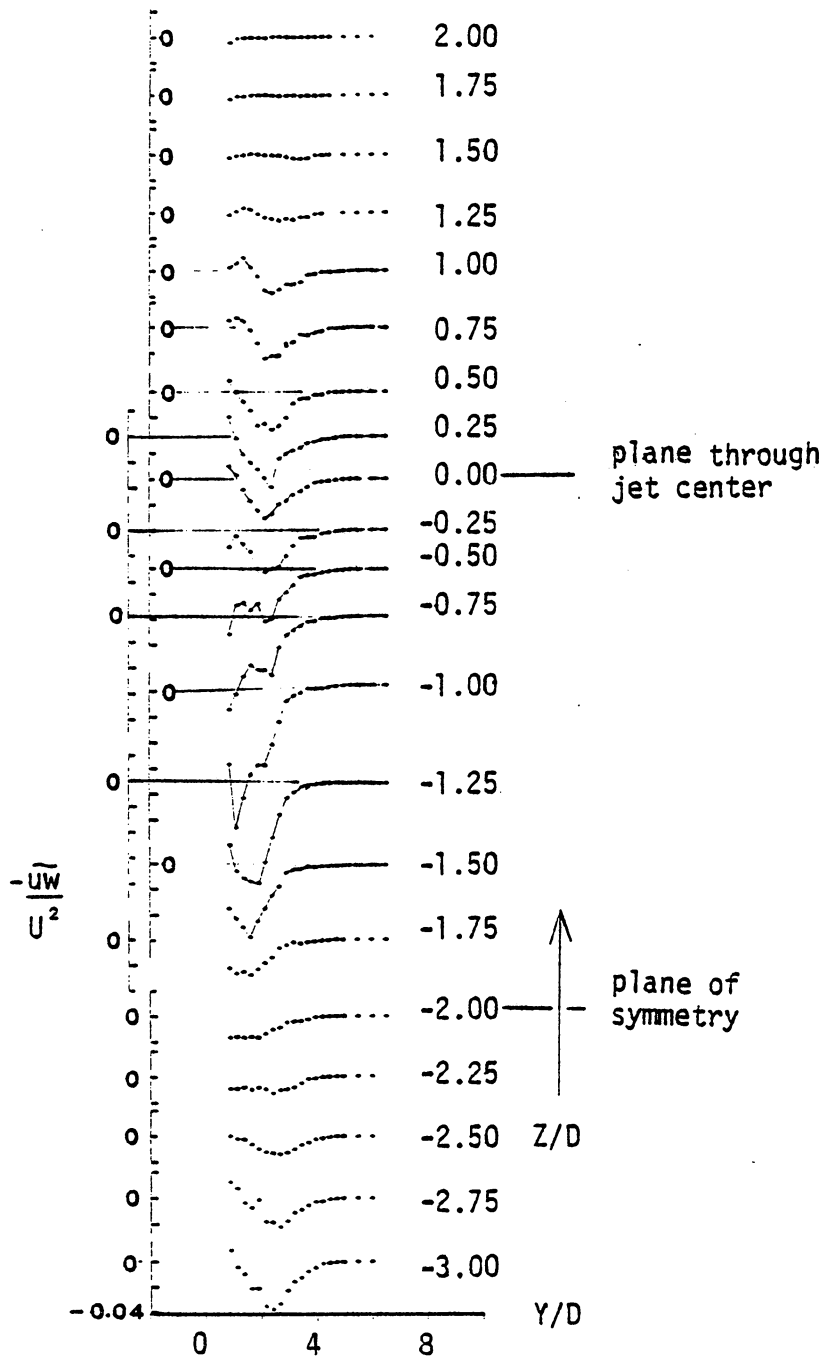


Fig.59 - Vertical distribution of the horizontal shear stress; side-by-side plume configuration; $X/D = 3$.

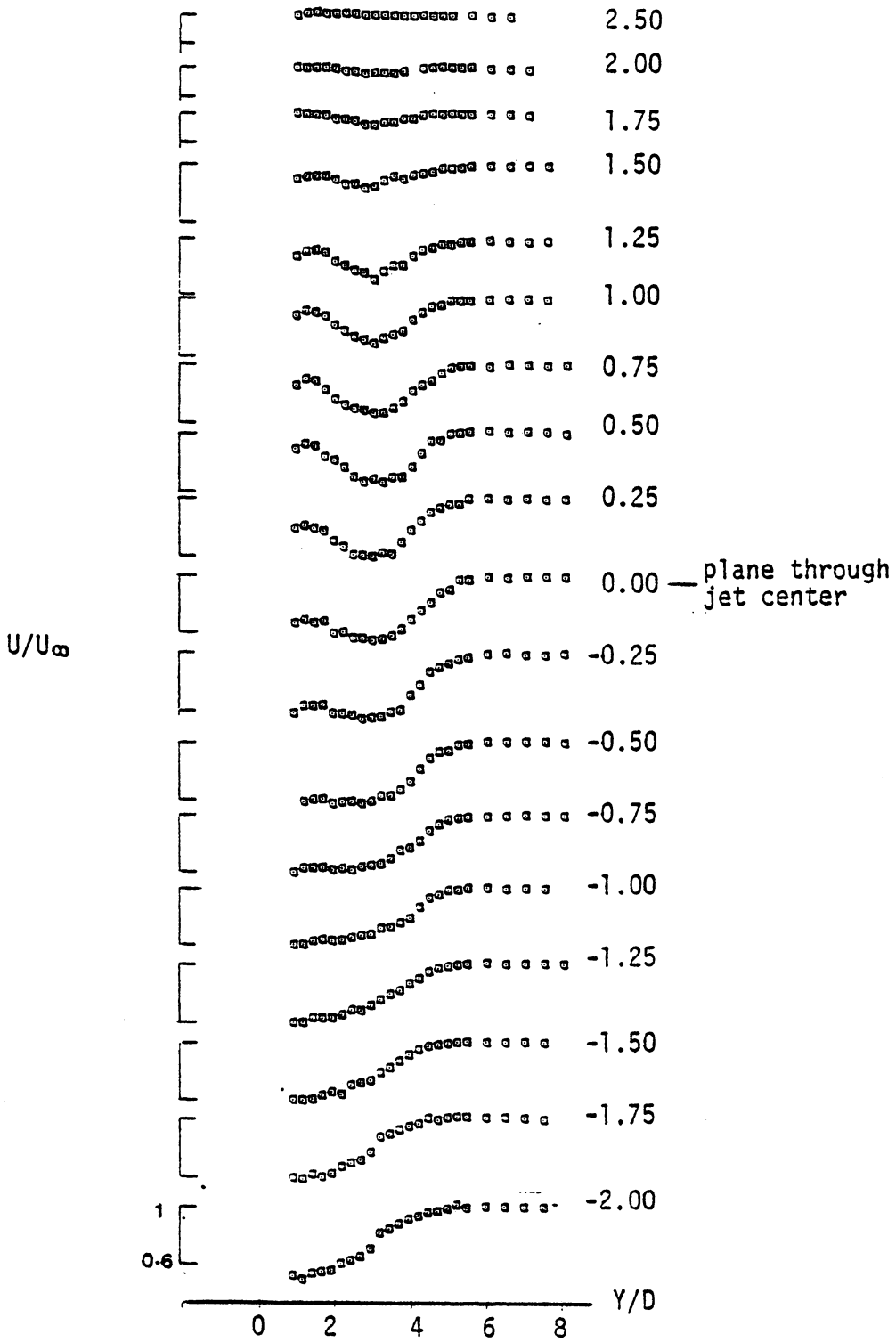


Fig. 60 - Vertical distribution of the axial mean velocity; side-by-side plume configuration; $X/D=10$

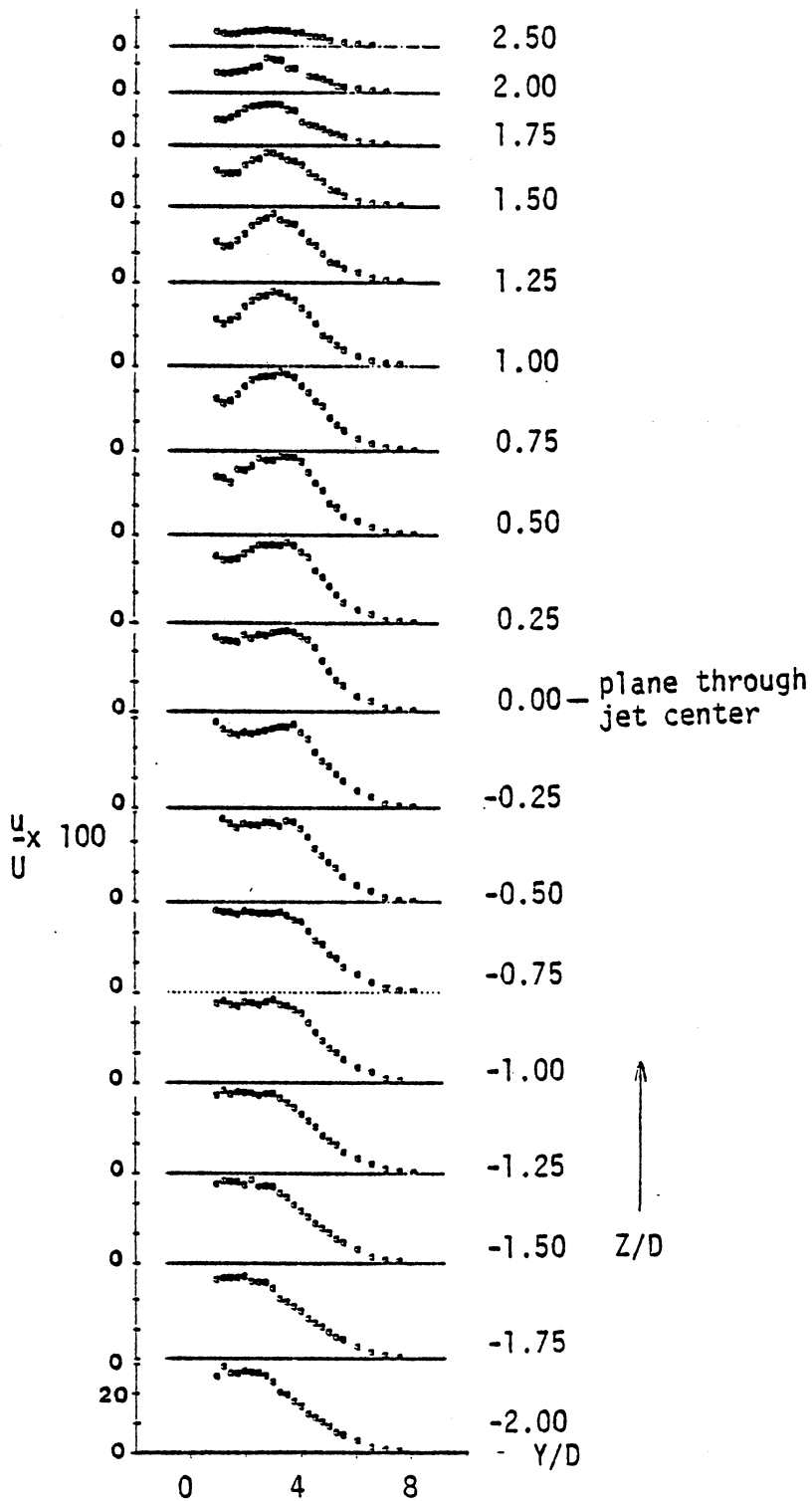


Fig.61 - Vertical distribution of axial turbulence intensity; side-by-side plume configuration; $X/D = 10$.

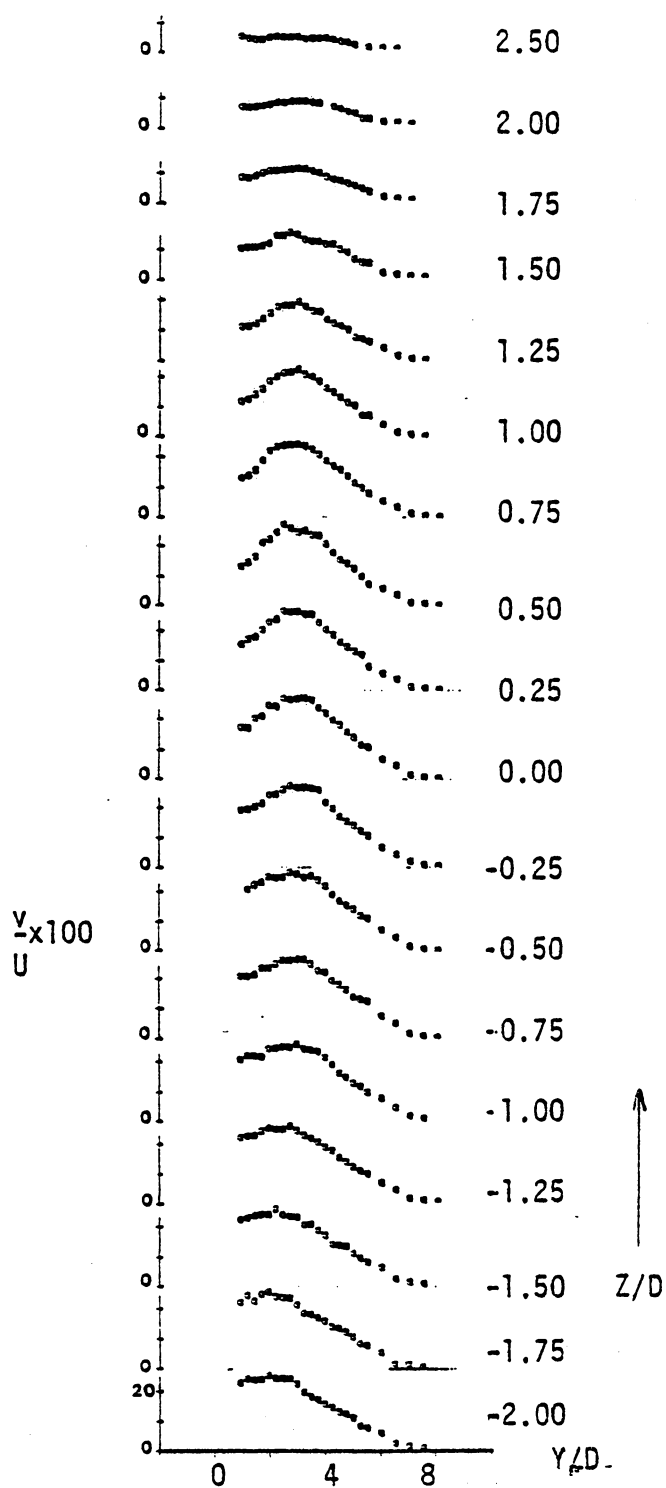


Fig. 62 - Vertical distribution of the vertical turbulence intensity; side-by-side plume configuration; $X/D = 10$.

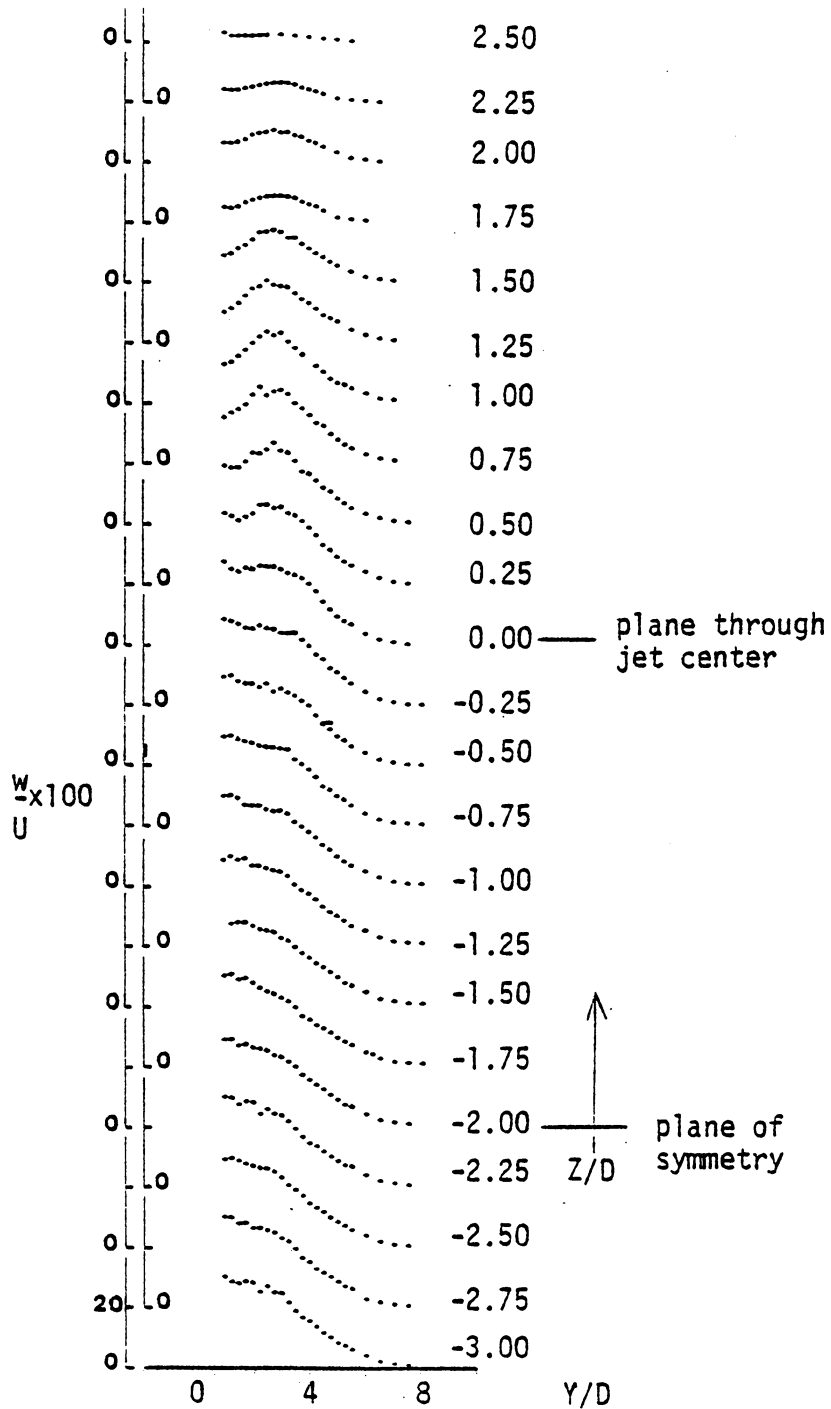


Fig. 63 - Vertical distribution of the horizontal turbulence intensity; side-by-side plume configuration; $X/D = 10$.

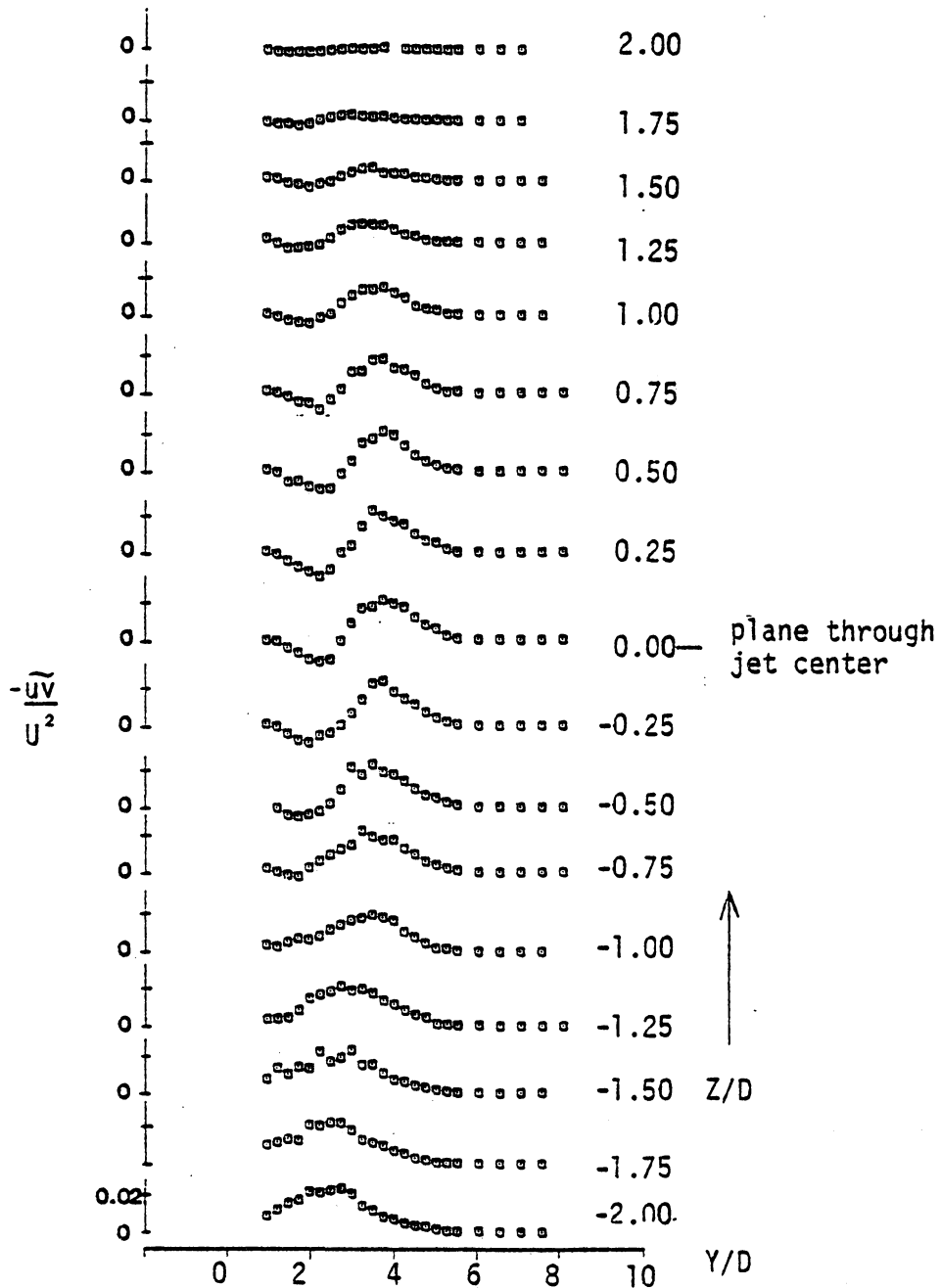


Fig. 64 - Vertical distribution of the vertical shear stress; side-by-side plume configuration; $X/D = 10$.

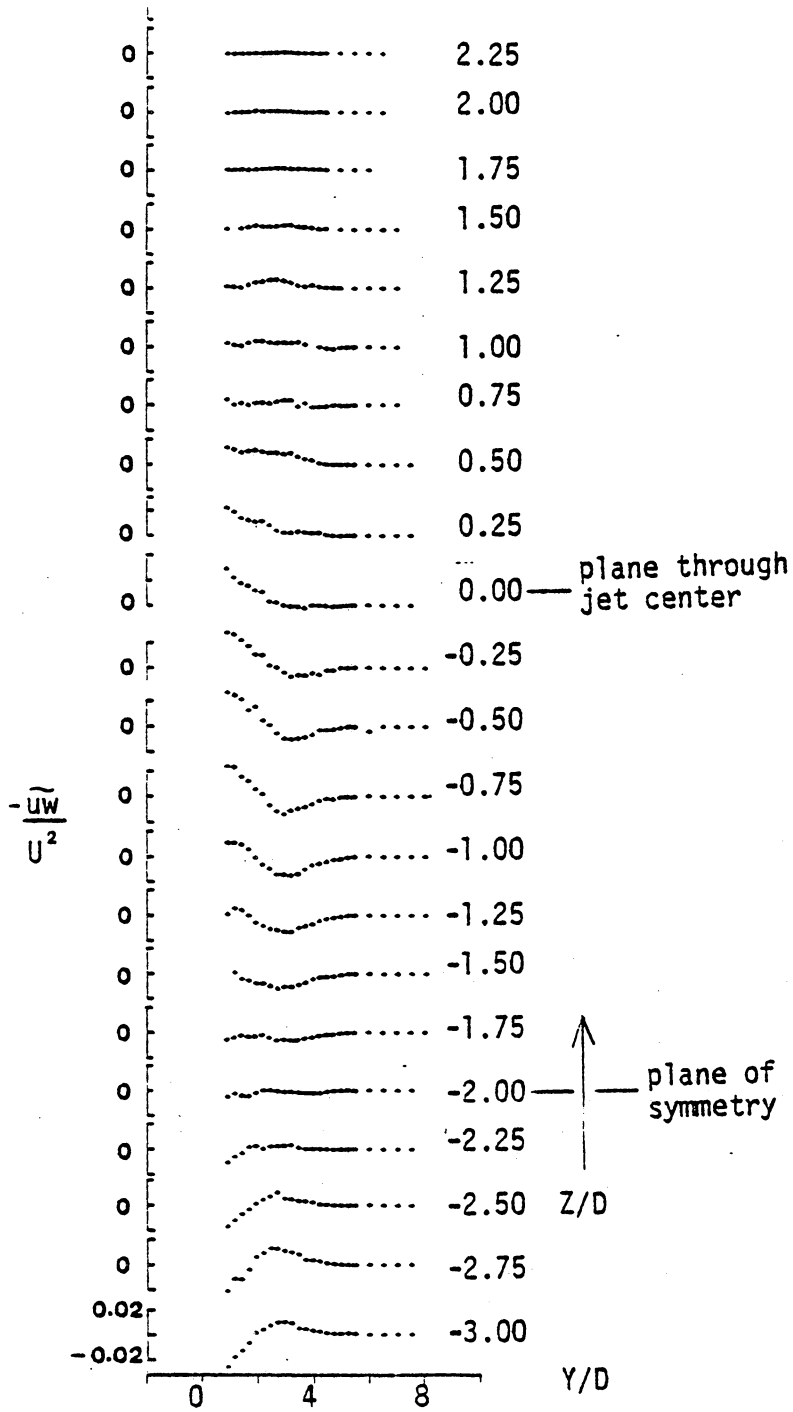


Fig. 65 - Vertical distribution of the horizontal shear stress; side-by-side plume configuration; $X/D = 10$.

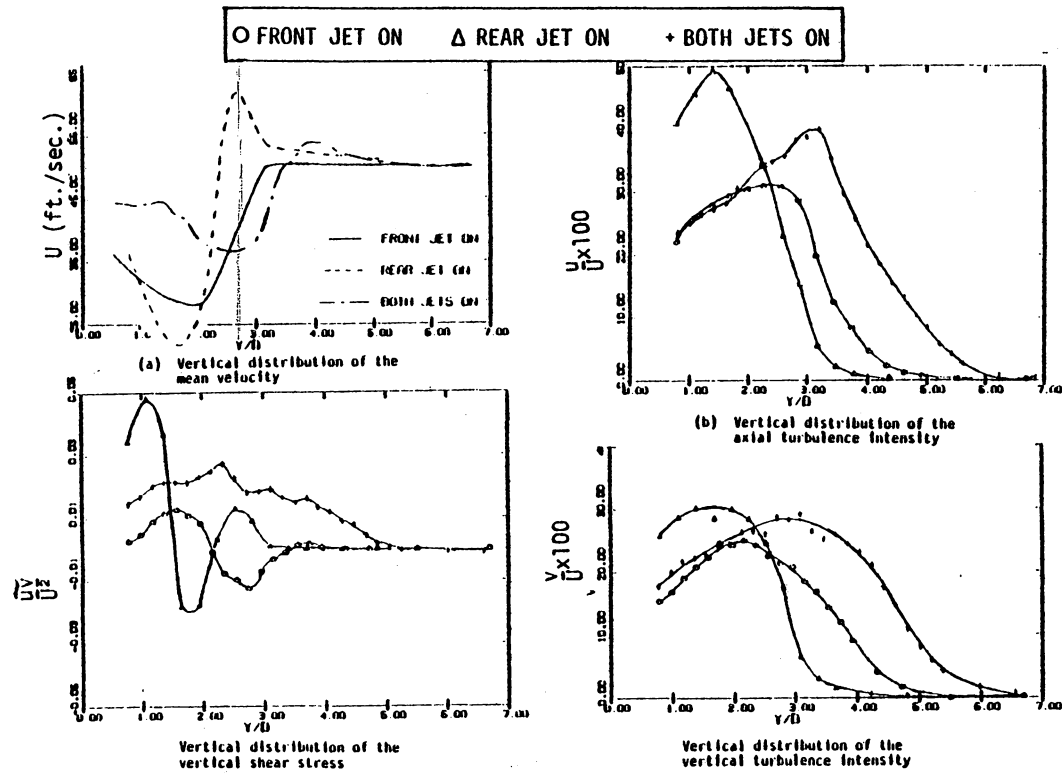


Fig.66- Flow properties in the plane of symmetry; tandem plume configuration; $X/D = 3$

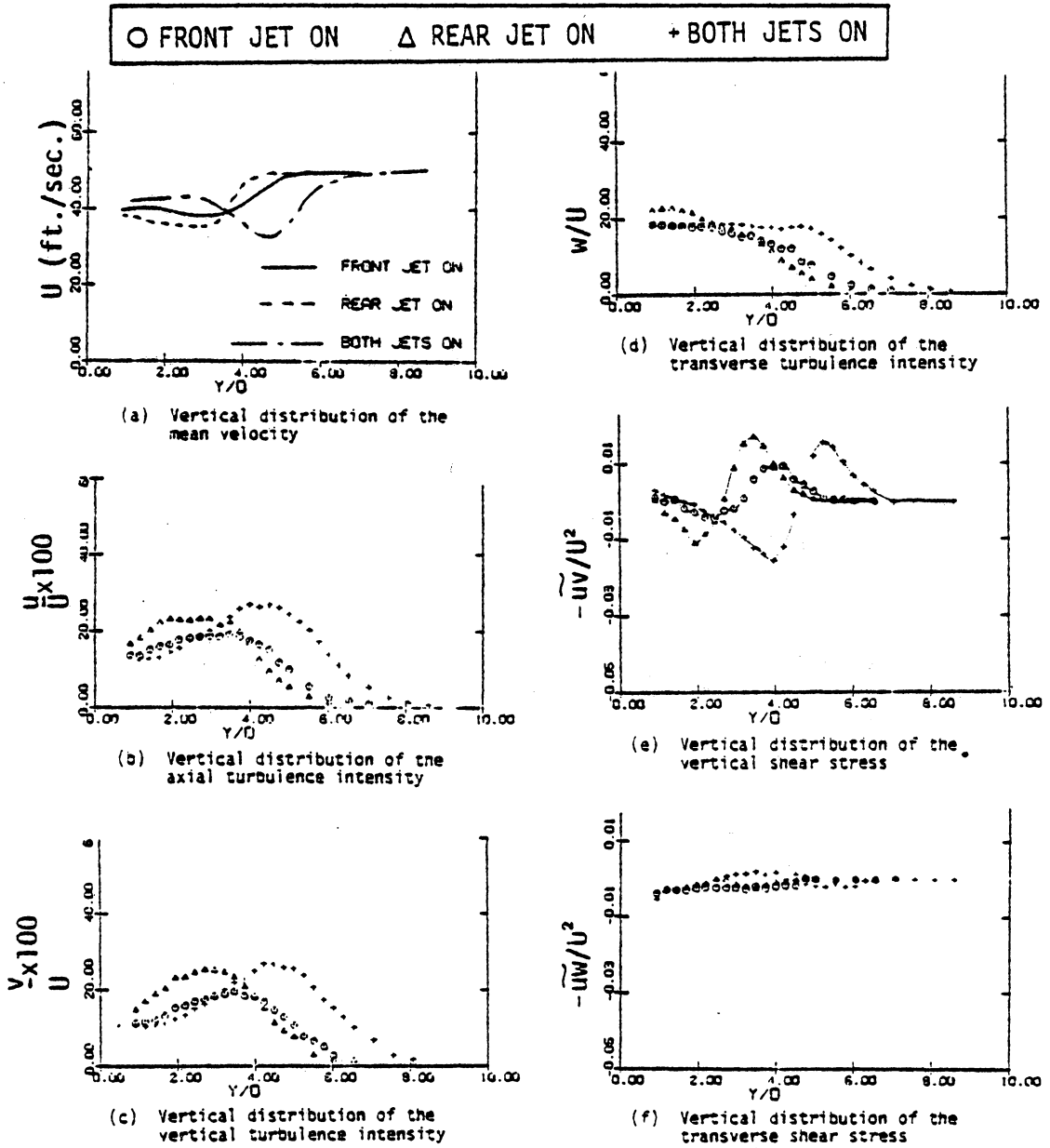


Fig.67 - Flow properties in the plane of symmetry; tandem plume configuration; $X/D = 10$.

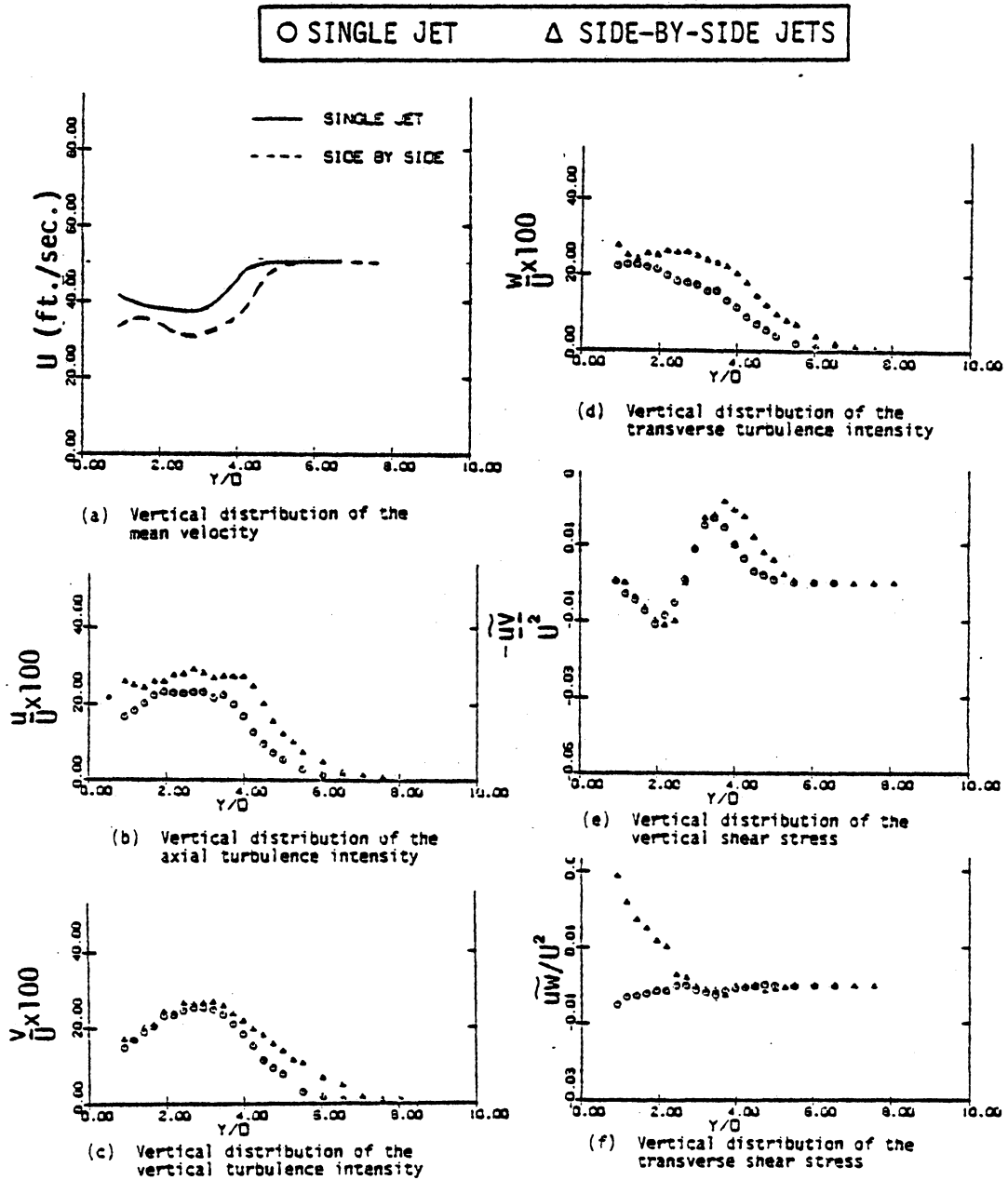


Fig. 68 - Flow properties in the vertical plane through one of the jet centers; side-by-side plume configuration; $X/D = 10$

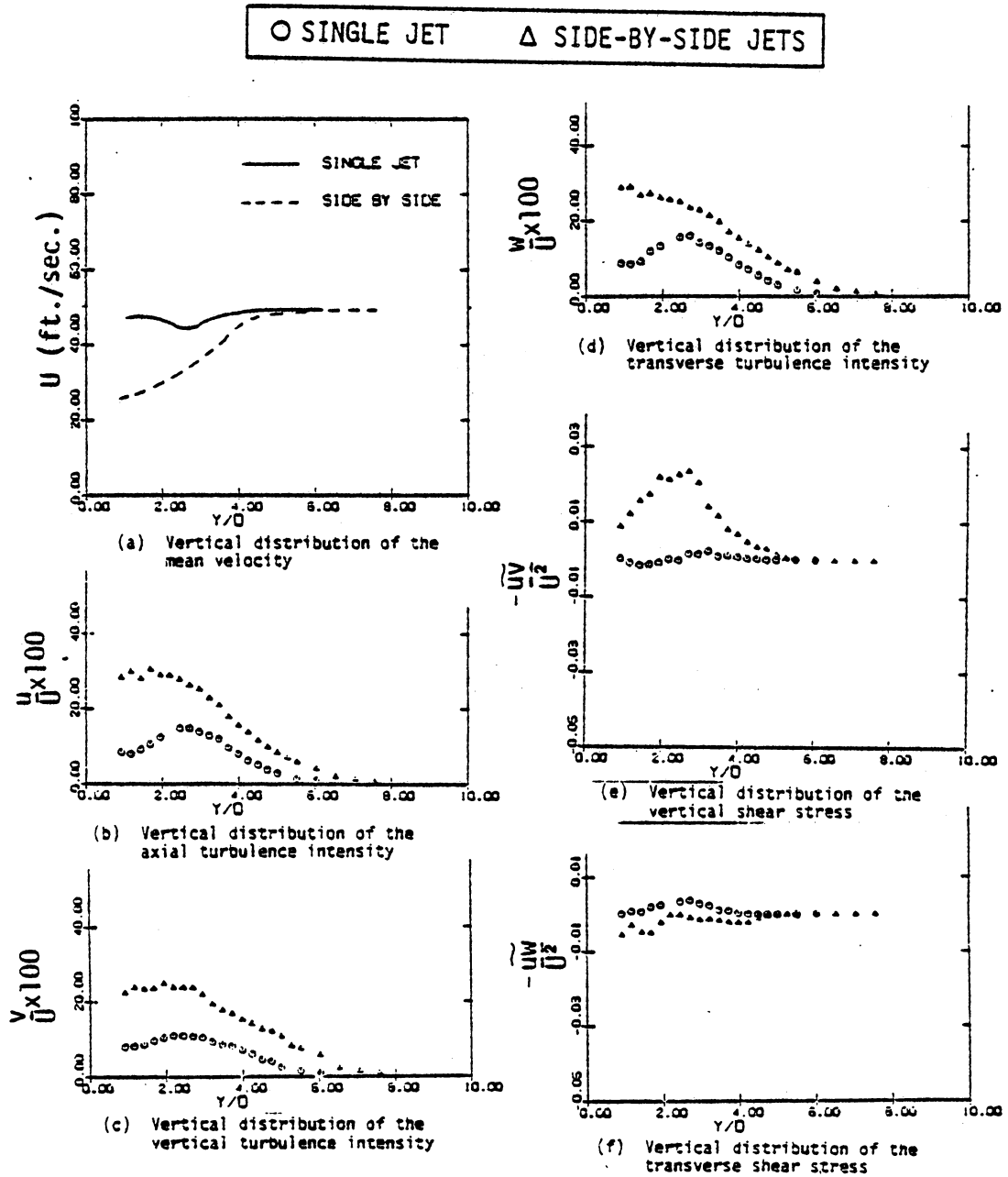


Fig.69 - Flow properties in the vertical plane of symmetry of the side-by-side plume configuration

X/D = 10

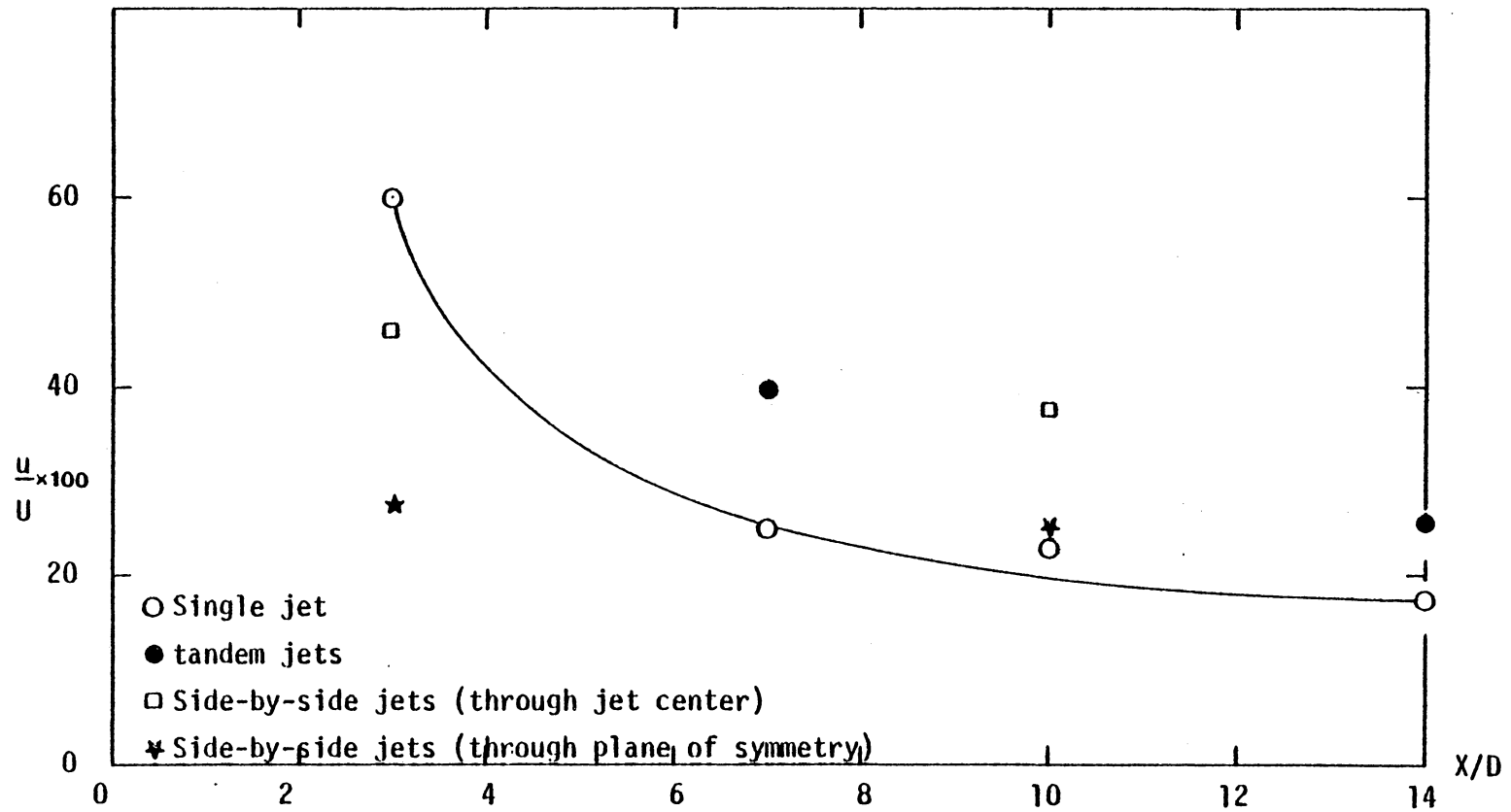


Fig.70 - Axial variation of maximum axial turbulence intensity

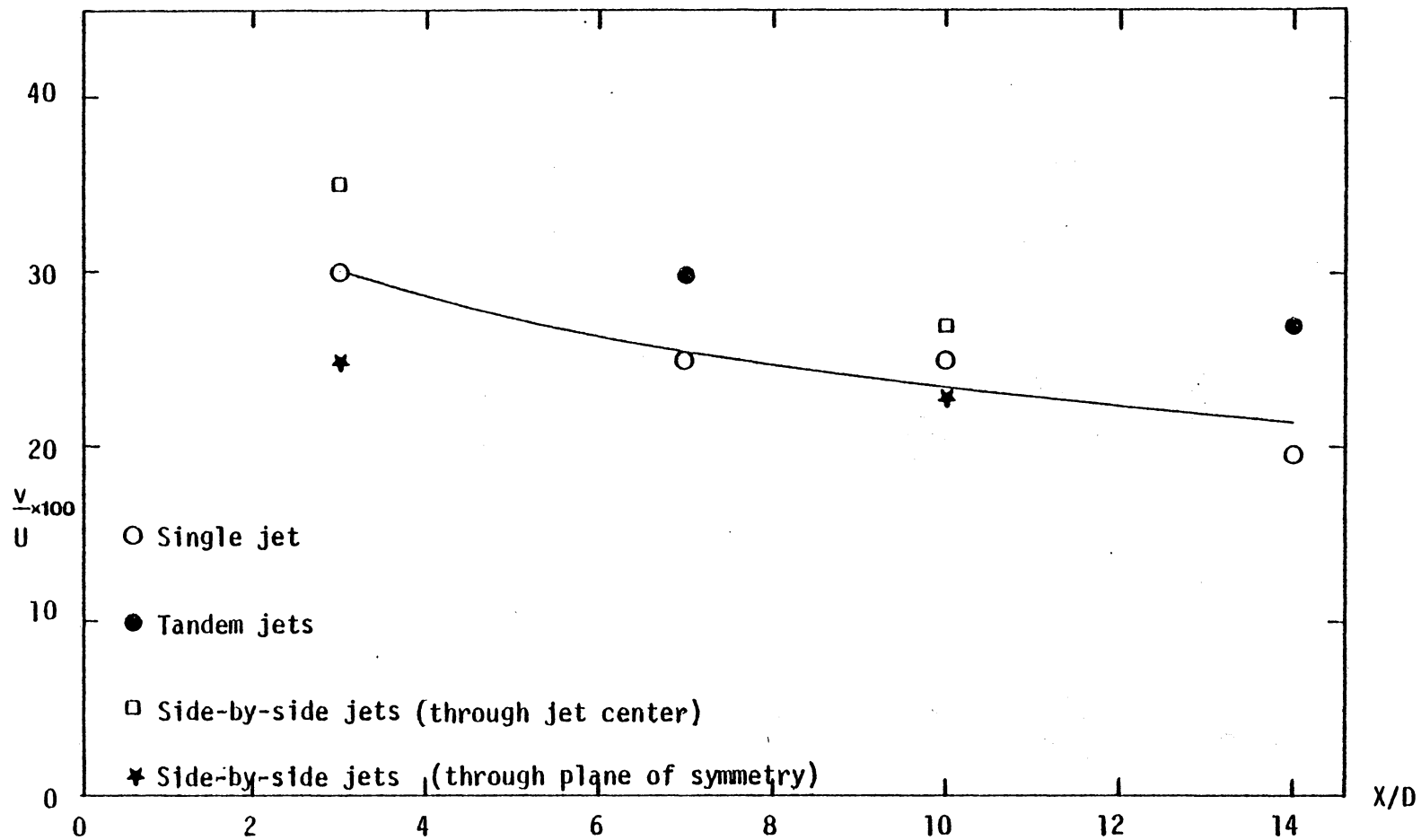


Fig.71 - Axial variation of maximum vertical turbulence intensity

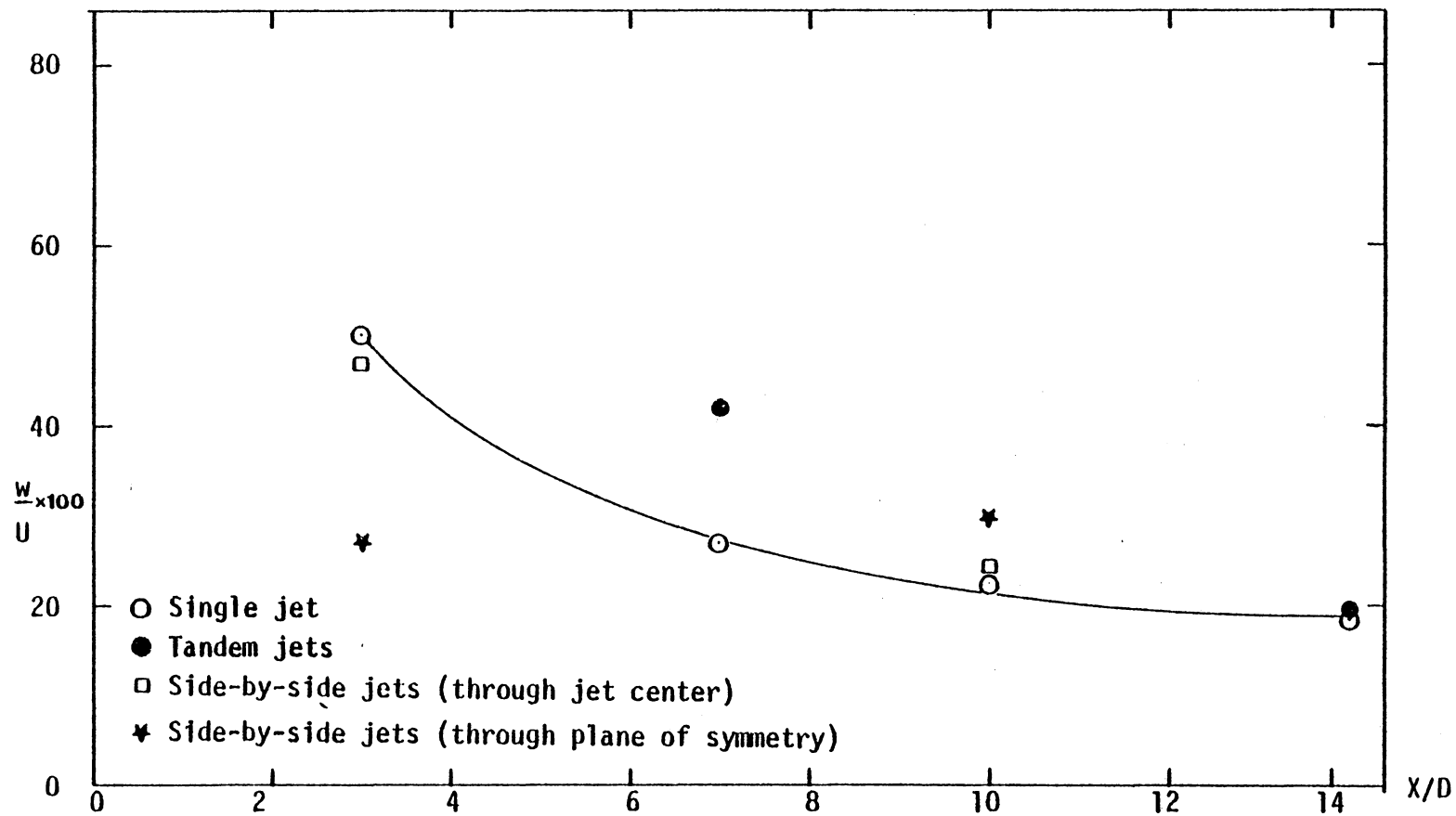


Fig.72 - Axial variation of maximum transverse turbulence intensity

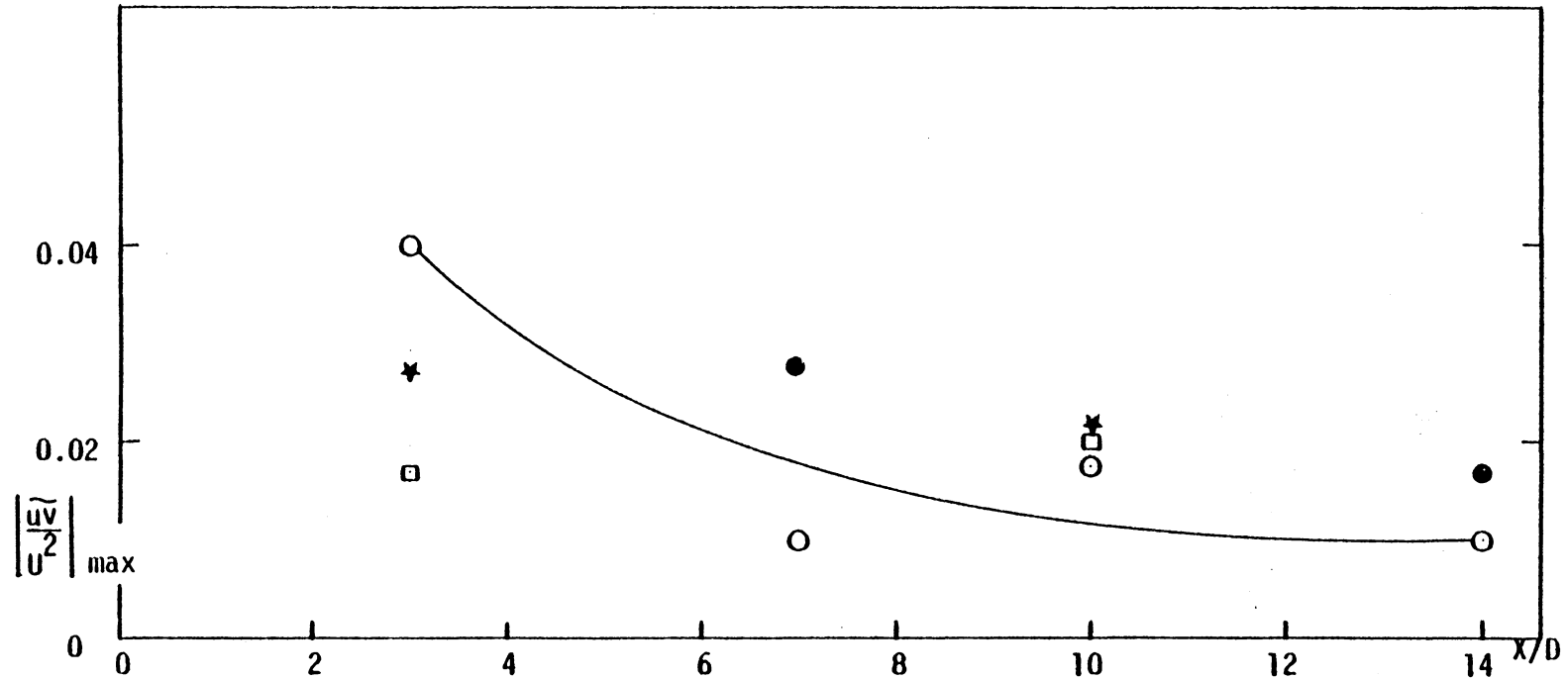


Fig.73 - Axial variation of maximum vertical shear stress

- Single jet
- Tandem jets
- Side-by-side jets (through jet center)
- ★ Side-by-side jets (through plane of symmetry)

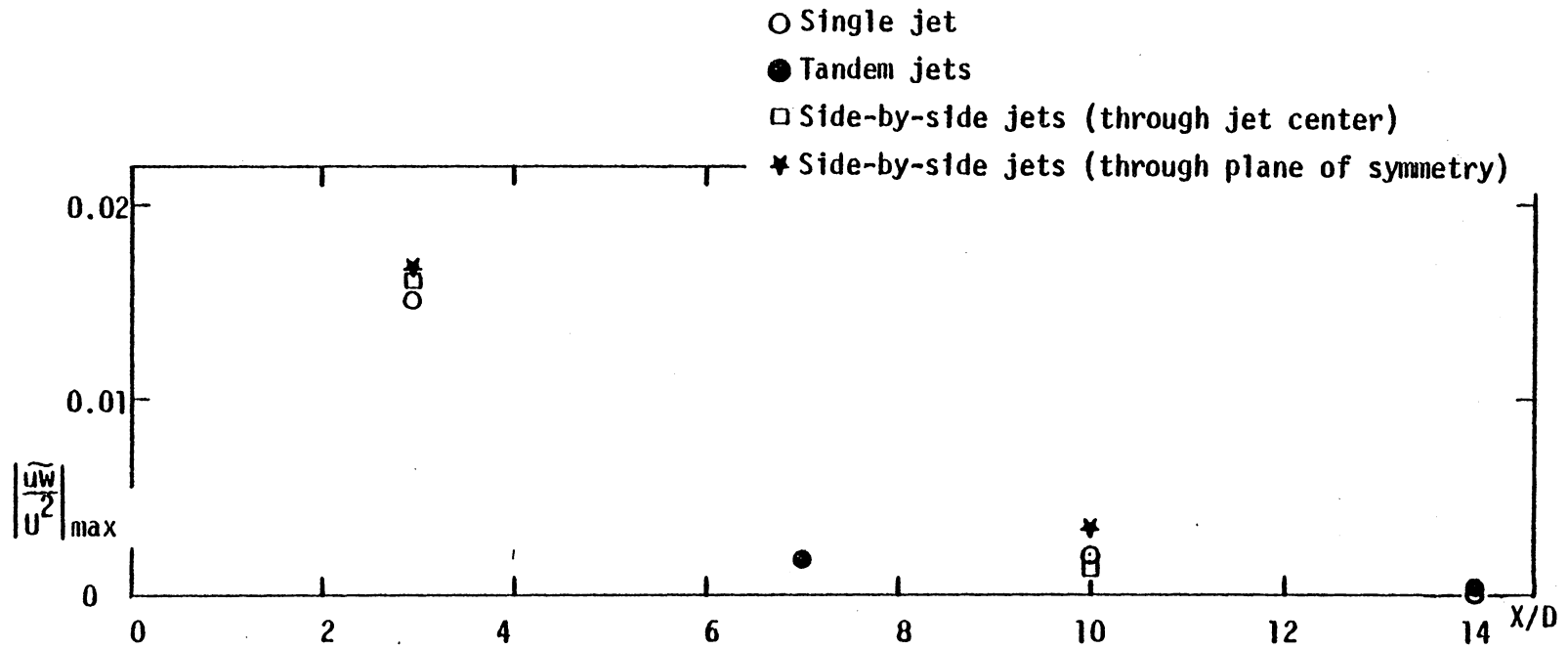


Fig.74 - Axial variation of maximum horizontal shear stress

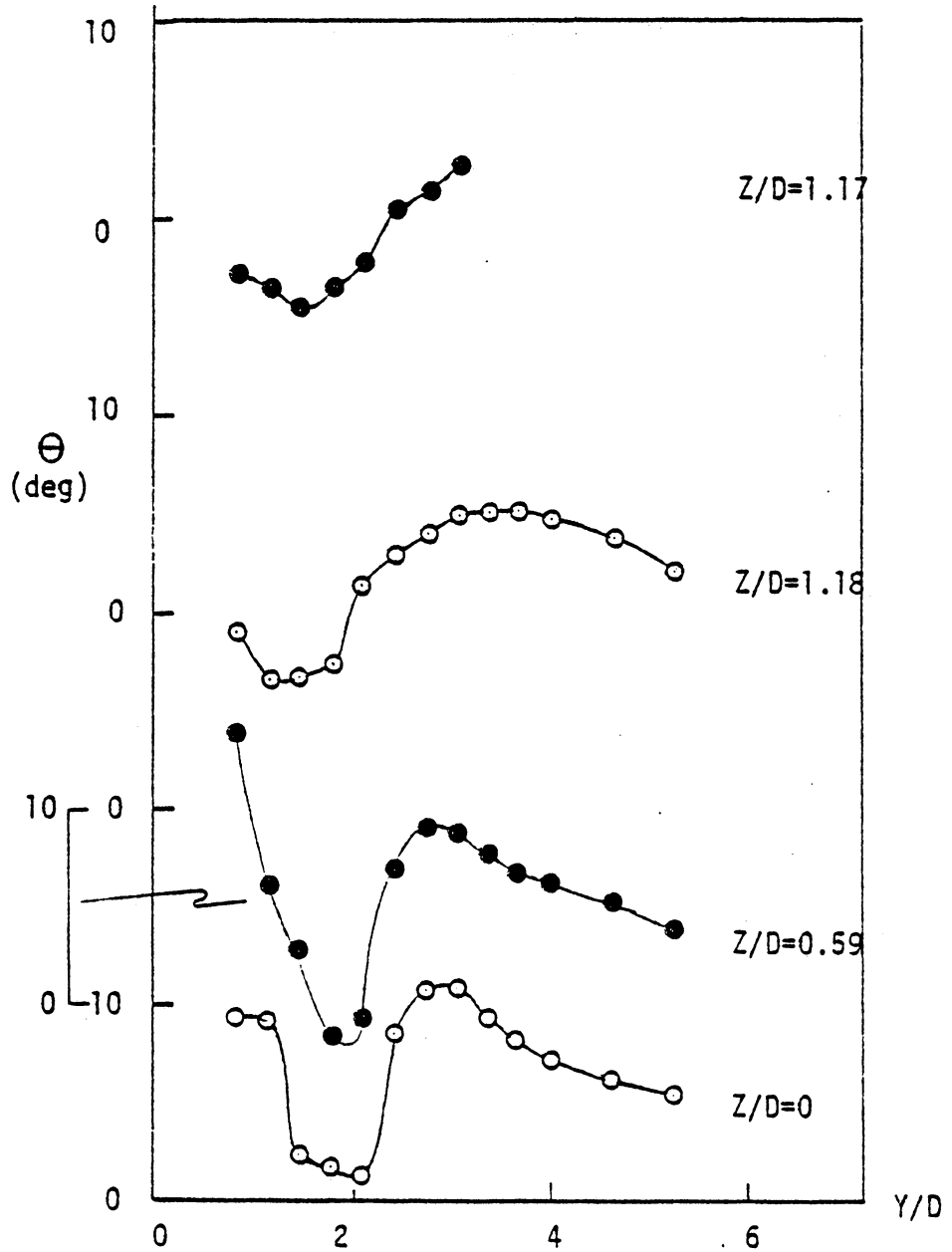


Fig.75 - Flow angles in the vertical plane
single jet; $X/D = 3$

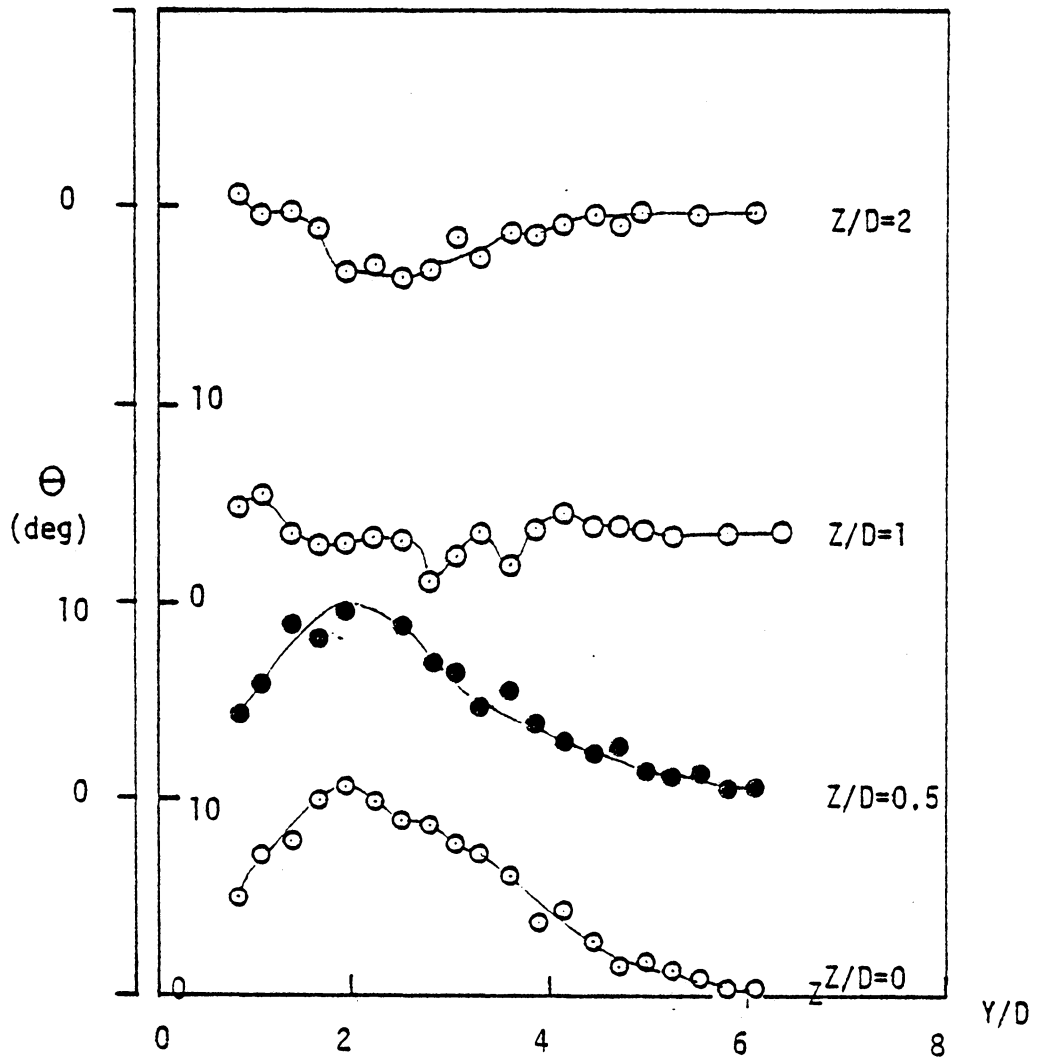


Fig.76 - Flow angles in the vertical plane
single jet; $X/D = 10$.

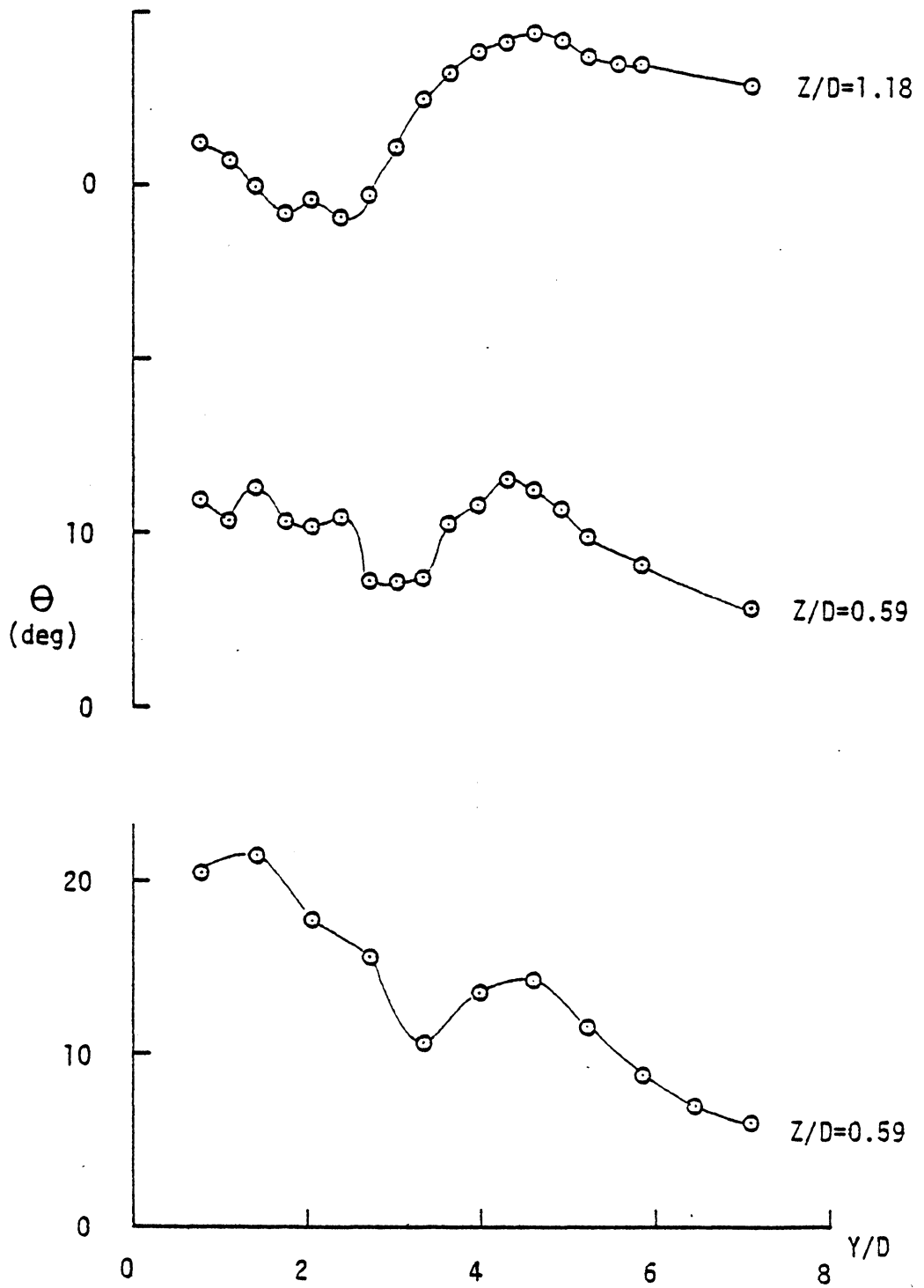


Fig. 77 - Flow angles in the vertical plane
tandem jets; $X/D=3$

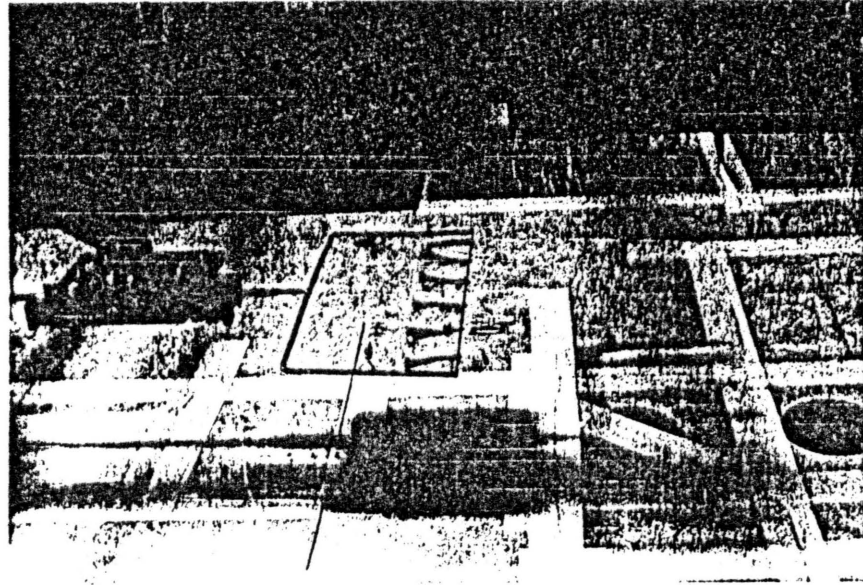


Fig. 78 - Tuft photograph showing positive and negative flow angles; single jet; $X/D = 8; Y/D=3$

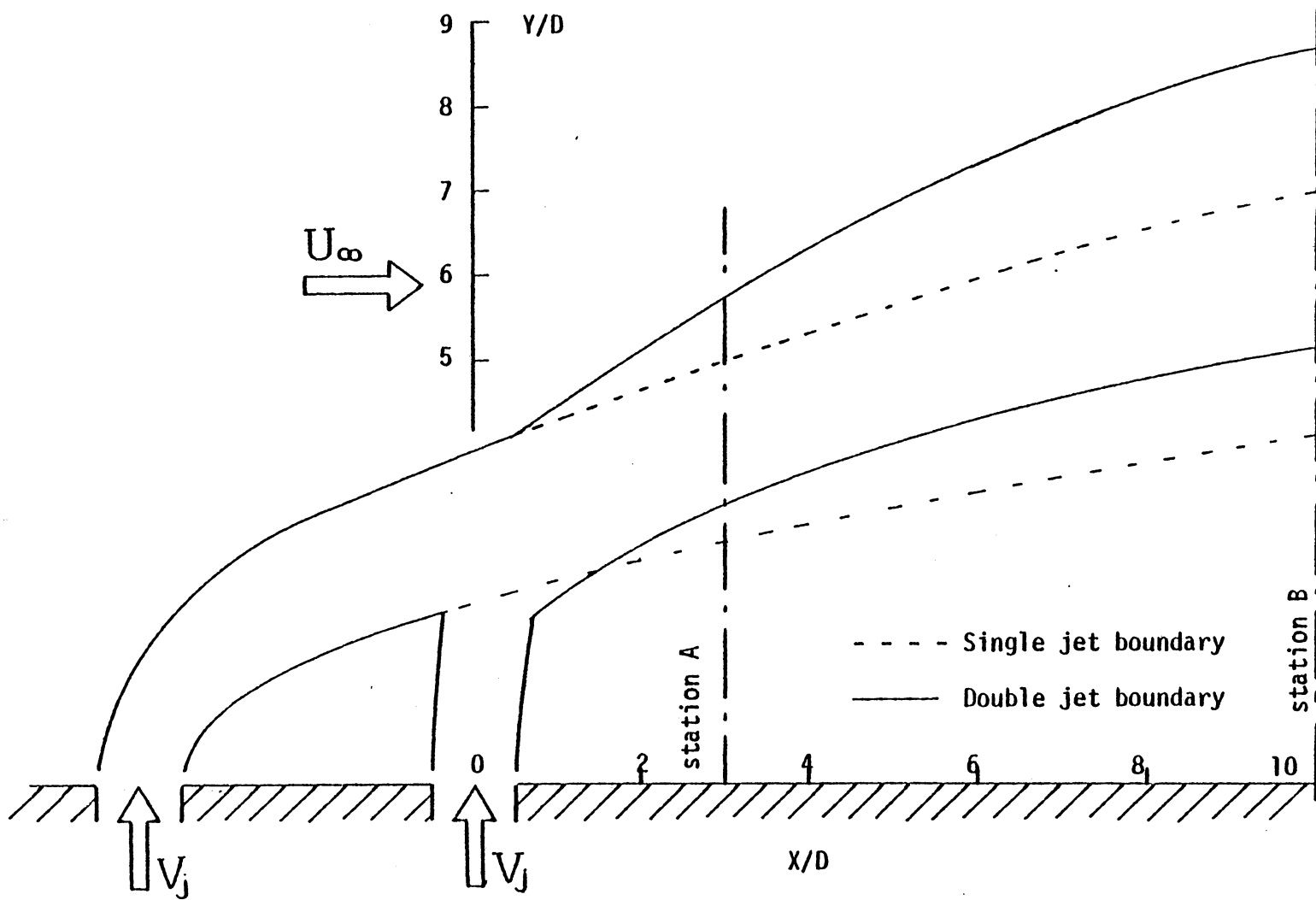


Fig. 79 - Pictorial representation of the jets in tandem configuration reconstructed from flow visualization and turbulence measurements.

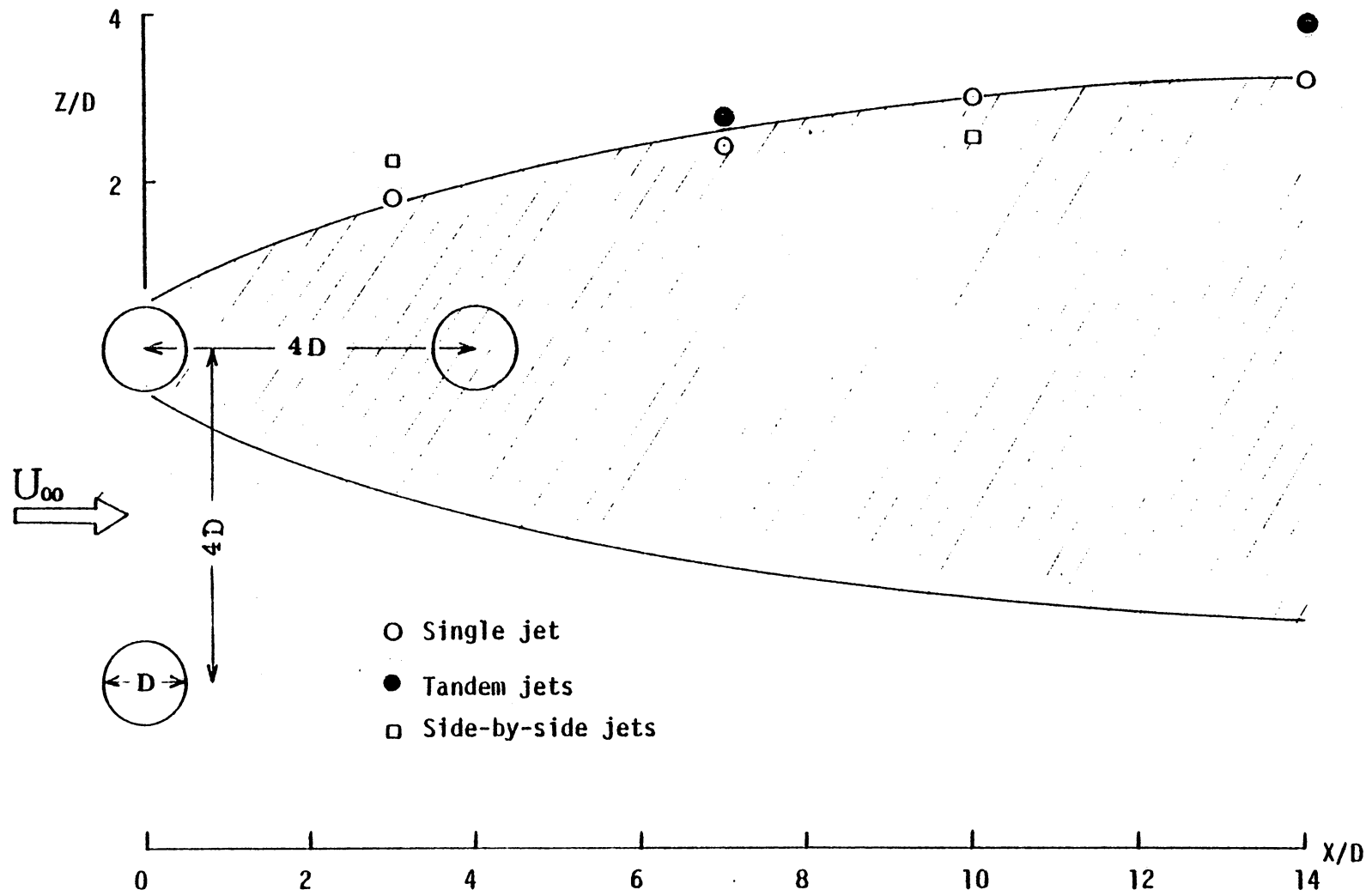


Fig.80 - Lateral spread of the jets in the three configurations studied

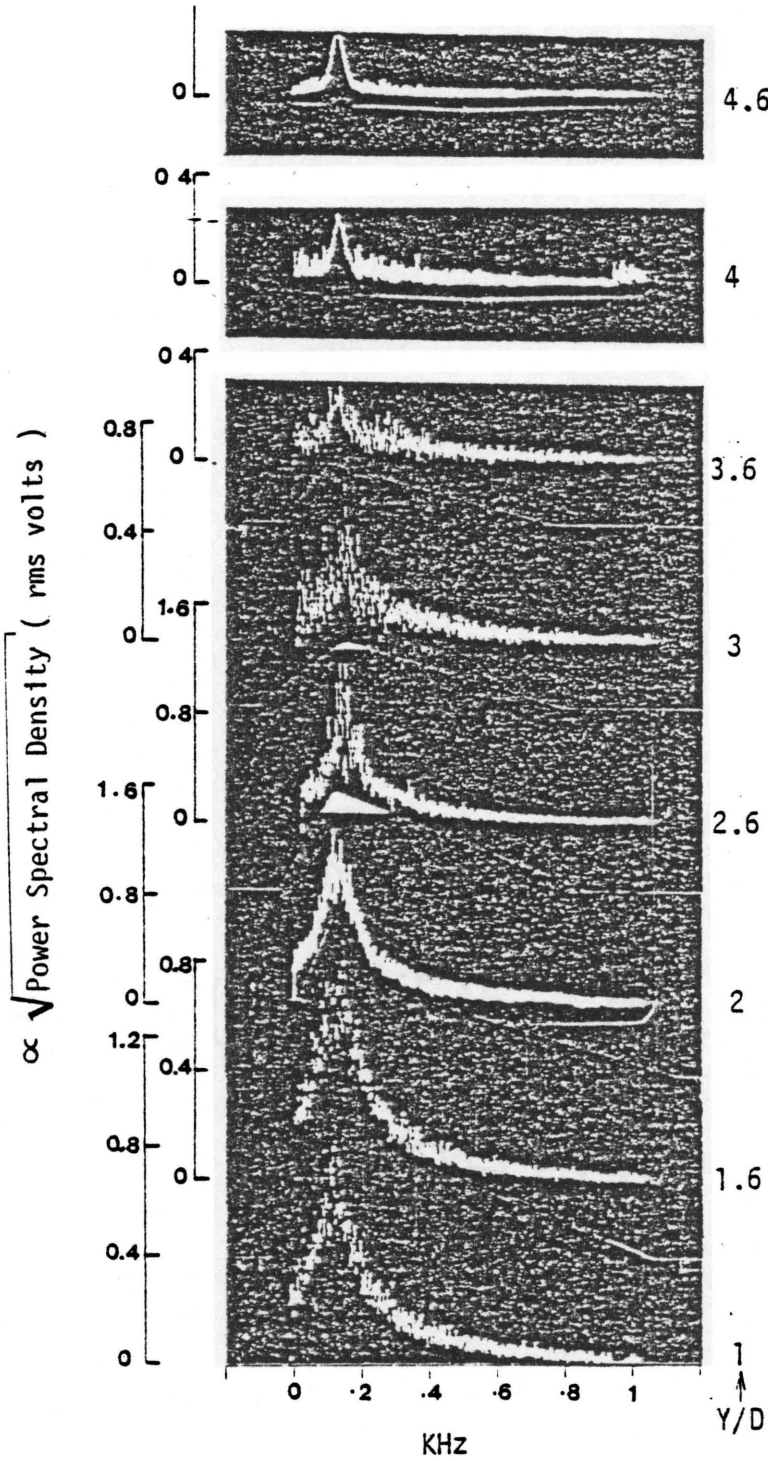


Fig.81 - Power spectra for a single jet in the plane of symmetry; $X/D=3$.

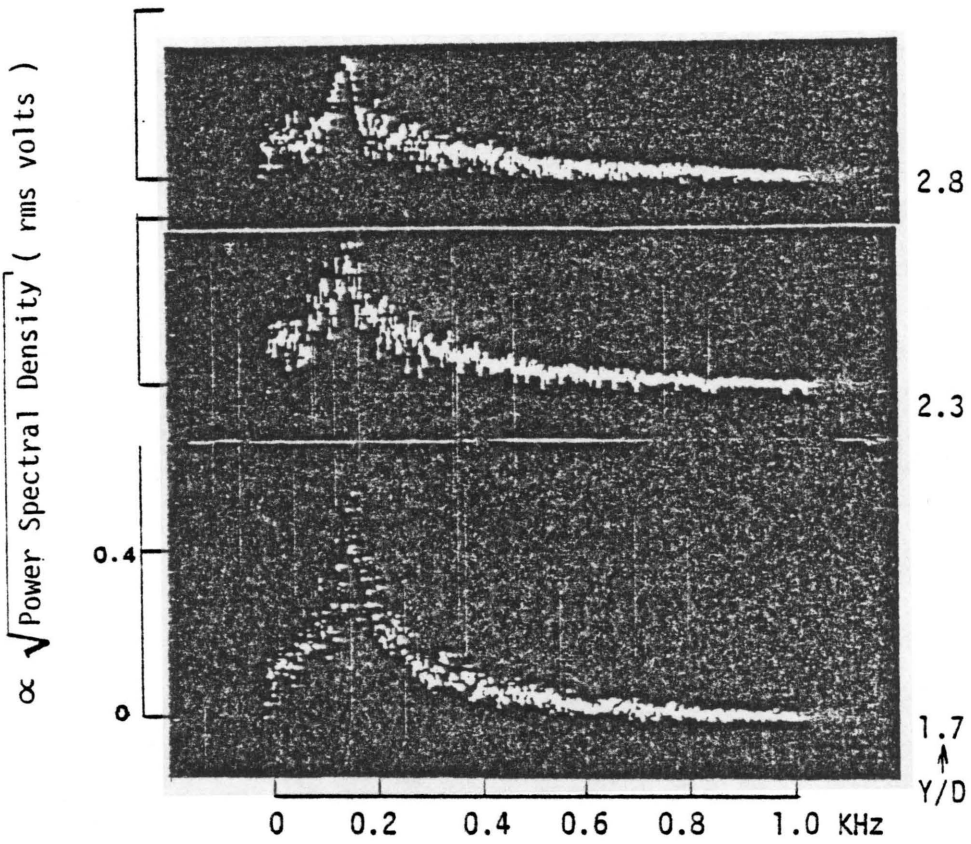


Fig.82 - Power spectra for a single jet;
 2D to the left of the plane of
 symmetry; $X/D = 3$.

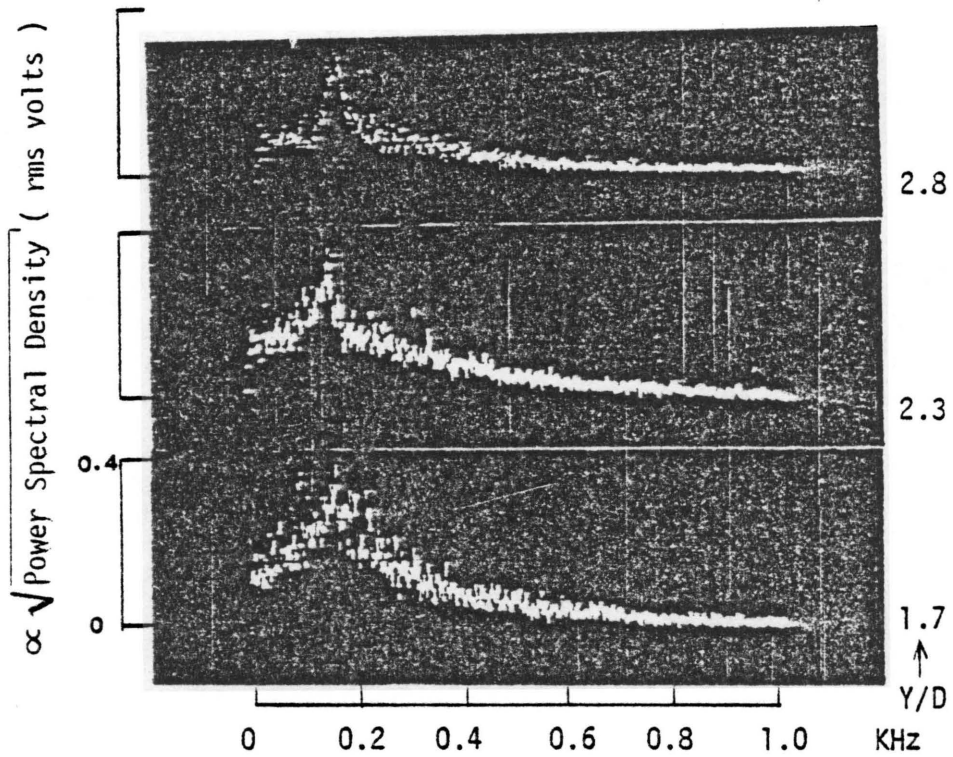


Fig.a3- Power spectra of the side-by-side jets
in the plane of symmetry($Z/D=-2$)
 $X/D = 3$.

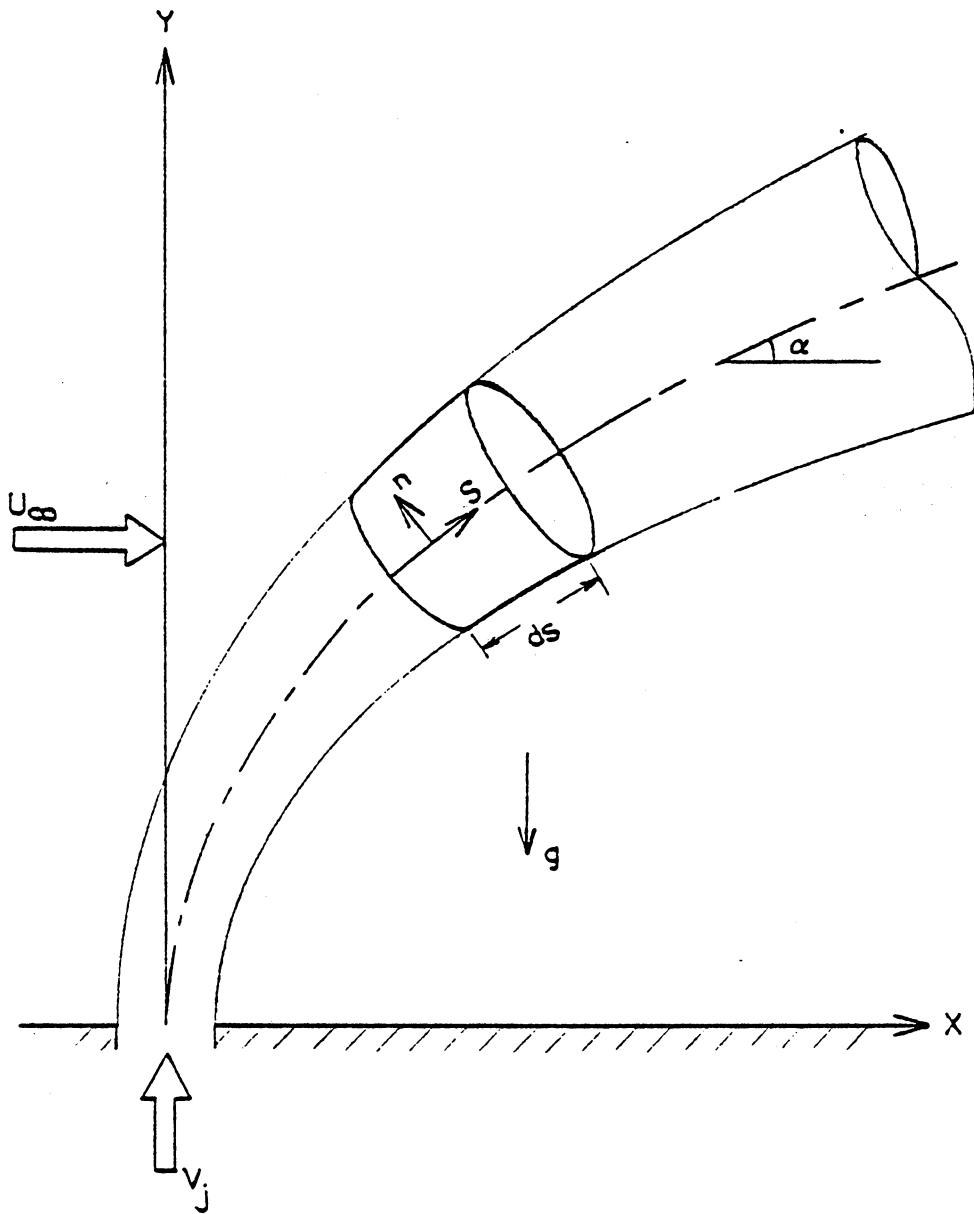


Fig. 84 - Cartesian and natural coordinate systems

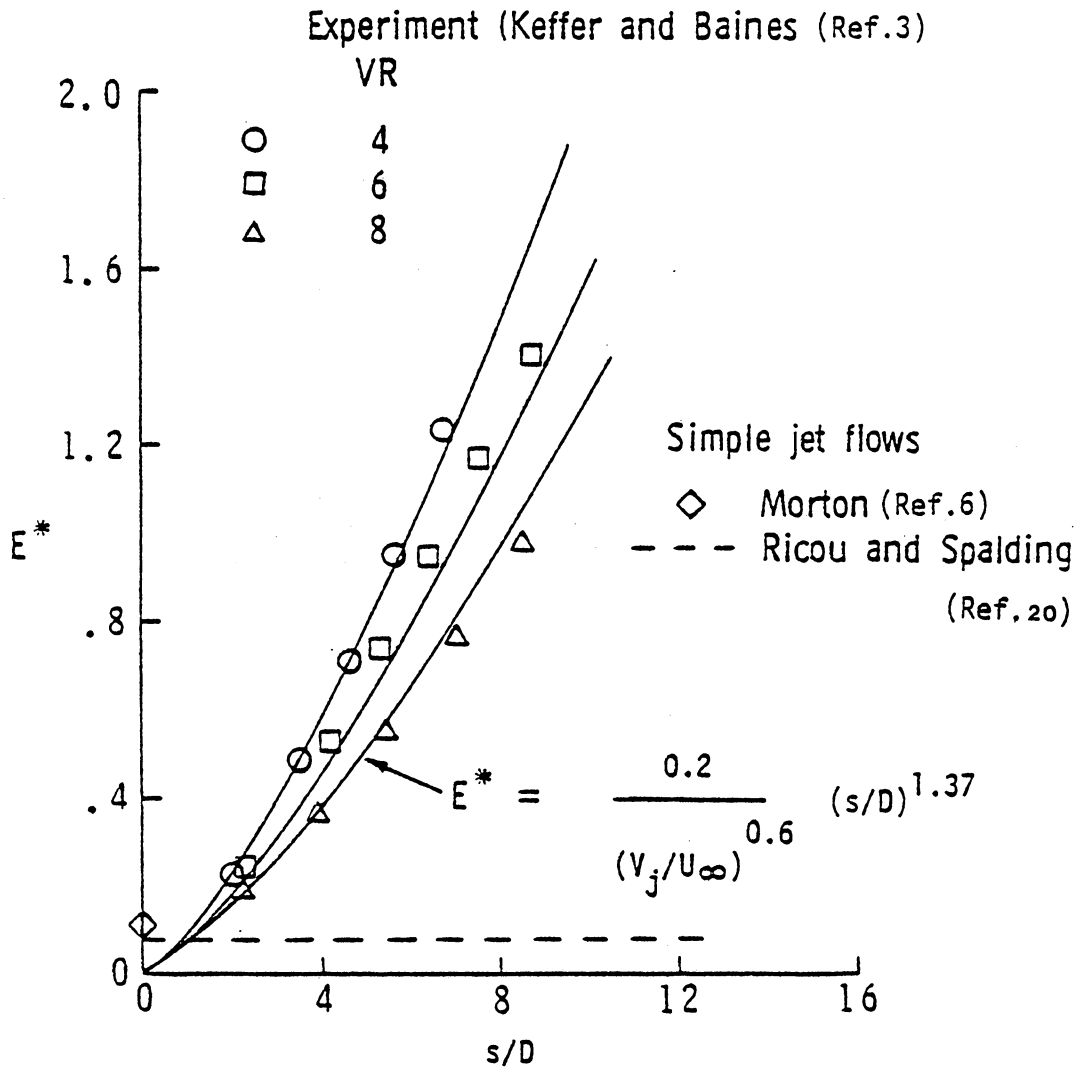


Figure-95 Entrainment coefficient as a function of position along axis of isothermal air jet; $\alpha_i = 90^\circ$.

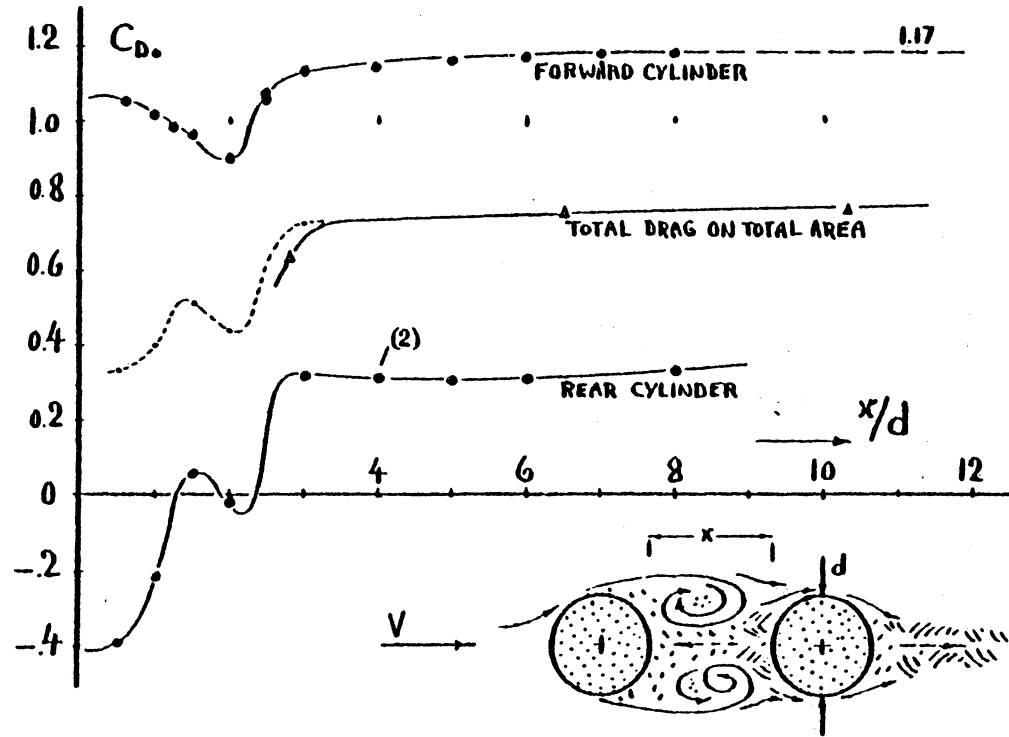


Fig.86 Drag coefficient of two circular cylinders one placed behind the other. From Ref.22

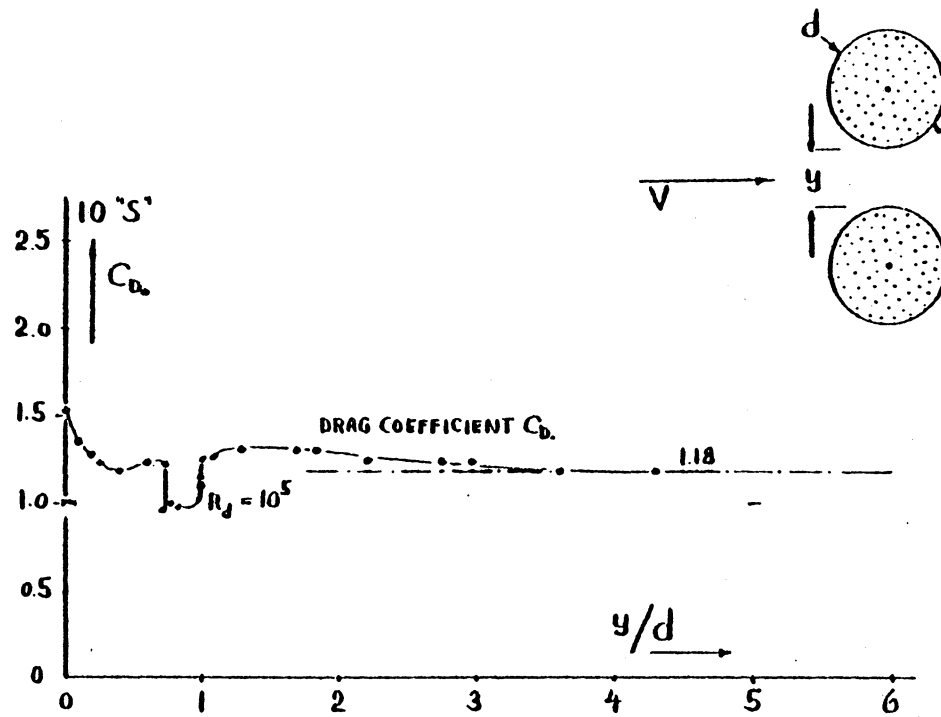


Fig.87 Drag coefficient of a pair of circular cylinders placed side-by-side. From Ref.22

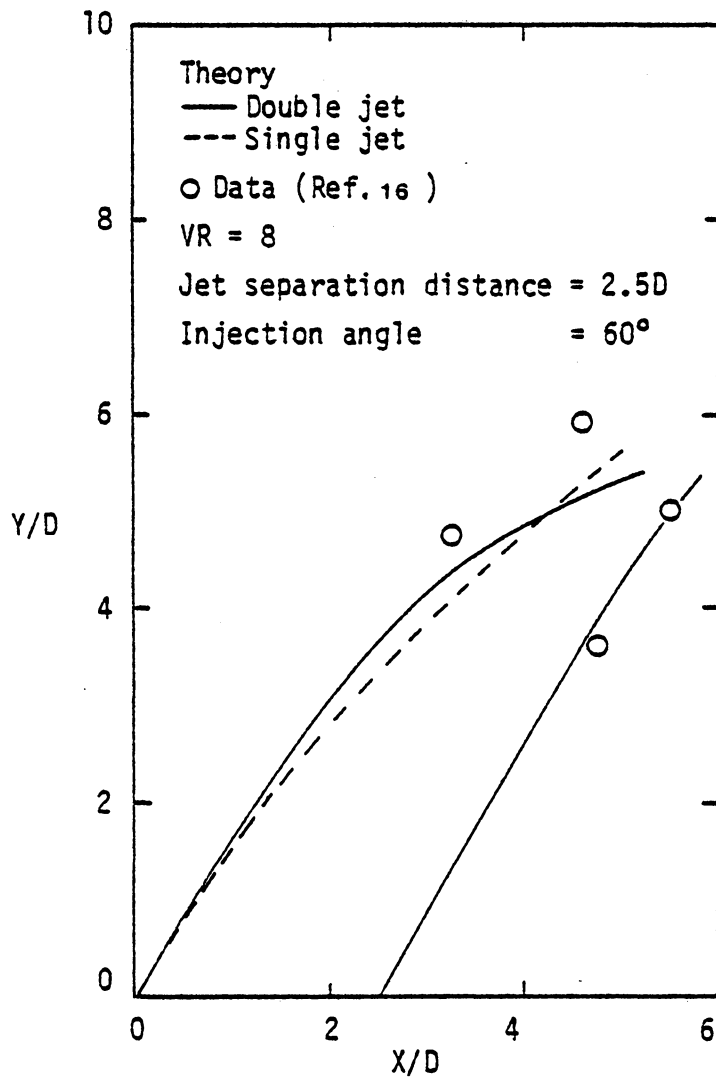


Fig. 88 Single and Tandem Jet Trajectories

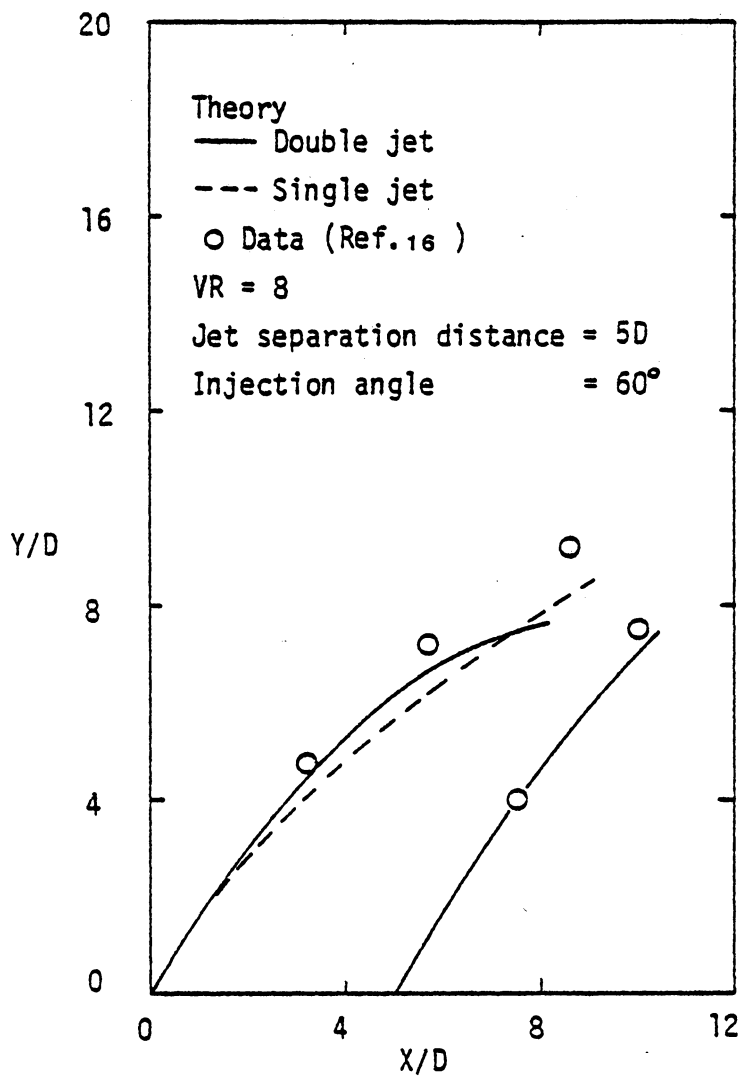


Fig.89 Single and Tandem Jet Trajectories

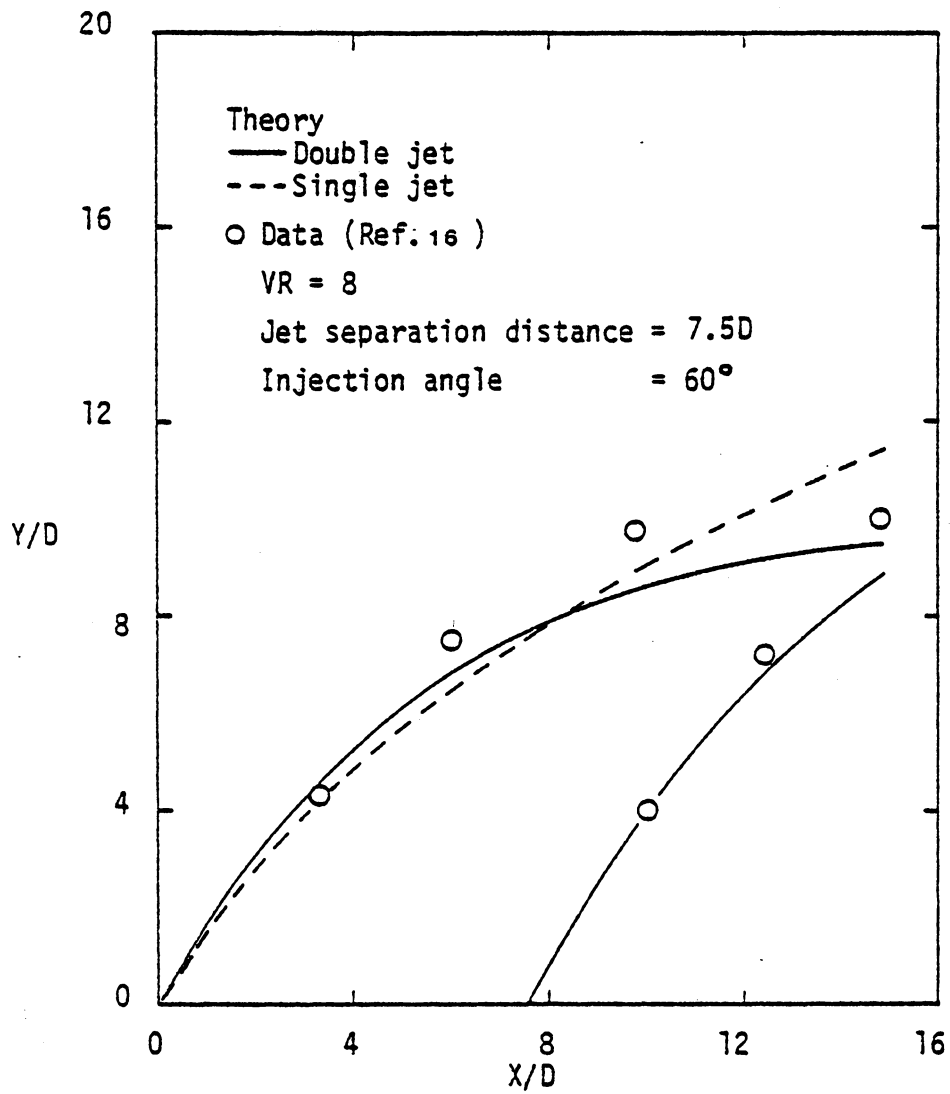


Fig.90 Single and Tandem Jet Trajectories.

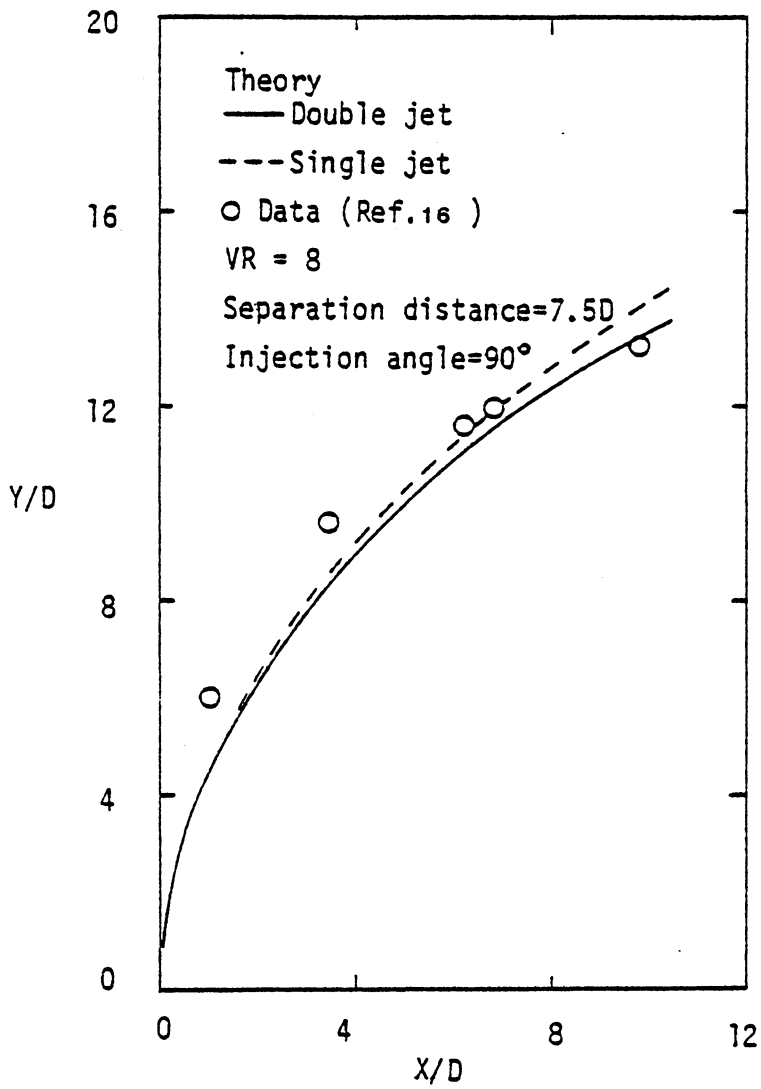


Fig.91 Trajectories for Single and Side-by-side Jets

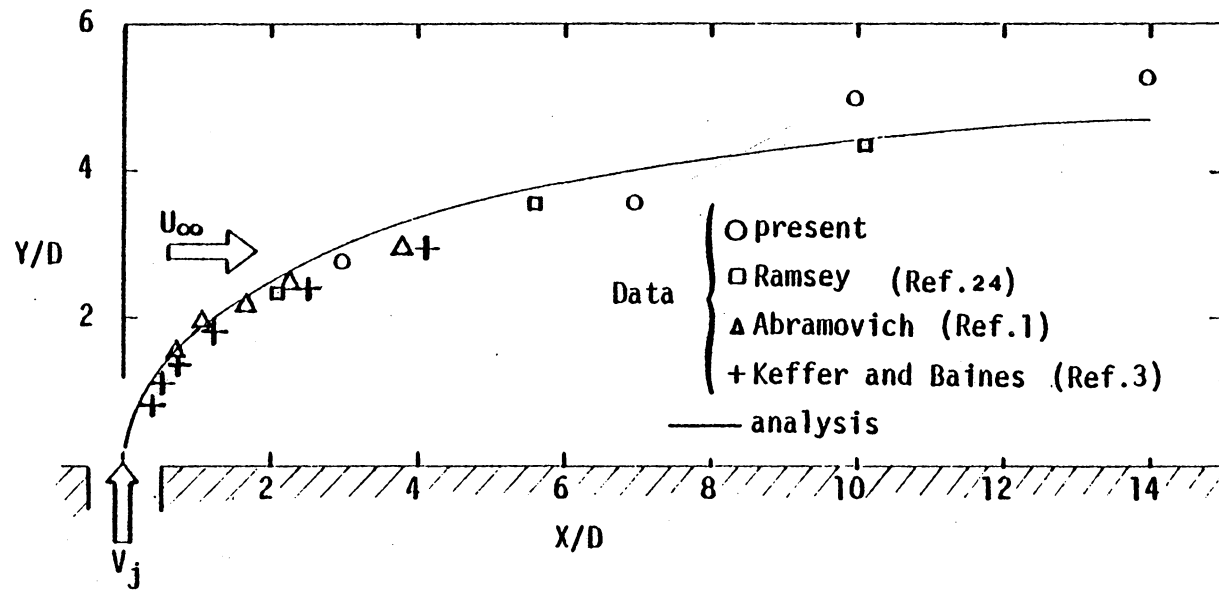


Fig.92 - Comparison of the data and the present analysis for $VR = 2$.

**The vita has been removed from
the scanned document**

EXPERIMENTAL AND ANALYTICAL
INVESTIGATION OF MULTIPLE JETS IN A CROSS-FLOW

by

Kakkattukuzhy Mathai Isaac

(ABSTRACT)

Extensive measurements using hot-wire anemometry were carried out for single jet, tandem jets, and side-by-side jets for a velocity ratio of 2, and a jet spacing of 4 for the latter two cases. The measurements yielded axial mean velocity, turbulence intensities, and Reynolds stresses for four downstream stations for the single jet and two downstream stations for the double jet. A preliminary study of the one-dimensional frequency spectra and flow visualization using a tuft wire were also performed. An analytical study using a momentum-integral approach was also carried out in order to predict the gross jet properties such as the jet trajectories, the jet growth, and the mean jet velocity and the mean jet temperature.

The jets showed considerable influence on each other for the jet spacing of four jet diameters. An upward shift of the merged jet trajectory, and a widening of the jet cross-section in both directions for the tandem jets as compared to the single jet, were observed. Good correlation between the mean velocity gradients and Reynolds shear stresses were

found to exist. The detailed flow structure was found to be very similar for the single jet and tandem jet cases for the downstream stations. The distribution of the one-dimensional energy spectra showed spatial and/or configurational dependence; however, no discernible variation of the frequency corresponding to the peak energy, was observed. The flow visualization study showed the existence of circulatory flow in the cross-planes. The analytical study gave results which agreed very well with experimental data.